SEDIMENT TRANSPORT DYNAMICS IN DELAWARE ESTUARY

by

JACQUELINE M. MCSWEENEY

A dissertation submitted to the

Graduate School-New Brunswick

Rutgers, The State University of New Jersey

in partial fulfillment of the requirements

for the degree of Doctor of Philosophy

Graduate Program in Oceanography

written under the direction of

Robert J. Chant

and approved by

_____

_____

_____

_____

New Brunswick, New Jersey

January 2017

ABSTRACT OF THE DISSERTATION

SEDIMENT TRANSPORT DYNAMICS IN DELAWARE ESTUARY

By: JACQUELINE M. MCSWEENEY

Dissertation Director: Robert J. Chant

Estuaries are dynamically complex systems that connect riverine sources to the coastal ocean. The circulation within an estuary is fundamentally 3-dimensional, and lateral processes contribute significantly to material transport. Estuaries are known to trap sediment through convergent processes, and the estuarine turbidity maximum (ETM) zone, an area of elevated suspended sediment concentrations, is a particularly important region of sediment trapping, resuspension, and deposition. Though it is understood that sediment transport processes vary spatially and temporally within the ETM, the details of this variability and their impact on transport pathways and trapping efficiency are unknown. This dissertation characterizes the spatiotemporal variability of sediment processes in the Delaware Estuary, focusing on the contribution of lateral processes, pathways of sediment export, and sediment impacts on primary productivity.

Sediment and velocity observations were acquired during 6 months in 2011 from seven moorings deployed across-channel in the known vicinity of the ETM. The data included upward-looking ADCPS calibrated to *in situ* sediment concentrations from which high-resolution sediment flux estimates were derived to evaluate the relative contributions of tidal and non-tidal processes and how they varied laterally. Tidal pumping contributed to roughly 30% of the along-channel sediment transport, facilitating

export on the flank on the Delaware (DE) side but mostly import in the channel. In contrast, tidal pumping contributed very little to across-channel transport. The subtidal (or residual) sediment transport varied both spatially and temporally, driving export at all locations during high river discharge but export on the flank and import in the channel during lower river flows. Residual fluxes dominated the across-channel transport, and an area of divergence on the DE flank was identified that could facilitate sediment delivery to edging marshes. These observations highlight that sediment transport processes are spatially variable and directly impact sediment trapping in an estuary

A coupled hydrodynamic and sediment transport Regional Ocean Modeling System (ROMS) model was used to evaluate the spatial variability of residual sediment fluxes over spring-neap, seasonal, and annual timescales. Since sediment transport observations are sparse and spatially limited, the model can help clarify the 3-dimensional structure of the ETM and how lateral variability may differ along-channel. This analysis provided a more comprehensive picture of how sediment may be reworked in the ETM or exported either out of the estuary or to the fringing marshes.

The Delaware Estuary is turbid, and primary production within the ETM can become light limited due to high sediment concentrations. In 2010 and 2011, measurements of suspended sediment, light levels, oxygen and nitrate concentrations, and chlorophyll were collected along the main axis of the estuary in March, June, September, and December. These observations were used along with an idealized ROMS model to evaluate stratification and other processes that control sediment resuspension, which in turn impact light availability and primary productivity. This study emphasized that estuarine sediment dynamics have importance implications beyond material transport.

Acknowledgments

This journey has been incredibly challenging and rewarding, and I attribute my success to the unwavering support of my family, friends, and colleagues.

I would like to thank Bob Chant for sharing his knowledge of estuarine physics with me and always encouraging me to grow as a whole, balanced person. Bob, your kindness over the years made my experience at Rutgers such a positive one. Beyond science, I learned from you how to treat people with kindness and respect, how to stand up for myself and learn when to say "no", and how to throw a fantastic dinner party! I am so grateful to have had you as an advisor.

I would also like to thank John Wilkin, who introduced me to the world of physical oceanography. John, your incredible mentorship is in large part the reason I decided to pursue this PhD at Rutgers. You were the first person who recognized the unique value of my chemistry background, and your encouragement boosted my confidence. Thank you for believing in me and giving me a chance to grow as a scientist.

I would also like to thank Chris Sommerfield and Ben Horton, who have been supportive through every committee meeting. Chris, I have learned so much about geology from you. I appreciate the time you spent carefully reviewing my manuscripts. I am undoubtedly a better writer after going through the revision process with you.

I have been blessed to interact with many amazing people during my time at Rutgers. I would especially like to thank Eli Hunter and Liz Sikes for thought-provoking conversations and guidance. Both you provided support and mentorship, for which I am so grateful. Though the ups and downs, my cohort – Alex Lopez, Nicole Waite, Nicole Couto, Brittany Crum, Kevin Crum, Christien Laber, Filipa Carvalho, and Katie Harazin

– has stuck together through it all. It has been a blessing to share this experience with you guys. I would like to also specifically thank Maria Aristizábal , Joe Jurisa, Jeana Drake, Sushmita Patwardhan, Aboozar Tabatabai, Mansha Seth-Pasricha, Guangyu Xu, and Fernando Pareja for the gift of friendship and for your support over the years.

Outside of work, I want to thank my wobble friends - Greg Seroka, Ilissa Seroka, Nick Pollack, Caroline Farkas, Ryan Romanowski, Evan Buckland, and Megan Francis. From softball to BBQs to ladder golf, hanging out together was such a great time. Thanks for picking me up through the tough times and keeping me sane!

I'd also like to thank those of you I've met through science along the way - Jeff Oblecz, Maha Alnajjar, Megan Williams, Anna Wargula, and Georgia Kakoulaki. Our friendships have led to great food, adventurous travel, and many late nights chatting! I am so glad our paths crossed! Thanks for always putting a smile on my face :)

To Ayano and my adopted Fox family, you have stood by my side through thick and thin, always lending an ear and offering words of support. Whether I was calling to rant or share excitement, I've always been happy to share the news with you. Thank you!

Along this journey, I was blessed to meet Aaron and my life will be forever changed. Aaron, you have brightened my life and inspired me to do my best. Thank you so much for your support and patience.

Finally, but certainly not least, I want to thank my family. Mom, Bryan, Sam and Zech, I wouldn't have been able to accomplish this without you. Over the years, you have reminded me of my strength and kept me grounded. It has been tough being across the country, but I have always felt your love and support. Thank you so much for always being there for me and encouraging me to pursue my passions.

Dedication

I dedicate this thesis to my Mom, who has shown me unconditional love and support. Mom, you were the first person to encourage me to explore my scientific curiosity and pursue my dreams. From your example, I learned perseverance and the true meaning of hard work. I will always be grateful for the sacrifices you have made for me and for your efforts in ensuring that I had educational opportunities. I would never have made it this far without you. I love you!

Table of Contents

List of Tables

Chapter 2

List of Figures

Chapter 1

Chapter 2

Chapter 3

Chapter 4

Chapter 1: Introduction

1.1 The Importance of Sediment in Estuaries

Estuaries are among the most productive ecosystems in the world. Though they occupy less than 1% of the earth's surface area, roughly 61% of the human population make their homes on estuarine shores (Bianchi, 2007). Coastal communities rely on estuarine systems for water supply, food resources, shipping, and recreation. In the US alone, roughly $10.8 billion are spent annually on coastal management, and in 2014 coastal counties provided 57 million jobs and contributed $7.6 trillion to the Gross Domestic Product (Kildow et al., 2016). Anthropogenic activity has heavily influenced estuaries on a global scale, introducing issues such as contamination, habitat loss, overfishing, and eutrophication. Estuaries are also impacted by physical changes triggered by climate change, such as sea level rise and an increased frequency of storm events. Thus, over the last few decades researchers have focused on improving our understanding of the natural state of estuarine systems in order to better delineate the extent of human impacts and inform management and restoration efforts.

Sediment transport processes contribute fundamentally to the health and function of an estuary. The sediment dynamics directly impact water quality, biogeochemical cycling, marsh stability, and channel morphodynamics. In the Delaware Estuary, water quality is of utmost importance because the Philadelphia Water Department draws nearly 125 million gallons water for consumption just north of the city (PWD, 2016). High sediment concentrations can be taxing on the filtration systems, causing a large economic cost (Johnson, 1913; PWD, 2016). Sediment transport also plays a crucial role in the stability of the marshes that fringe the bay and lower estuary. The marshes provide important ecosystem services, such as providing habitat for terrestrial and marine species,

serving as a buffer from storm surge and sea level rise, and facilitating sequestration of carbon. Without a steady supply of sediment, marshes are more vulnerable to erosion. Marshes in Delaware have been eroding horizontally at a rate of about 5 m/year in certain regions (Pijanowski, 2016), and the specific role of sediment supply in this loss is an open scientific question. As in most urbanized systems, the navigational channels in Delaware have been deepened to accommodate shipping vessels and require maintenance dredging to prevent the channels from filling in with sediment. Over time, the morphodynamic adjustment of the cross-channel bathymetry to dredging can have feedbacks on circulation, salt intrusion, and sediment transport processes themselves. The societal and economic impacts of sediment transport are numerous, and consequently there is motivation is understand the mechanisms that drive sediment transport and trapping as well as their broader impact.

1.2 The Physics of Estuarine Circulation

Since sediment dynamics are inherently tied to the hydrodynamics of a system, it is important to frame this study in the context of estuarine circulation theory. An estuary's physical response to external forcings – such as wind, waves, or river flow – is evaluated through the momentum balance equations. Pritchard (1956) was the first to elucidate a tidally averaged, along-channel momentum balance to describe the two-layer gravitational flow of an estuary. His conceptual model is the cornerstone of classic estuarine theory and spurred decades of investigation into other solutions of the hydrodynamic equations (Hansen and Rattray, 1965; Chatwin, 1976; Geyer et al., 2000; MacCready, 2004, 2007; Scully and Friedrichs, 2007b; MacCready and Geyer, 2010). In

his solution, the seaward barotropic (*i*) and landward baroclinc (*ii*) pressure gradients are balanced with the vertical stress divergence (*iii*) to yield:

$$\underbrace{g\frac{\partial \eta_o}{\partial x}}_{(i)} + \underbrace{g\beta\frac{\partial \overline{s}}{\partial x}z}_{(ii)} = \underbrace{\frac{\partial}{\partial z}\left(K_o\frac{\partial u_o}{\partial z}\right)}_{(iii)} \tag{0.1}$$

where x is the along-channel direction, z is the vertical direction, g is gravitational acceleration, η_o is the sea surface elevation anomaly, β is the haline contraction coefficient, K_o is the eddy viscosity, u_o is the along-channel velocity, and the subscript o indicates tidally averaged terms. In other words, the estuarine exchange flow is characterized by a surface seaward flow of freshwater from the estuary and bottom landward flow of salt water from the coastal ocean.

Hansen and Rattray (1965) developed an analytical solution to Equation 1.1 for the middle of an estuary (excluding the mouth and head) by integrating twice with respect to z, applying boundary conditions – no slip at the bottom, shear at the surface equal to wind stress $\left(\tau_w = \frac{\partial w}{\partial z}\Big|_{z=0}\right)$ – and assuming a rectangular channel of depth H and width B:

$$u = \overline{u}\left(\frac{3}{2} - \frac{3}{2}\varsigma^2\right) + u_e\left(1 - 9\varsigma^2 - 8\varsigma^3\right) \tag{0.2}$$

$$\varsigma = \frac{z}{H} \tag{0.3}$$

$$u_e = \frac{g\beta\frac{\partial s}{\partial x}H^3}{48K_o} \tag{0.4}$$

where $\overline{u}$ is the depth averaged flow (or the river flow divided by the cross sectional area), u_e is the exchange flow and ς is a non-dimensional length scale relating z and H. This solution was consistent with another solution for u developed by Chatwin (1976),

but the salt balance accompanying Equation 1.2 (Hansen and Rattray, 1965) was challenged by Chatwin's finding that a steady salt balance could be achieved without a diffusive salt flux, indicating that the dynamics remain unresolved.

The temporal scale of the momentum balance analyses has been a subject of interest in the last decades. On subtidal timescales (greater than ~1 day), the exchange flow (Equation 1.2) always reinforces a stable water column, through the strength of stratification depends on spring-neap conditions (Chant et al., 2007). Shifting away from the Pritchard (1952) approach of looking at the mean dynamics, there has been an emphasis on tidal and turbulent timescales (Uncles, 2002; Scully and Friedrichs, 2007b). In a groundbreaking study, Simpson et al. (1990) introduced the concept of strain induced periodic stratification (SIPS), which describes a tidal asymmetry in stratification induced by a vertical straining of the along-channel salinity gradient by tidal flows. Through the SIPS mechanism, stratification becomes enhanced on ebb and turbulent mixing is generated on flood.

Asymmetries in tidal velocities and stratification have been shown to contribute significantly to circulation and the formation of the estuarine turbidity maximum (Jay and Musiak, 1996; Burchard and Baumert, 1998; Scully and Friedrichs, 2007b), which has significant implications for the local environment, productivity, and sediment resuspension (Uncles, 2002). Novel methods of measuring turbulent quantities (Gerbi et al., 2008; Kirincich et al., 2010) and sediment fall velocities (Fugate and Friedrichs, 2002) have provided a means of quantifying vertical processes on shorter timescales and highlighting their importance on tidally mean quantities. These techniques have opened

the door to answering lingering questions about how mixing and dissipation processes impact estuarine circulation (Geyer et al., 2008).

Pritchard's (1956) classic model continues to be used as a starting framework for contemporary analyses, as it has been found to work well for coastal plain estuaries (Geyer et al., 2000; MacCready, 2007; Ralston et al., 2008). Recent work has advanced the momentum balance solutions to incorporate depth-dependent eddy viscosity and dispersion and to account for longitudinal variations in channel depth and width (MacCready, 2004, 2007). These developments are particularly relevant for studying estuaries in a more realistic sense, though they still lack the ability to address the issue of different cross-sectional shapes (MacCready, 2007). It has long been acknowledged that lateral variation of bathymetry is a natural feature of estuaries that plays an important role in estuarine circulation (Fischer, 1972; Smith, 1980; Huzzey and Brubaker, 1988; Uncles, 2002). Thus, there has also been a shift in recent work to explore the importance of lateral variability and identify its effect on transport (Valle-Levinson et al., 2003; Lerczak and Geyer, 2004; Scully and Friedrichs, 2007b). Indeed, the cross-channel morphology of estuarine channels reflects geomorphic feedbacks whereby lateral circulation and waves shape the channel while the channel modifies the wave field and the lateral circulation.

1.3 Physical Mechanisms Driving Estuarine Sediment Transport

The estuarine turbidity maximum (ETM) zone is a region of elevated suspended sediment concentrations (SSC) that typically resides just seaward of the salt intrusion front wherein sediment is hydrodynamically trapped and stored. Early conceptual models

of the ETM describe intense sediment deposition near the salinity intrusion front that is driven by near-bottom flow convergence due to along-channel (axial; longitudinal) baroclinic pressure gradients (Postma, 1967; Schubel, 1968; Meade, 1969; Festa and Hansen, 1978). In recent decades, researchers have expanding on classic theory, identifying other physical mechanisms that impact sediment transport dynamics and sediment trapping in the ETM.

Stratification plays an extremely important role in reinforcing sediment trapping by reducing turbulent diffusivity (Geyer, 1993b). The along-channel salinity gradient is strained by vertically-sheared currents on a tidal timescale, resulting in increased vertical mixing during flood tides and enhanced stratification during ebb tides (Simpson et al., 1990). This tidal straining mechanism generates stratification asymmetries that enable flood-driven sediment transport within the ETM (Jay and Musiak, 1994; Geyer et al., 2001). When the water column is stratified by the ebb tide, vertical mixing is reduced and sediment resuspension is limited to the lower layer. During flood tide, water column instabilities form as saltier water is advected over fresher water and the increased bed stress resuspends sediment, which is then advected up-estuary by the tidal current. Notably, tidal pumping of sediment can drive an up-estuary sediment flux even in the absence of an up-estuary residual current (Postma, 1967; Allen et al., 1980; Scully and Friedrichs, 2003).

Asymmetries in the velocity shear (Jay and Musiak, 1994; Burchard and Baumert, 1998), turbulent mixing (Scully and Friedrichs, 2007b), and bed-stress (Scully and Friedrichs, 2007a) can similarly affect sediment transport patterns. Whereas asymmetries in mixing are controlled primarily by stratification, asymmetries in bed stress are

modulated by changes in the net pressure gradient forcing (Scully and Friedrichs, 2007b). Thus, the tidal variability of stratification and eddy viscosity may actually oppose each other, weakening the total impact of tidal asymmetries on sediment transport. This observation emphasizes that the mechanisms driving material transport can clarify why observed sediment transport patterns may vary on different timescales and among different estuaries.

1.3.1 The Importance of Lateral Processes

While estuarine sediment processes have traditionally been studied in a 2-dimensional framework, recent observational and modeling efforts have highlighted the importance of cross-estuary (lateral) sediment transport and trapping (Huijts et al., 2006; Fugate et al., 2007; Ralston et al., 2012). Lateral processes, such as differential advection and lateral baroclinicity, may modify stratification conditions such that stratification patterns are opposite from those predicted by along-channel tidal straining. For example, Scully and Geyer (2012) concluded that horizontal advection of the lateral density gradient and tidal asymmetries in mixing can generate stratification that is stronger on flood tide than ebb. Similarly, Aristizábal and Chant (2014) observed that tidal reversals of lateral circulation strained the across-channel salinity gradient, driving strong stratification on the flanks during the flood tide but mixing during the ebb. Recent observations in the German Wadden Seas illustrated that lateral flows driving tidal asymmetries in stratification can even have feedbacks that enhance the along-channel estuarine exchange (Becherer et al., 2015). These studies demonstrate that lateral process contribute to important spatial variability in tidal asymmetries, which ultimately can significantly impact patterns of

sediment transport. For instance, tidal asymmetries have been observed to drive sediment export on the shallower flanks in the York, Hudson, and Chesapeake estuaries (Fugate et al., 2007; Scully and Friedrichs, 2007a; Ralston et al., 2012).

An estuary's cross-channel bathymetry also plays an important role in modulating the lateral circulation and consequent lateral salinity gradient, in turn impacting the cross-channel sediment distribution and resuspension (Huijts et al., 2006; Huijts et al., 2011; Ralston et al., 2012; Aristizábal and Chant, 2014; McSweeney et al., 2016a). Bathymetric features can generate salinity fronts, which drive sediment convergence and depositional hotspots (Valle-Levinson et al., 2003; Ralston et al., 2012). Since the morphology of individual estuaries is unique, it is necessary to broadly understand the impact bathymetry has on circulation and transport.

1.3.2 Mechanisms Driving Lateral Circulation

The mechanisms driving lateral circulation (also referred to as secondary flows) may vary between estuaries, but the three main mechanisms that drive lateral flows are Ekman forcing, flow curvature, and differential advection (Figure 1.1). To evaluate the relative importance of these mechanisms in a given system, the lateral momentum balance is evaluated. In Cartesian coordinates, the cross-channel momentum balance is:

$$\underbrace{\frac{\partial v}{\partial t}}_{\text{Acceleration}} + \underbrace{u\frac{\partial v}{\partial x} + v\frac{\partial v}{\partial y}}_{\text{Horizontal Advection}} + \underbrace{w\frac{\partial v}{\partial z}}_{\text{Vertical Advection}} = \underbrace{-g\frac{\partial \eta}{\partial y} - \frac{g}{\rho_o}\frac{\partial \rho}{\partial y}}_{\text{Pressure Gradient}} + \underbrace{fu}_{\text{Coriolis}} + \underbrace{\frac{1}{\rho_o}\frac{\partial \tau_v}{\partial z}}_{\text{Vertical Stress Divergence}} \tag{0.5}$$

where v is the cross-channel velocity, u is the along-channel velocity, t is time, x is the along-channel direction, y is the cross-channel direction, g is the acceleration due to gravity, η is the height of the free surface, ρ is the density, ρ_o is the mean density, f is the

local Coriolis parameter, τ_v is the stress in the cross-channel direction, and z is the vertical direction. Here, the acceleration and advection of the lateral flows are balanced by the lateral pressure gradient, which has barotropic and baroclinic components, the Coriolis term, and the vertical stress divergence. The vertical advective term is typically ignored in estuarine systems because it is usually an order of magnitude less than the leading terms (Aristizábal and Chant, 2014). For example, vertical advection can be scaled as wv/H where H is the depth, w is the vertical velocity and v is the cross channel velocities. Taking typical values of $v \sim 10^{-1}$ m s^{-1}, $w \sim 10^{-3}$ m s^{-1}, and $H \sim 10$ m, the vertical advection scales to 10^{-6}, which is at least an order of magnitude less than the leading terms, which scale to 10^{-4} or 10^{-5}.

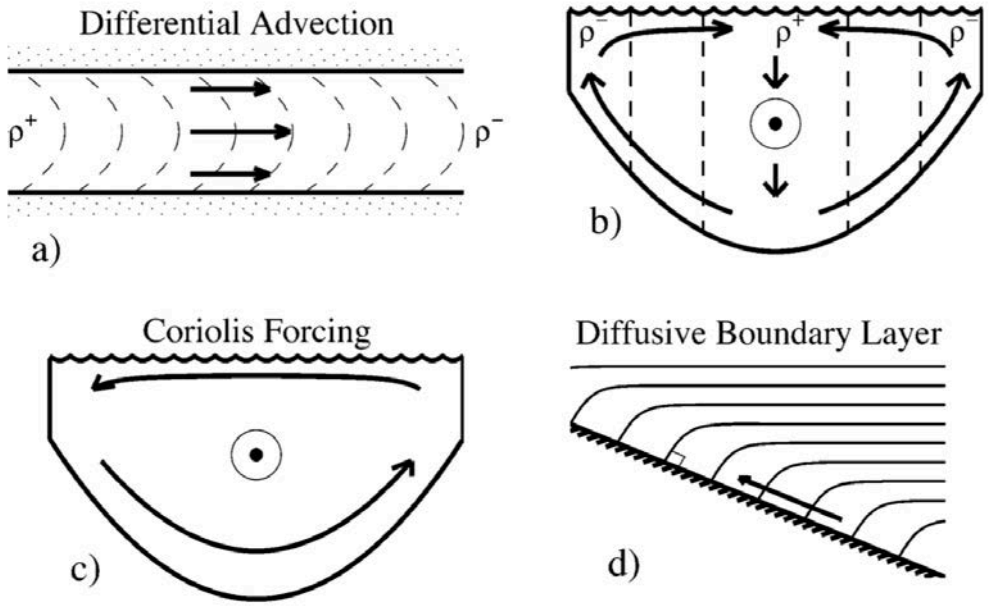

Figure 1.1 Figure from Lerczak and Geyer (2004). (a) Schematic showing distortion of the along-channel density gradient due to differential advection during flood tide. (b) Cross- channel density gradients due to differential advection during flood tide and the lateral circulation pattern that is driven by the lateral pressure gradients. (c) Lateral circulation pattern due to Coriolis forcing during flood tide. (d) Isopycnals tilting to normal at a bottom boundary in order to satisfy a zero-buoyancy-flux boundary condition. The thick arrow indicates the direction of the circulation driven by the along-slope pressure gradient of the diffusive boundary layer.

In cases where Ekman forcing is a dominant term, the main balance in Equation 1.1 is between Coriolis and friction. Idealized models indicate that in a straight channel with symmetric cross channel bathymetry and vertical stratification, an Ekman balance will drive a lateral flow that consists of a single recirculating cell (Lerczak and Geyer, 2004). In the Delaware Estuary, the lateral circulation due to Coriolis and baroclinicity forcing has been observed to rotate clockwise (looking up-estuary) on flood, flowing towards DE at the bottom and towards NJ at the surface, and counter-clockwise during the ebb (Figure 1.2, Aristizábal and Chant, 2014). This single-cell circulation by Ekman, combined with enhanced bottom stresses on the flood tide due to the augmentation of near-bottom tidal currents by the gravitational circulation, would produce a tidally-averaged transport of sediment to the left of the channel. This would favor sediment accumulation on the DE flank and possibly and a migration of the thalweg towards NJ over a longer period of time. Hypothetically, these transport processes could lead to the development of an asymmetric cross section .

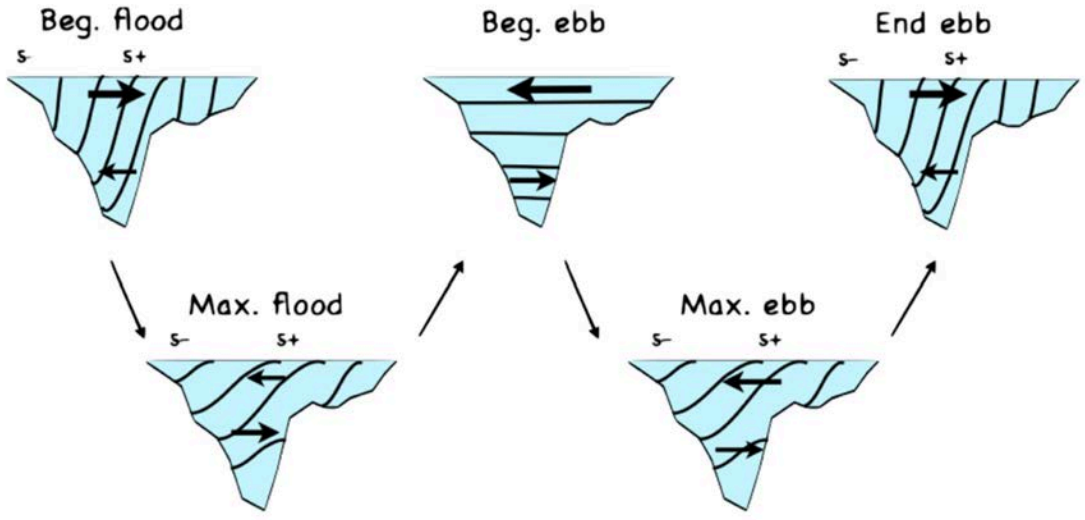

Figure 1.2 Figure from (Aristizábal and Chant, 2014). Cartoon depicting the cross-channel circulation and salinity field for different tidal phases. The oceanward direction is out of the page.

Secondary flows can also be generated by flow curvature around channel bends when the Rossby number is large (Chant, 2002). The Rossby number represents the relative importance of inertia and rotation, and is expressed as $\frac{u}{fR}$, where R is the radius of curvature. When flow curvature is important, centrifugal acceleration becomes a dominant force and is balanced by the cross-channel pressure gradient. The centrifugal acceleration is contained in the horizontal advection terms in Cartesian coordinates, but can be separated from other advective forces by transforming the momentum balance to a curvilinear coordinate system. In curvilinear coordinates, the momentum term for horizontal advection becomes:

$$u_s \frac{\partial u_n}{\partial s} - \frac{u_s^2}{R} \tag{0.6}$$

where s is the streamwise direction, u_s is the streamwise velocity, u_n is the normal velocity, and R is the radius of curvature. Scaling the flow curvature term as u^2/R with typical values from Delaware Estuary ETM (u~ 10^0 m s^{-1}, R ~ 10^4 m), we get a leading term of 10^{-4}. Since the radius of curvature can change significantly along the main axis of an estuary, the role of flow curvature in driving secondary flows may vary spatially within a system. Notably, despite flow curvature playing a significant role in the lateral circulation of many estuaries, studies often neglect the contribution of flow curvature because of spatially limited data or assumed idealized geometry (Lerczak and Geyer, 2004; Aristizábal and Chant, 2014).

The third major contributor to lateral circulation in an estuary is differential advection. Differential advection describes the scenario in which laterally-sheared tidal currents advect the along-channel density gradient, creating a lateral density gradient.

The across-channel pressure gradient, which has an important baroclinic component due to differential advection, is balanced by the vertical stress divergence, resulting in a 2-cell circulation (Nunes and Simpson, 1985). During flood tide, the thalweg is saltier than the flanks and the baroclinic pressure gradient drives surface convergence in the channel. These patterns, along with the direction of the lateral flows, reverse during the ebb tide. Although scaling arguments would indicate that the lateral flows driven by flood and ebb tides are of comparable magnitude, nonlinear feedbacks and stratification asymmetries cause the lateral flows due to differential advection to be enhanced on flood and suppressed on ebb (Lerczak and Geyer, 2004). Thus, secondary circulation pattern associated with differential advection is a 2-cell circulation that converges at the surface and diverges at depth.

1.3.3 Controls on Sediment Resuspension

The phase difference between the lateral flows and sediment resuspension is a crucial factor for advective and tidal-pumping transport (Lerczak and Geyer, 2004; Fugate et al., 2007; Sommerfield and Wong, 2011). Tidal period asymmetries in velocity shear, net rotation effect, eddy diffusivity, and stratification all have complex impacts on the direction and magnitude of the sediment fluxes (Scully and Friedrichs, 2003; Fugate et al., 2007; Aristizábal and Chant, 2014). Furthermore, these asymmetries often have feedbacks that create variability in sediment resuspension that is independent of the lateral circulation patterns. Observations indicate that these asymmetries are often localized and transient, but the mechanistic processes connecting the lateral and sediment dynamics are robust.

Sediment transport is tied closely to estuarine circulation through processes such as erosion, resuspension, advection, mixing, sinking and deposition. These dynamics are driven by both tidal and non-tidal currents and are of particular interest in the ETM, where there are persistently elevated levels of entrapment and resuspension of SSC (Postma, 1967; Sommerfield and Wong, 2011). To first order, the balance of erosion and deposition controls the amount of sediment suspended in the water column, which is then subject to advection and transportation. Friedrichs et al. (1998) calculated a first order equation of this balance for a channel of varying width, which can be described as:

$$\underbrace{\frac{\partial C}{\partial t}+\frac{1}{w}\frac{\partial}{\partial x}(uC)-\frac{1}{w}\frac{\partial}{\partial x}\left(wK\frac{\partial C}{\partial x}\right)}_{SSC}=\underbrace{\frac{\alpha}{\tau_e}u^2}_{erosion}-\underbrace{\frac{C}{\tau_d}}_{deposition} \tag{0.7}$$

where w is the width of the channel, C is the depth-integrated sediment concentration, K is the horizontal diffusion coefficient, α is an erosion parameter, and τ_c is the adjustment time scale for the concentration field (which is assumed to be constant for a given sediment type). One caveat of this approach is that it uses the depth-averaged sediment concentration to get at deposition rates, when in reality the near-bed concentration is more closely tied with this process. However, Friedrichs et al. (1998) justify the use of the depth-averaged concentration by arguing that the bulk of the sediment mass is contained in the lower layer, such that the depth-averaged and near-bottom values are roughly proportional. Since the erosion and deposition terms are often written in terms of the required critical erosion and deposition stresses, τ_e and τ_d respectively (Sanford and Maa, 2001), factors such as near bottom velocity, bottom roughness, and turbulent mixing are significant in this balance.

The sediment size distribution and density are other important factors related to transport because they determine a particle's sinking velocity and critical erosion velocity (Postma, 1967; Sanford and Maa, 2001). When a particle is in suspension, there is a competition between sinking and turbulent mixing which, when in steady state, can be described as:

$$\underbrace{Cw_s}_{sinking} = \underbrace{-K\frac{\partial C}{\partial z}}_{mixing} \tag{0.8}$$

where C is the sediment concentration of a certain particle size, w_s is the particle settling velocity and K is the eddy diffusivity (Geyer, 1993b). For an unstratified system, the eddy diffusivity can be further expressed as:

$$K = \beta\kappa u_*\left(\frac{1-z}{h_o}\right) \tag{0.9}$$

$$u_* = \left(\frac{\tau_b}{\rho}\right)^{\frac{1}{2}} \tag{0.10}$$

where β is a proportionality constant between eddy viscosity and diffusivity, κ is von Karman's constant, u_* is the friction velocity, τ_b is the bottom stress, z is the height above the bed, and h_o is the water depth (Dyer, 1986). Integration of Equation 1.8 yields a Rouse profile, which describes the vertical sediment profile to have an exponential dependency on the Rouse number, $R_o = \frac{w_s}{\beta\kappa u_*}$ (Geyer, 1993b). Since the Rouse number is a balance of the sinking velocity and turbulence, it is a parameter that can be used as a criterion for suspension of particles of a specific diameter and settling velocity (Geyer, 1993b). However, this is complex within estuaries because cohesive sediments and

flocculation often cause particle sizes – and therefore sinking velocities – to vary over short timescales. These fluctuations are due to the balance between turbulence and cohesiveness and have continued to make estimations of sinking velocity a challenge (Hill et al., 2000; Fugate and Friedrichs, 2003).

1.3.4 Timescales of Variability

Estuarine circulation is controlled by a combination of river discharge, tides, and wind, and thus sediment transport mechanisms vary on tidal and subtidal timescales, including spring-neap, seasonal, and longer timescales. At tidal timescales, sediment transport can vary spatially between systems and within a system depending on the dominant mechanisms. For example, tidal-pumping by flood tides tend to drive an up-estuary sediment flux in the York River (Virginia, USA) channel and shoals (Scully and Friedrichs, 2007a). In the Delaware Estuary, tidal pumping drives an up-estuary sediment flux in the channel and a weaker down-estuary sediment flux on the western shoal (Sommerfield and Wong, 2011; McSweeney et al., 2016a). Spring-neap variability of sediment transport similarly differs spatially. In the Hudson Estuary and York River, spring tides have been observed to generate strong landward sediment fluxes (Geyer et al., 2001; Scully and Friedrichs, 2007a), whereas in the Delaware spring tides are dominant in the channel and neap tides are dominant on the flank but the direction of the fluxes is controlled by river discharge conditions (McSweeney et al., 2016a). On longer timescales, river discharge generally modulates sediment fluxes and transport patterns. In the Pearl River Estuary (China), an estuary with extremely complex network of tributaries, sediment characteristics and transport processes in the ETM vary seasonally

due to both stratification patterns and the introduction of new sediment during high flows (Wai et al., 2004; Xia et al., 2004). Seasonal freshets and storm events deliver considerable amounts of new sediment to the turbidity maximum, and sediment can either by reworked in the ETM or exported seaward (Geyer et al., 2001; Cook et al., 2007; Ralston and Geyer, 2009; Cheng et al., 2013).

1.4 Impacts of Sediment on Biological and Chemical Processes

Sediment transport with an ETM has important impacts on chemical and biological processes in the estuary. For example, the fate and composition of estuarine particulate organic carbon (POC) is inherently linked to sediment transport processes. Hermes and Sikes (2016) observed that the ETM region in Delaware Estuary is a geochemical filter for plant-derived POC and that sediment reworking can ultimately decrease the amount of carbon exported. Furthermore, deposition rates and sediment fluxes toward the estuarine coastlines impact the relative magnitude of different carbon pools, ultimately influencing carbon sequestration.

In turbid estuaries with high nutrient loadings, sediment dynamics also have an important impact on light-availability and productivity. Light-limited production has been observed in many urbanized estuaries, including the Hudson Estuary (Stross and Sokol, 1989), San Francisco Bay (Cloern, 1991; May et al., 2003), the Chesapeake Estuary (Malone et al., 1988), the Guadiana Estuary (SW Iberia) (Domingues et al., 2005), the Colne Estuary (east UK) (Kocum et al., 2002), and the Delaware Estuary (Pennock, 1985; Fisher et al., 1988). Because sediment in surface waters attenuates light, systems with turbulent mixing and frequent sediment resuspension can experience

persistent low-light conditions (Biggs et al., 1983). The distribution of sediment, as well as other light-absorbers, is spatiotemporally variable such that light attenuation is a function stratification, mixing, and circulation. For sediment specifically, light absorption patterns depends on the frequency and duration of resuspension, particle size and density, and sediment concentration.

1.5 The Delaware Estuary

1.5.1 Regional Description

The Delaware Estuary is a coastal plain estuary in the Mid Atlantic Bight that extends approximately 215 km from the oceanic mouth through tidal fresh reach (Figure 1.3). The estuary is funnel shaped and has an asymmetric cross-channel bathymetry that has developed through morphodynamic adjustment to decades of dredging and channel deepening. The Wilmington-Philadelphia port complex has significant economic value for the northeast, prompting the decision to accommodate growing shipping vessels through the progressive deepening of the shipping channel from its natural depth of 5–6 m the late 1800s to a uniform depth of 14 m in 2015.

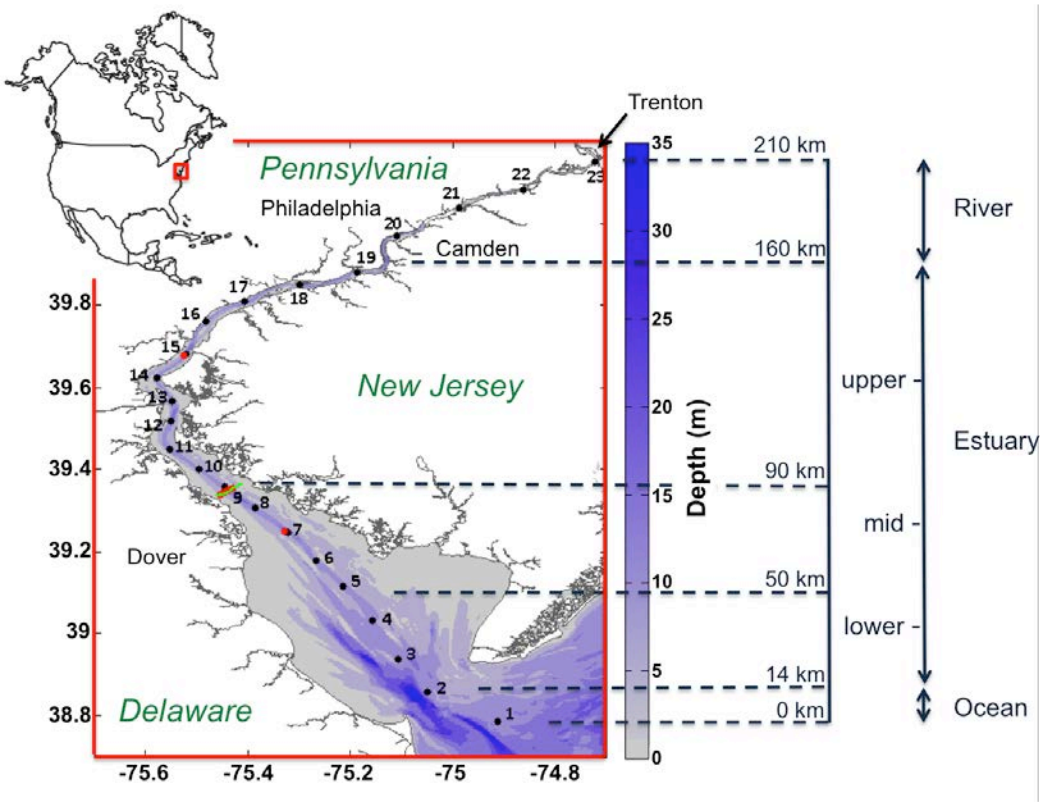

Figure 1.3 Map of the Delaware Estuary

Circulation in the estuary is largely controlled by tides, wind, and river discharge. Semi-diurnal tides generate tidal velocities on the order of 1.5 m s^{-1}, and the tidal range is 1.5 m at the ocean mouth and increases towards the head of the tide near Trenton, NJ (Cook et al., 2007; Wong and Sommerfield, 2009; Sommerfield and Wong, 2011). Remote and local winds modulate the mean sea-level and subtidal currents in most of the estuary, with remote winds primarily controlling sea-level setup and local winds driving currents in the lower estuary (Wong and Moses‐Hall, 1998). The prevailing winds are oriented southeast along the main axis of the estuary, and the region is vulnerable to strong winds from tropical storms and extratropical transitions. In 2011, Hurricane Irene and Tropical Storm Lee delivered heavy rains and anomalously strong winds to the area, breaking historic storm surge and discharge records (Duval, 2013).

The physical dynamics and circulation of the Delaware estuary became of increasing interest in the 1980's, and the system has been a focus of active research since then. In an early study of subtidal circulation, Pape and Garvine (1982) noted that the residual circulation in Delaware was unknown due to the lack of attention the system had received, particularly compared to the nearby Chesapeake. The classification of the estuary is a debatable topic in the literature, probably because of limited sampling and spatial stratification differences. Many previous studies have classified the Delaware as well-mixed (Beardsley and Boicourt, 1981; Garvine et al., 1992; Janzen and Wong, 2002), some arguing that this is evidenced by the tidal volume flux being more than two orders of magnitude greater than the fresh water volume flux (Wong and Sommerfield, 2009). However, others have noted variable stratification and considered it as partially mixed (Pape and Garvine, 1982; Aristizábal and Chant, 2014). Recent work by Aristizábal and Chant (2013) illustrated that the NJ flank is generally well mixed compared to the DE flank and main channel, which can have vertical stratification as strong as 10 psu at times. There is a persistent lateral salinity gradient due to differential advection and a laterally sheared exchange flow which causes the freshest water to hug the Delaware flank (Wong and Moses‐Hall, 1998; Aristizábal and Chant, 2013). This lateral salinity gradient plays an important role in modulating spatial patterns of stratification (Aristizábal and Chant, 2014).

The Delaware River is the main tributary to the estuary and has a mean annual discharge of 340 $m^3 s^{-1}$ (1950-2015). The remaining freshwater inflow comes from the Schuylkill and Christina rivers, which contribute 80 and 20 $m^3 s^{-1}$ respectively, and numerous coastal plain streams in the lower section of the estuary. In a typical year, river

discharge (Q_R) is greatest in March and minimal in September, though storm events can input significantly large amounts of freshwater to the system. Since suspended-sediment delivery is proportional to the freshwater discharge, the highest sediment loadings typically accompany the spring freshet and storm events. The sediment load in tons day^{-1}, Q_s, is estimated to $Q_s \sim a \cdot Q_R{}^b$, where a ranges from 0.01 to 500 (tons day^{-1} m^{-3} s) and b ranges between 1.2 and 3 for estuarine systems (Nash, 1994). For the Delaware River at Trenton, a and b have been estimated from observations to be 0.01 (tons day^{-1} m^{-3} s) and 1.8 (Nash, 1994). The total mean supply of riverine sediment by all tributaries has been estimated to be about 1-2 x 10^9 kg yr^{-1} (Mansue and Commings, 1974), though most of the sediment is supplied from Delaware and Schuylkill rivers. Using the rating relationship above, we estimate that the sediment delivery at Trenton was 2.5x10^8 kg in 2010 and 7.3x10^8 kg in 2011. Because 2011 was a wet year and included several storms that exceeded the historic discharge record, the sediment load in 2011 was nearly triple that of 2010.

Mapping efforts over the last few decades have revealed that the sediment distribution in the estuary is quite patchy. The upper estuary is mostly muddy, whereas the lower estuary and bay is sandy (Weil, 1977; Biggs and Beasley, 1988; Sommerfield and Madsen, 2004). The middle of the estuary is composed of a sand mud mixture that is influenced by axial sediment convergence. Mudfloc sizes usually increase with proximity to the salt intrusion front due to the increased flocculation rates in the ETM (Gibbs et al., 1983). In contrast, flocculation processes are less important in the tidal river and lower bay, so the is a tendency for smaller particle aggregates. The estuarine

circulation, which is inherently very 3-dimensional, drives spatially variable transport that influences sediment fate.

Suspended sediment concentrations are highest in the ETM zone, which is usually just seaward of the salt intrusion front and extends 70-120 km up-estuary from the mouth. The ETM has an along-channel structure that is characterized by a landward leading edge that has sediment mixed throughout the water column and to the surface and an interior (or tail) where sediment is trapped below stratification and cannot be resuspended to the surface (McSweeney et al., 2016a).

Within the ETM, sediment is asymmetrically distributed across-estuary such that the DE flank consistently has higher concentrations and more deposition (McSweeney et al., 2016a). Observations of sediment transport within the ETM indicate that tidal and subtidal processes that drive export on the DE flank and import within the channel, resulting in a lateral straining of the ETM structure (Sommerfield and Wong, 2011; McSweeney et al., 2016a).

1.5.2 Previous Studies of Sediment Transport in Delaware Estuary

The general circulation in the Delaware has been relatively well studied (Pape and Garvine, 1982; Wong and Garvine, 1984; Garvine et al., 1992; Wong and Moses‐Hall, 1998; Janzen and Wong, 2002; Aristizábal and Chant, 2013), but there remain lingering questions about lateral processes and sediment dynamics (Cook et al., 2007; Sommerfield and Wong, 2011). In a study of the sediment transport response to river discharge, Cook et al. (2007) posited that excursions of ETM sediment could be explained by riverine fluctuations, wind forcings and tidal pumping. These interconnections are not surprising

due to the strong correlation between the turbidity maxima and the salt head, but they emphasize the complexity of teasing apart the mechanisms diving transport. Since lateral circulation significantly contributes to the axial distribution of salt (Wong and Moses‐Hall, 1998; Aristizábal and Chant, 2013), it is anticipated that lateral processes are key to sediment transport as well. Supporting this notion, Sommerfield and Wong (2011) provide evidence of different transport patterns between the flank and channel of the upper estuary and suggest that the morphology of the estuary has a feedback on axial sediment due to the residual current having a dependency on the depth cubed. Thus, they argue the importance of both tidal pumping on the flanks and lateral variations in gravitational transport as mechanisms for sediment sequestration.

Our understanding of sediment transport patterns in the Delaware Estuary has improved significantly in the last decade. Observations of tidal sediment fluxes in the channel of the upper-estuary revealed that tidal pumping is more important in the ETM than further down-estuary, where bed-sediment becomes depleted early in the tidal cycle (Cook et al., 2007). Sediment delivery from the tidal freshwater river to the upper estuary is primarily driven by a river-induced mean current (Cook et al., 2007; Wong and Sommerfield, 2009). Within the ETM, both tidal and advective sediment transport mechanisms contribute significantly to total transport but these mechanisms vary spatially, especially between the estuarine channel and shallower subtidal flanks (Sommerfield and Wong, 2011). Both tidal and residual fluxes are capable of driving up- or down-estuary, and the patterns are dependent on location, spring-neap, and river discharge conditions (Sommerfield and Wong, 2011; McSweeney et al., 2016a).

1.6 Thesis Objectives and Outline

This chapter has provided context for the research results that are presented in this thesis. Several research questions about estuarine sediment transport motivate this work:

1. How does sediment transport vary spatially in Delaware Estuary?
2. What mechanisms explain the observed spatial sediment transport patterns?
3. How do these mechanisms and patterns vary of tidal, spring-neap, and longer timescales?
4. How do spatiotemporal patterns in sediment transport ultimately impact the trapping efficiency of the estuary?
5. How do sediment dynamics influence the light available for production?

The thesis is structured as follows:

In Chapter 2, we will use observations from a mooring transect in the vicinity of the ETM to look at the lateral variability of along-channel and across-channel sediment transport. We decompose the sediment fluxes to evaluate the relative contribution of tidal and residual processes. Since the data span roughly 6 months, we look at spring-neap variability as well as high and low river discharge periods. We conclude with an analysis of the tidal pumping mechanism and the factors that may contribute to spatial variability in tidal pumping.

In Chapter 3, we use a Regional Ocean Modeling System (ROMS) model that couples hydrodynamics and sediment dynamics to further evaluate the spatiotemporal variability of sediment residual transport. Looking at spring-neap, seasonal, and annual timescales, we describe how different timescales contribute to sediment transport patterns. We emphasize the 3-dimensinonal nature of circulation and

transport, demonstrating the impact on the trapping efficiency of the ETM. We also describe the importance of lateral processes and illustrate how the across-channel momentum balance varies along the axis of the estuary.

In Chapter 4, we use both data and an idealized ROMS model to describe how sediment dynamics ultimately influence light availability and modulate spatial patterns of primary productivity. We show how stratification variability, which varies with spring-neap and river discharge conditions, controls sediment resuspension and therefore the light field. This chapter highlights the broader importance of sediment transport processes.

We conclude the thesis with a chapter summarizing our main findings.

Chapter 2: Lateral Variability of Sediment Transport in the Delaware Estuary

2.1 Abstract

Lateral processes contribute significantly to circulation and material transport in estuaries. The mechanisms controlling transport may vary spatially such that shallow and deep regions of an estuary contribute differently to the total transport. An observational study was conducted to explore the importance of lateral variability in sediment transport mechanisms in the Delaware Estuary. Seven moorings were deployed across the channel in the region of the estuarine turbidity maximum (ETM) zone from April to August 2011. Time series of along-channel sediment transport reveal a consistent pattern of sediment export across the entire estuary during periods of high river discharge, followed by a transition to import within the channel and export on the flanks during low river flow. There is a persistent divergence of across-channel sediment fluxes on the Delaware side, where sediment from the flank is transported toward both the channel and wetland coast. Decomposition of the fluxes highlight that across-channel sediment transport is driven by mean lateral circulation, whereas along-channel transport is driven primarily by mean advection, with tidal pumping contributing to about 30% of total transport. The spatial and temporal variability of mean advection and tidal pumping were generally complementary, with both contributing to the observed sediment transport pathways. Tidal pumping, linked to tidal asymmetries in stratification and sediment resuspension, was shown to drive both ebb-driven export and flood-driven import depending on the tidal variability of stratification. The spatiotemporal patterns of sediment transport highlight the three-dimensional structure of the ETM and shed light on the variability of sediment transport mechanisms.

2.2 Introduction

Sediment transport processes are fundamental to the water quality, biogeochemical cycling, and morphodynamics of an estuary. The estuarine turbidity maximum (ETM) zone, a region of elevated suspended sediment concentrations (SSC), is of particular interest due to its ability to trap and store sediment. Early conceptual models of the ETM were based on the simple idea that along-channel (axial; longitudinal) gradients in the baroclinic pressure field generate near-bottom flow convergence near the limit of the salinity intrusion, leading to intense deposition of sediment (Postma, 1967; Schubel, 1968; Meade, 1969; Festa and Hansen, 1978). This traditional view has been challenged by recent observational and modeling studies of cross-estuary (lateral) sediment transport and trapping (Huijts et al., 2006; Fugate et al., 2007; Ralston et al., 2012), which indicate that lateral processes are equally important.

One important mechanism reinforcing sediment trapping within in the ETM is the reduced turbulence due to stratification (Geyer, 1993b). When the along-channel salinity gradient is subjected to vertically sheared tidal currents, the longitudinal density field becomes strained, enhancing stratification on the ebb tide and generating vertical mixing on flood (Simpson et al., 1990). Tidal asymmetries in stratification due to this tidal straining mechanism have been shown to generate significant flood-driven sediment transport within the ETM (Jay and Musiak, 1994; Geyer et al., 2001). During the ebb tide, stratification suppresses vertical mixing and sediment is limited to the lower part of the water column. As the tide transitions to flood, saltier water is advected over fresher water, generating water column instabilities and consequent mixing. The stress on the bed suspends sediment into the water column, which is then subjected to advection by the tidal current and pumped up-estuary. Significantly, tidal pumping of sediment by this

mechanism has been shown to generate an up-estuary sediment flux independent of an up-estuary advective residual current (Scully and Friedrichs, 2003).

Recent observations have revealed that lateral processes may result in stratification patterns contrary to those predicted by along-channel tidal straining. Scully and Geyer (2012) posited that horizontal advection of the lateral density gradient, coupled with tidal asymmetries in mixing, can generate stronger stratification on flood tide compared to ebb tide. Similarly, Aristizábal and Chant (2014) noted that tidal reversals of lateral circulation strained the across-channel salinity gradient such that the flanks experienced strong stratification during the flood tide and were nearly well mixed during ebb. Such observations have raised awareness that cross-channel circulation mechanisms have important implications for tidal asymmetries.

Recent efforts to characterize lateral variations in sediment transport have highlighted the significance of tidal asymmetries in turbulent mixing, bed stress, and stratification. Partially mixed estuaries, including the York, Hudson, and Chesapeake, have been observed to export sediment on the flank due such tidal asymmetries (Fugate et al., 2007; Scully and Friedrichs, 2007a; Ralston et al., 2012), though the mechanisms driving tidal transport differ among systems. It is important to note that Scully and Friedrichs (2007b) distinguish that tidal asymmetries in mixing are controlled in large part by stratification whereas tidal asymmetries in bed stress are generated by the net pressure gradient forcing. Thus, the stratification and eddy viscosity variability on a tidal timescale may oppose each other, weakening the impact of tidal asymmetries on sediment fluxes. These observations emphasize the importance of identifying the mechanisms driving tidal pumping to clarify how asymmetries impact material transport.

This paper explores lateral variability of sediment transport mechanisms in the Delaware Estuary, with particular attention to the influences of stratification on tidal pumping variability. Prior work has shown that the relative importance of tidal and advective transport mechanisms differ between the estuarine channel and shallower subtidal flanks (Sommerfield and Wong, 2011); however, the role of salinity stratification has not been explored. By relating transport by tidal pumping to stratification and resuspension asymmetries, we expand on past work by elucidating the tidal pumping mechanisms specific to channel and flank subenvironments. Furthermore, we examine the lateral variability of across-channel sediment transport and its role in the three-dimensional structure of the ETM. These sediment-transport processes are fundamentally related to bathymetry (Ralston et al., 2012) and thus are of morphodynamic significance on the long term.

2.3 The Delaware Estuary

The Delaware Estuary is a coastal plain estuary nested between Delaware, New Jersey, and Pennsylvania (Figure 2.1a). It extends approximately 215 km from the oceanic mouth of the bay through the reach of the tidal riverine portion. Dominated by semi-diurnal tides, the tidal range is approximately 1.5 m at the mouth and increases toward the head of the tide, with maximum tidal currents on the order of 1m/s (Cook et al., 2007; Wong and Sommerfield, 2009; Sommerfield and Wong, 2011). To accommodate shipping traffic to the Wilmington-Philadelphia port complex, the shipping channel has been progressively deepened since the late 1800s from its natural depth of 5–6 m to a uniform depth of 14 m in 2015.

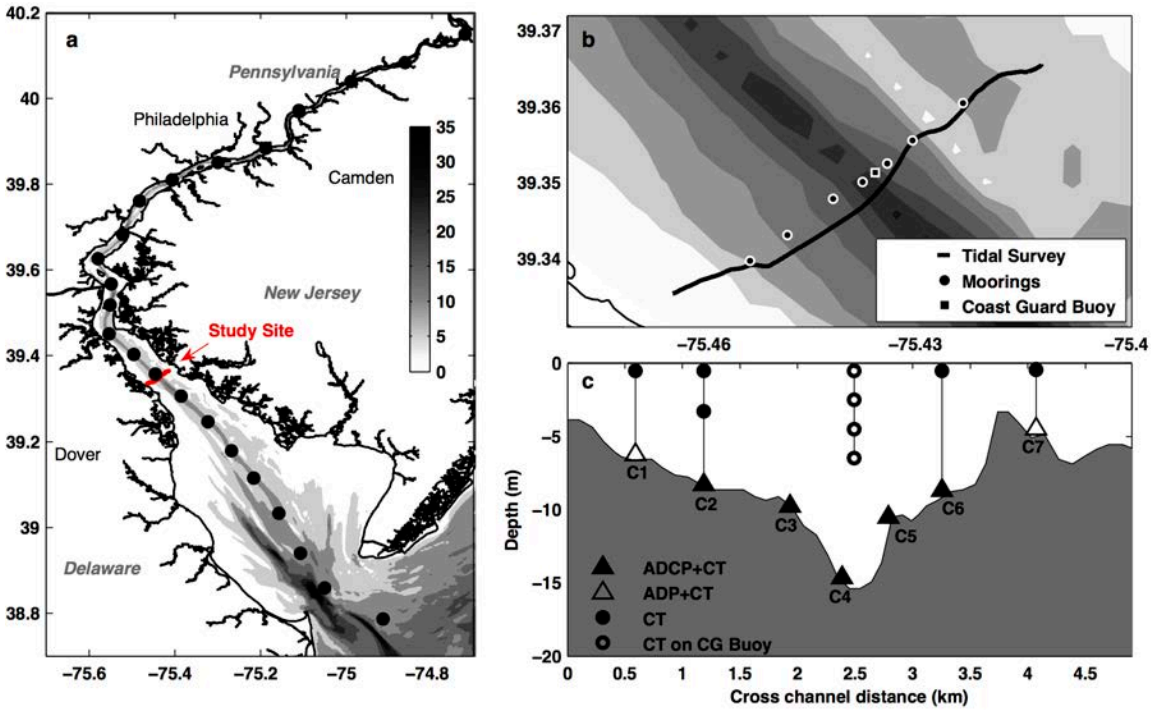

Figure 2.1. Map of the Delaware Estuary (a) Bathymetry (m) is noted by the grayscale. The black dots represent the 23 survey stations from the axial surveys. The red sample site line indicates the location of the moorings and tidal surveys; (b) zoomed in picture of mooring and Coast Guard buoy locations with grayscale bathymetry; and (c) mooring transect set up.

The freshwater discharge to the estuary, Q_R, is dominated by the Delaware River, which supplies more than half of the input with an annual mean discharge of 330 m^3/s. The remaining inflow is contributed by the Schuylkill and Christina river tributaries, with annual mean flows of about 77 and 19 m^3/s, as well as numerous coastal plain streams in the lower section of the estuary (Mansue and Commings, 1974). The U.S. Geological Survey record from 1912 to present indicates that mean freshwater discharge of the Delaware usually peaks around March and is minimal around September (Figure 2.2a). Notably, 2011 was an anomalously wet year, and there were many discharge events that exceeded the historic mean.

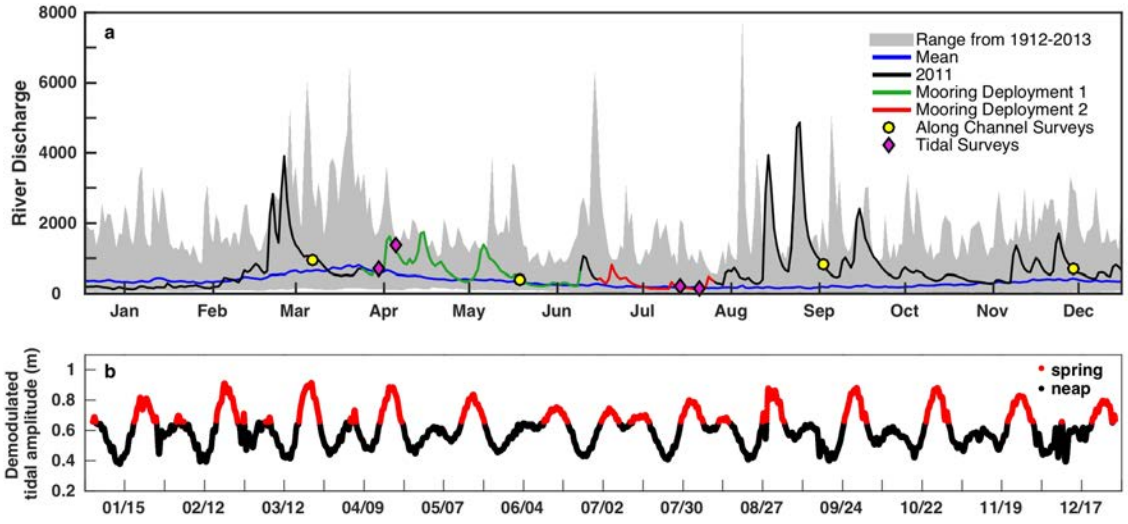

Figure 2.2. Timeseries of river discharge (a) Mean daily discharge (m^3 s^{-1}) of the Delaware River at Trenton, 1912–2013. Gray shaded region shows the range over the whole record. The solid black line is the 2011 discharge record, the green and red lines show the durations of the first and second mooring deployments respectively, the yellow dots represent the along-channel surveys, and the pink diamonds indicate the lateral-transect tidal surveys. (b) The demodulated tidal amplitude (m) for 2011 from a sea level gauge in Lewes, Delaware. The red dots indicate spring tides, identified by when the demodulated tidal amplitude is greater than the mean. The black dots indicate neap tides.

The suspended sediment load (tons/d) of rivers, Q_s, is in general proportional to the fresh water discharge (m^3/s) such that $Q_s \sim aQ_R^{\ b}$, and where *a* ranges from 0.01 to 500 and *b* ranges between 1.2 and 3 (Nash, 1994). For the Delaware River at Trenton, the observed values for *a* and *b* are 0.01 and 1.8 respectively, indicating that the minimum discharge rate required to transport sediment is relatively low (Nash, 1994). The mean total supply of suspended sediment from the river tributaries is estimated to be about 1-2 x 10^9 kg/yr (Mansue and Commings, 1974), most of which is supplied by the Delaware and Schuylkill rivers. Using the rating relationship above, we estimate that the sediment loading at Trenton for 2011 was roughly 7.3 x 10^8 kg. Similar to the seasonal variation of river discharge, the maximum sediment loadings typically accompany the spring freshet events in March and April (Cook et al., 2007; Sommerfield and Wong,

2011). Suspended sediment concentrations are highest in the ETM zone, which extends 70-120 km up-estuary from the mouth and is usually centered near the 0.1-1 isohaline (Figure 2.3). Due to high flocculation and aggregation rates near the head of the salt intrusion, mudfloc sizes also tend to increase with proximity to the ETM. Thus, the tidal river and lower bay are characterized by lower SSC values and smaller mudfloc sizes (Gibbs et al., 1983). There is some evidence to suggest that flocculation rates and particle aggregate sizes are maximal within the ETM region (Gibbs et al., 1983).

Previous research has indicated that the mechanism of sediment delivery from the tidal freshwater river to the upper estuary is primarily driven by a river-induced mean current (Cook et al., 2007; Wong and Sommerfield, 2009). Within the upper and lower segments of the estuary, tidal asymmetries in velocity and SSC generate tidal pumping fluxes that vary in strength and direction, moderating residual sediment fluxes (Sommerfield and Wong, 2011). Although the overall pattern of residual sediment fluxes suggests that the controlling mechanisms vary between the estuarine channel and subtidal flanks (Sommerfield and Wong, 2011), lateral variation of sediment flux could not be determined in past studies due to a limited number of measurement stations. Indeed, the results of Sommerfield and Wong (2011) are based on a single point measurement on the flanks, which is unable to capture the vertical structure of either tidal or residual flows. Nonetheless, studies of lateral variation in the salinity field support the idea that lateral density gradients and secondary circulation have important implications for sediment transport (Wong, 1994; Aristizábal and Chant, 2013).

2.4 Methods

2.4.1 Mooring Instrumentation and Measurements

In 2011, seven moorings were deployed across the channel approximately 90 km up-estuary from the mouth, within the lower limit of the ETM zone. These were equipped with surface and bottom CT sensors to measure salinity and temperature and bottom mounted, upward-looking 1200 kHz RDI ADCPs or Sontek ADPs (Figure 2.1b,c), which measured velocity and acoustic backscatter. A string of CT sensors was deployed off a Coast Guard Buoy near C4 to measure salinity in the channel without obstructing the shipping lane (Figure 2.1b, c). The subtidal flat flanking the channel on the Delaware side of the estuary (DE flank; moorings C1 and C2) has a relatively smooth transition to the deeper channel (moorings C3, C4, and C5) compared to the subtidal flank on the New Jersey side (NJ flank; C6 and C7), which is separated from the channel by a shallow shoal. Since sediment deposition is known to be higher on the DE flank (Sommerfield and Madsen, 2004), the moorings were arranged to detail this region.

The C1-C6 moorings were deployed April to late June 2011, and C1-C7 moorings were deployed early July to August 2011. As shown in Figure 2.2a, the river discharge was higher during the first deployment (mean of 678 m^3/s) compared to that during the second (mean 297 m^3/s). Because of instrument fouling and technical issues, particularly during the first deployment, some moorings did not return data. Specifically, data from C1 and C6 were not available for the entirety of the first deployment and the records from C3 and C4 were cut short. During the second deployment, only C2 was fouled.

The lowermost ADCP bin was about 1-1.5 m above the seafloor, and the upper 1-1.5 m of the water column was contaminated by side-lobe interference with the surface seawater. Since the transport at the bed and surface are integral to a discussion of total

transport, the data profiles were extrapolated to span the entire depth. Current profiles were extrapolated to the bottom assuming a log profile as follows

$$u(z) = \frac{u_*}{\kappa} \ln\left(\frac{z}{z_0}\right) \tag{1.1}$$

where u_* is the bottom friction velocity, κ is the von Karman's constant (0.4), z is the depth, and z_o is the bottom roughness. Sensitivity tests demonstrated that the extrapolations were relatively insensitive to the bottom roughness, and z_o was selected to be 0.067m following Lerczak et al. (2006). Velocities were extrapolated to the surface by fitting a parabolic curve to three observations at the top of the ADCP profile and forcing the vertical shear, $\partial u/\partial z$, to zero at the surface. Suspended sediment concentrations were estimated with acoustic backscatter that was calibrated against *in situ* measurements (described in section 2.4.3). Following the methodology of Chant et al. (2010), sediment profiles were extrapolated linearly to both the bottom and surface. Bubble contamination was an issue at the surface, so the corresponding high backscatter signal in the uppermost part of the water column was removed from the dataset prior to the surface extrapolation.

Once extrapolated, the velocity and sediment profiles were transformed from a vertical coordinate system to a sigma (σ) coordinate system with 80 equally spaced σ-levels. The σ-coordinate system is defined as:

$$\sigma = \frac{z - \eta(t)}{h + \eta(t)} \tag{1.2}$$

where h is the mean water depth and $\eta(t)$ is the time-varying sea-level, which has tidal and subtidal components. This transformation eliminates the tidally-variable position of

fixed ADCP bins (z-levels) in the water column and yields a continuous dataset at every σ level.

Finally, the velocities were separated into along-channel and across-channel components. This was accomplished by finding the major axis of the M2 component of the *u* and *v* velocity components and then rotating the entire dataset according to this axis.

Spring-neap tides during the deployments were identified by demodulating the 2011 sea level record from a tide gauge in Lewes, Delaware (Figure 2.2b). If the demodulated tidal amplitude (m) was greater than the mean, it was identified it as a spring tide. In the context of the year-long record, the study time period was characterized by weak spring tides.

2.4.2 Along-Channel and Across-Channel Surveys

Four along-estuary surveys were conducted in 2011, with one contemporaneous with the mooring deployments. These surveys involved taking vertical profiles at 23 stations along the channel's thalweg with an instrument package equipped with a CTD and an optical backscatter (OBS) sensor (Figure 2.1a). The OBS was calibrated with the *in situ* samples to calculate sediment concentrations, which were then used to contextualize the approximate axial location of the ETM and the along-estuary distribution of sediment during the mooring deployments (Figure 2.3).

Additionally, four cross-channel tidal surveys were conducted shipboard over the course of the two mooring deployments (Figures 2.2a , 2.4). An instrument package that included a CTD to measure salinity and temperature and an OBS was towed abeam of the boat in a yo-yoing motion that covered the full extent of the water column. At the end of

each section, the boat stopped to collect surface and bottom water samples for calibration of optical and acoustic sensors. All transects were run from the NJ side to the DE side. A boat-mounted, downward looking ADCP was used to collect current data and acoustic backscatter, which was then calibrated with *in situ* samples to estimate SSC (Figure 2.4). Each survey yielded roughly 13 40-min lateral transects, providing a synoptic picture of the lateral distribution of suspended sediment concentration.

2.4.3 Calibrations

Suspended sediment concentrations were estimated from the ADCP acoustic backscatter (ABS) through a series of instrument-specific calibrations. Prior to all calibrations, the acoustic backscatter data were corrected to account for range spreading and absorption by water following the methods of Sommerfield and Wong (2011). OBS point measurements were first linearly calibrated with co-collected *in situ* SSC samples from two of the tidal surveys that overlapped with the mooring deployments (Equation 2.3). The regression coefficients (a_1 and b_1) were used to calibrate the cage-mounted OBS sensor to ABS from a boat mounted ADCP (Equation 2.4). The boat mounted ADCPs from each survey were then used to calibrate each moored ADCP by isolating the temporal and spatial data that overlapped and calculating the regression between the two vertical profiles (Equation 2.5). These regressions were then used to estimate a timeseries of vertical sediment profiles (Equation 2.6). Tables 2.1-2.3 summarize the regressions for each mooring, including R^2 values for each calibration, which ranged from 0.576 to 0.915.

$$TSS_{in\,situ}\left(\frac{mg}{L}\right)=\left[OBS_{pt}(volts)\times a_1\right]+b_1 \tag{1.3}$$

$$\log_{10}\left(\left[OBS_{cage}(volts)\times a_1\right]+b_1\right)\left(\frac{mg}{L}\right)=\left[ABS_{boat}(dB)\times a_2\right]+b_2 \quad (1.4)$$

$$\left[ABS_{boat}(dB)\times a_2\right]+b_2=\left[ABS_{moor}(dB)\times a_3\right]+b_3 \quad (1.5)$$

$$SSC_{moor}\left(\frac{mg}{L}\right)=10^{\left[ABS_{moor}(dB)\times a_3\right]+b_3} \quad (1.6)$$

	a_1	b_1	R^2
April 18-19, 2011	63.3207	65.5212	0.63433
July 27-28, 2011	59.2214	-2.2479	0.91540

Table 2.1 Calibration regression of cage mounted OBS to *in situ* SSC samples (Equation 2.3)

	a_2	b_2	R^2
April 18-19, 2011	0.019677	0.46103	0.67476
July 27-28, 2011	0.033972	-1.6593	0.67100

Table 2.2 Calibration regression of boat-mounted ABS to cage mounted OBS (Equation 2.4)

As shown in Table 2.3, there was a change in the calibration coefficients between deployments perhaps due to variations in particle size and (or) flocculation processes over time. In order to address the impact of this change, sensitivity tests were run to determine the difference between uniform versus variable calibration coefficients. We estimated all fluxes using 10 sets of uniform coefficients, spanning from a=0.01, b=1.2 to a=0.035, b= -0.7 with equally spaced intervals. The uniform calibrations introduced expected changes in the magnitude of the estimations, overestimating the first deployment fluxes and underestimating the second compared to those estimated with the coefficients in Table 2.3. However, the relative importance of tidal and subtidal fluxes and their spatiotemporal variability were unaffected by using a uniform calibration.

Thus, we argue that the results presented in this paper are unaffected by the change in ADCP-SSC calibrations.

	a_3	b_3	R^2
April 18-19, 2011			
Mooring C2	0. 011980	1.21326	0. 66838
Mooring C3	0. 012278	1.15328	0. 62268
Mooring C4	0. 012271	1.23082	0. 41814
Mooring C5	0. 012057	1.15422	0. 57659
July 27-28, 2011			
Mooring C1	0.028318	-0.63199	0.74912
Mooring C3	0.025905	-1.0859	0.84536
Mooring C4	0.034250	-1.6517	0.67662
Mooring C5	0.026896	-1.1532	0.71389
Mooring C6	0.014992	-0.17015	0.09422
Mooring C7	0.023853	-0.79097	0.35561

Table 2.3 Calibration regression for coincident data from the moored and boat-mounted ABSs (Equation 2.5)

The CTD package was equipped with both a low range and high range OBS sensor. The low range sensor was selected for the calibrations because *in situ* measurements indicated the sensor's sensitivity to lower values of SSC was more appropriate in the Delaware system. However, this selection may lead to an underestimation of SSC for concentrations greater than 450 mg/L.

2.4.4 Sediment Flux Estimation and Decomposition

Along-channel and across-channel suspended sediment fluxes were calculated at each mooring position using the sediment and velocity profiles. Positive transport values indicate flux into the estuary, whereas negative values represent transport down-estuary. Since the instantaneous velocity and SSC can also be described as the sum of the tidally-varying (U_t, C_t) and tidally averaged parts (U_{mean}, C_{mean}), the two profiles were first decomposed using a 36 h Lanczos low-pass filter.

$$U_{mean}(t,\sigma) = U_{lp}(t,\sigma) \qquad C_{mean}(t,\sigma) = C_{lp}(t,\sigma) \tag{1.7}$$

$$U_t(t,\sigma) = U(t,\sigma) - U_{lp}(t,\sigma) \qquad C_t(t,\sigma) = C(t,\sigma) - C_{lp}(t,\sigma) \tag{1.8}$$

The mean advective transport ($Q_{s\,mean}$) and tidal transport ($Q_{s\,t}$) were then calculated as follows:

$$Q_{s\,mean}(t) = H\int_0^1 U_{mean}C_{mean}\,\partial\sigma \tag{1.9}$$

$$Q_{st}(t) = \left[H\int_0^1 U_t C_t\,\partial\sigma \right]_{lp} \tag{1.10}$$

where H is the water column depth. This decomposition aims to isolate the specific effects of tidal pumping and mean advection on sediment transport (Geyer et al., 2001; Sommerfield and Wong, 2011). The mean term was not further decomposed into estuarine and riverine components as done by Chant et al. (2010) because the laterally sheared exchange flow can only be marginally resolved with 4-6 moorings across the channel. Thus, we would not be able to isolate the mean river flow of less than 1 cm/s from a laterally-sheared exchange flow that exceeds 10 cm/s and drives outflow on the Delaware side of the river. Thus, we kept the mean advective term as is, but argue that

the riverine component can only export sediment, the vertical shear component can only import with elevated SSC at the bottom, and the lateral shear can either import or export depending on the lateral distribution of sediment.

The total instantaneous sediment transport, the sum of the tidal and mean advective terms, was also integrated in time over each mooring record to yield a cumulative sediment transport in metric tons per unit width. These estimations of the integrated transport shed light on the net gain or loss of sediment from the estuary during the deployments, but are not used to develop a sediment budget due to data gaps and uncertainties in ADCP-SSC calibration.

2.5 Results

2.5.1 Suspended Sediment Distribution

The ETM zone was located approximately 100 km up-estuary from the mouth in early June 2011 (Figure 2.3). The high-concentration core of the ETM extended for roughly 20 km, with a 20-km long tail of lower sediment concentrations. Maximum SSC values in the core and tail were approximately 230 and 120 mg/L, respectively. The landward edge of the ETM coincided with the salt intrusion (~1 psu), and the water column was relative well mixed through the core of the ETM. Thus, resuspension within the ETM core extended the full depth of the water column, with vertical profiles of SSC characterized by heightened concentrations near the bed. A subsurface salinity front with a vertical stratification of about 3 psu extended over the ETM tail, limiting resuspension there to the lower 6 m of the water column.

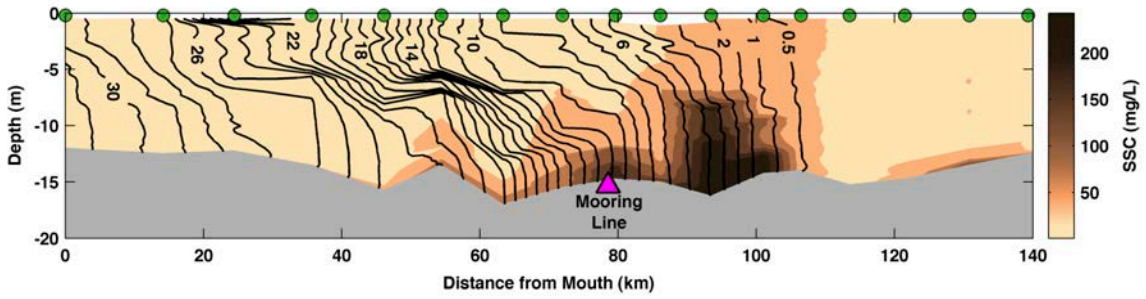

Figure 2.3 Along-channel distribution of suspended sediment concentration (SSC in mg/L) from an along-channel survey 3–4 June 2011. Salinity (psu) is contoured in black. The magenta triangle represents the across-channel mooring line. The green circles at the top show the locations of the vertical casts.

The shipboard tidal surveys revealed a consistent pattern of elevated sediment concentrations on the DE flank, with lower SSC values on the NJ flank (Figure 2.4). Concentrations observed on the DE side were 2-4 times greater than those measured on the NJ flank. This distribution is consistent for all four tidal surveys and the entirety of the C1, C2, C3, and C7 mooring records, indicating that this lateral pattern is consistent. Lateral gradients of the salinity field and vertical stratification are worth noting. The DE side of the estuary is consistently fresher than the NJ side, causing an important baroclinic pressure gradient across the channel (Figure 2.4). Furthermore, the NJ side is relatively well mixed over a tidal cycle whereas the DE side exhibits variable tidal stratification, with stratification weakening over the ebb and becoming enhanced on flood. This tidal asymmetry in stratification is driven by the straining of isopycnals by lateral circulation and along-channel advection (Aristizábal and Chant, 2014) and has significant implications for sediment transport on the DE flank. As shown in Figure 2.4, the height of sediment resuspension appears to be limited by stratification.

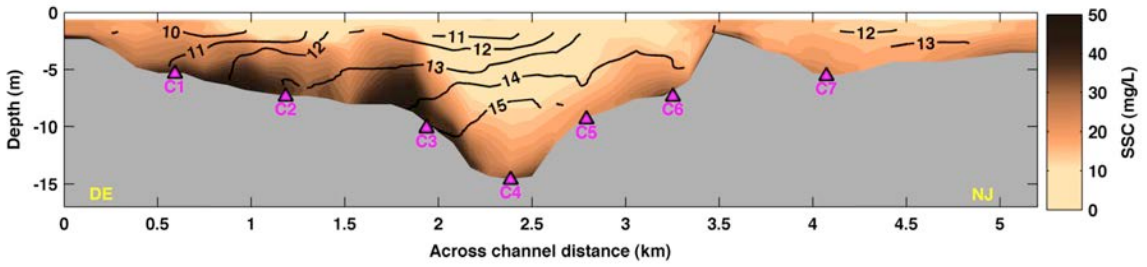

Figure 2.4 Lateral distribution of suspended sediment (mg/L) from a survey on 28 July 2011 during the ebb tide. Salinity contours are in black. Perspective is looking into the estuary.

2.5.2 Using Salinity to Contextualize the Position of the ETM Zone

The axial survey discussed in section 2.4.2 took place during the transition from high to low flow periods (Figure 2.2a). As is evident in Figure 2.3, the moorings would have then captured the seaward tail of the ETM in June. Following that the ETM has been observed to migrate in response to river discharge conditions (Sommerfield and Wong, 2011), it is thus likely that the ETM was down-estuary of the June location during the majority of the first mooring deployment and in a roughly similar location during the second deployment. This would suggest that our first deployment captured more of the ETM core while the second captured more of the ETM tail. This notion can be further analyzed by examining the timeseries of bottom salinity in the channel and comparing it to that observed during the axial survey (Figure 2.5, top). The lower salinities during the first deployment, as low as 1.3 psu on 19 April, support the idea that high river discharges probably pushed the ETM oceanward, such that the ETM core resided in the vicinity of the moorings. The increased salinities measured during the second deployment further suggest that the ETM had migrated back up-estuary in response to weaker river flows, with moorings capturing more of the activity in the ETM tail. This

migration of the ETM is corroborated with snapshots of the ETM from longitudinal surveys in March and June.

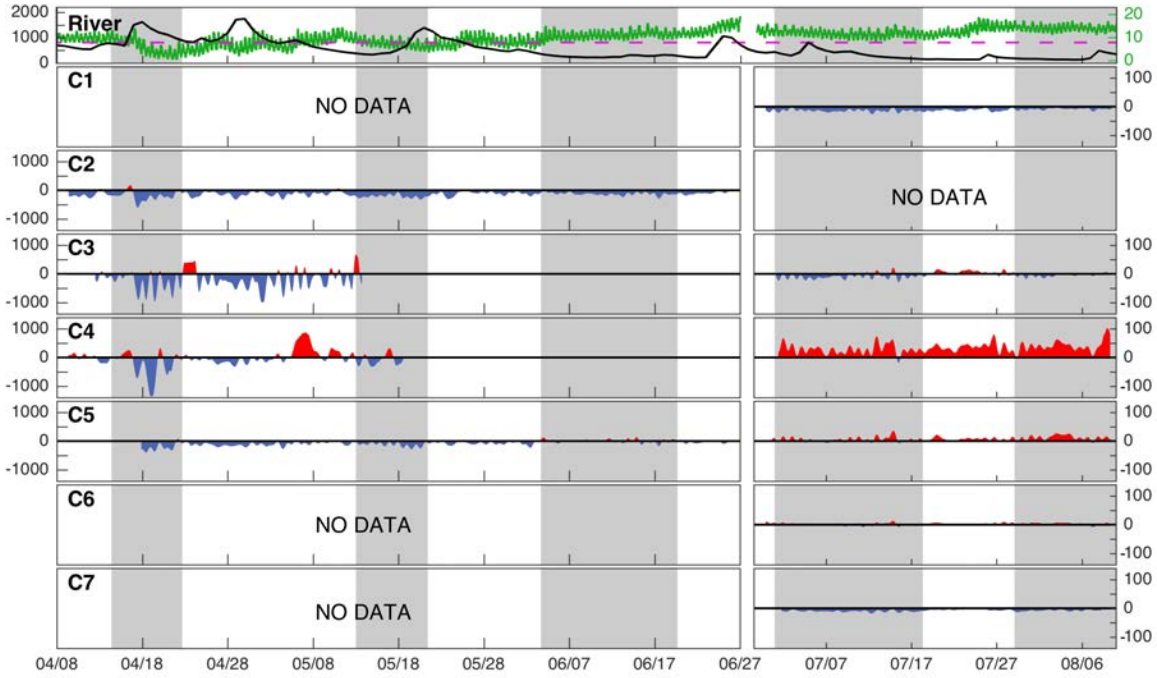

Figure 2.5 Instantaneous total along-channel sediment transport. (top) River discharge at Trenton (m^3 s^{-1}) in black and bottom salinity at the Coast Guard buoy in green. The purple dashed line denotes the bottom salinity at C5 during the along-channel survey 3–4 June. (bottom) Time series of instantaneous total along-channel sediment transport (g m^{-1} s^{-1}) at mooring locations C1–C7. Gray shading indicates spring tides, white indicates neap. Positive fluxes (red) signify import into the estuary, while negative fluxes (blue) indicate export.

2.5.3 Along-Channel Sediment Transport

2.5.3.1 Temporal Variability of Sediment Transport

Timeseries of depth-integrated instantaneous along-channel sediment transport derived for each mooring (Figure 2.5) reveal a pattern of persistent export in the spring and a transition to laterally variable transport direction in the summer. During the summer months, the flanks consistently exported sediment while the channel tended to

import it. Despite the predominance of export during the period of high river discharge, there were brief episodes of channel sediment import. The C3 mooring timeseries exhibits patterns that alternate between that typical of the flank and channel, indicating that this location may be transitional. The magnitude of transport on the exterior part of the flank (C1) was small (but consistent) compared to that closer to the channel (C2) due to increasing SSC and current strength towards the deeper channel (Figure 2.5).

Transient sediment transport events in the record most likely represent river discharge and wind events (Figure 2.5). Notably, the first river discharge pulse in mid-April drove sediment strongly down-estuary at all sites after a period of weaker transport. The April discharge event succeeded a relatively dry month (Figure 2.2a), so the heightened sediment delivery may have been caused by remobilization of sediment stored in the upper tidal river during the preceding month. There are other events in the record, such as in early May and mid July, during which all of the sites show variability in the direction of sediment transport. These events are consistent with fluctuations in the 2-5 day weather-band period, suggesting that they were associated with meteorologically forced barotropic flows, which have been shown to overwhelm the river discharge and flow both up and down the estuary (Aristizábal and Chant, 2015). Finally, the large landward pulse of sediment at mooring C4 around 3 May occurred when bottom salinity rose above 10 with diminishing river flow.

The strength of the total transport signal for both the channel and flank can be generalized with respect to river flow conditions. The integrated transport (Figure 2.6) illustrates that the high flow period was dominated by export through the whole cross section, with particularly strong fluxes on the DE side of the interior flank and edge of

the channel (sites C2 and C3). Note that the decrease in integrated transport around 3 May was associated with the landward pulse of sediment in the deep channel discussed above. The low flow period, on the other hand, was dominated by import in the channel that seemed to exceed the export over the flanks. Since C2 mooring data are unavailable for the latter half of the observational period, the total amount exported over the flank during the low flow period cannot be estimated; however, based on the available record, we would expect sediment to have been exported.

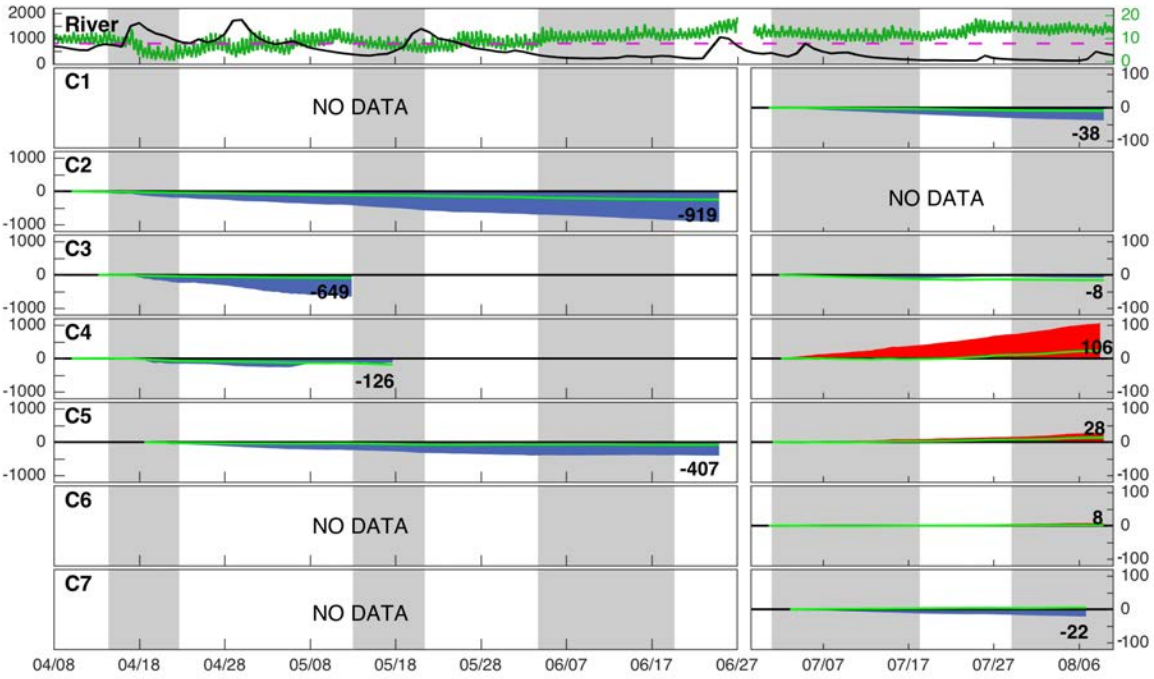

Figure 2.6 Integrated along-channel sediment transport per unit of width (metric tons m^{-1}) at mooring locations C1–C7 (bottom plots). The numbers are the last integrated value at the end of the specific deployment. The green lines show the integrated contribution by tidal pumping. All other aspects of the figure are consistent with Figure 2.5.

Due to the seasonality of river discharge, the pattern described above implies that there is a seasonal component to lateral variations in along-channel sediment transport. That is, during spring and early summer, significant amounts of sediment move down-estuary in the channel and flanks. Then, in late summer and early fall, sediment is

pumped back up-estuary in the channel while being exported over the flanks, but on a much smaller scale. The time-dependence of these sediment-transport pathways has important implications for the ultimate fate of suspended materials in the estuary. For example, sediment import within the channel during times of low river discharge may increase the residence time of sediment in suspension and perhaps contribute to its permanent entrapment within the estuarine system.

2.5.3.2 Decomposition of Sediment Fluxes

To evaluate the relative importance of tidal and non-tidal transport processes, we decomposed the timeseries of instantaneous along-estuary transport into tidal and mean components. Figure 2.7 shows the tidal pumping term at each mooring along with the percent contribution of tidal pumping to total sediment transport for each spring/neap tide. The percent contribution was calculated as follows:

$$\left[\left|\int_{t_o}^{t_f} Q_{st}\,\partial t\right| \Big/ \left|\int_{t_o}^{t_f}\left(Q_{st}+Q_{s\,mean}\right)\partial t\right|\right]\times 100 \qquad (1.11)$$

Due to the calculation method, the percent contribution of tidal pumping is less meaningful when the total transport is small (asterisks in Figure 2.7). Since there was a reversal in the direction of transport by mean advection at C4 during the neap tide 23 April to 12 May (Figure 2.8), we separated that calculation into two parts to yield more meaningful percent contributions. It is clear from the estimations in Figure 2.7 that tidal pumping contributes roughly 30% to total sediment transport.

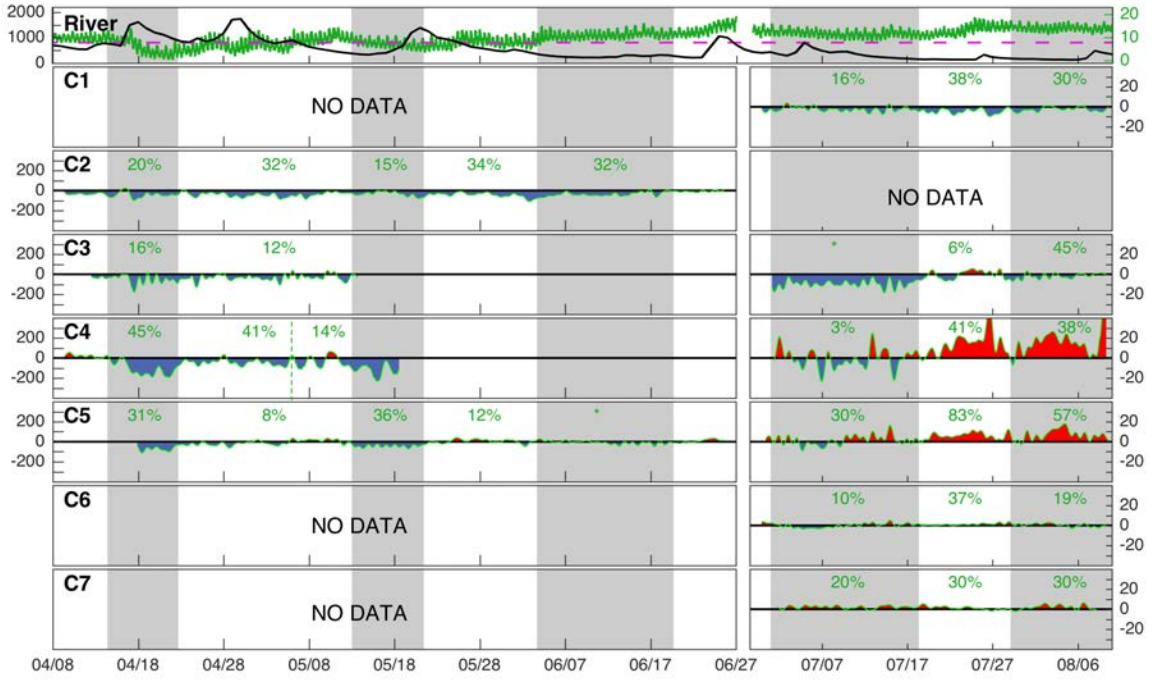

Figure 2.7 Instantaneous along-channel sediment transport by tidal pumping alone (g m^{-1} s^{-1}) at mooring locations C1–C7 (bottom plots). The green numbers show the percent contribution of tidal pumping for each mooring each spring-neap tide. The neap tide 23 April to 12 May at C4 is separated into two parts to account for the change in sign of mean transport. The green stars represent times when the tidal pumping contribution calculation is not meaningful due to the very weak sediment transport. All other aspects of the figure are consistent with Figure 2.5.

The spatial pattern of sediment transport by tidal pumping (Figure 2.7) is very similar to that of the total along-estuary transport. There is steady export at all locations during the higher river discharge period, but during lower river discharge there is a transition to export on the DE flank and import in the channel. The transport on the NJ flank is much weaker and the direction is variable. There is some spring-neap variability, though the signal is subtle and is spatially variable. On the flanks, there is more transport during neap tides compared to spring; in the channel, there is stronger transport by tidal pumping during spring tides.

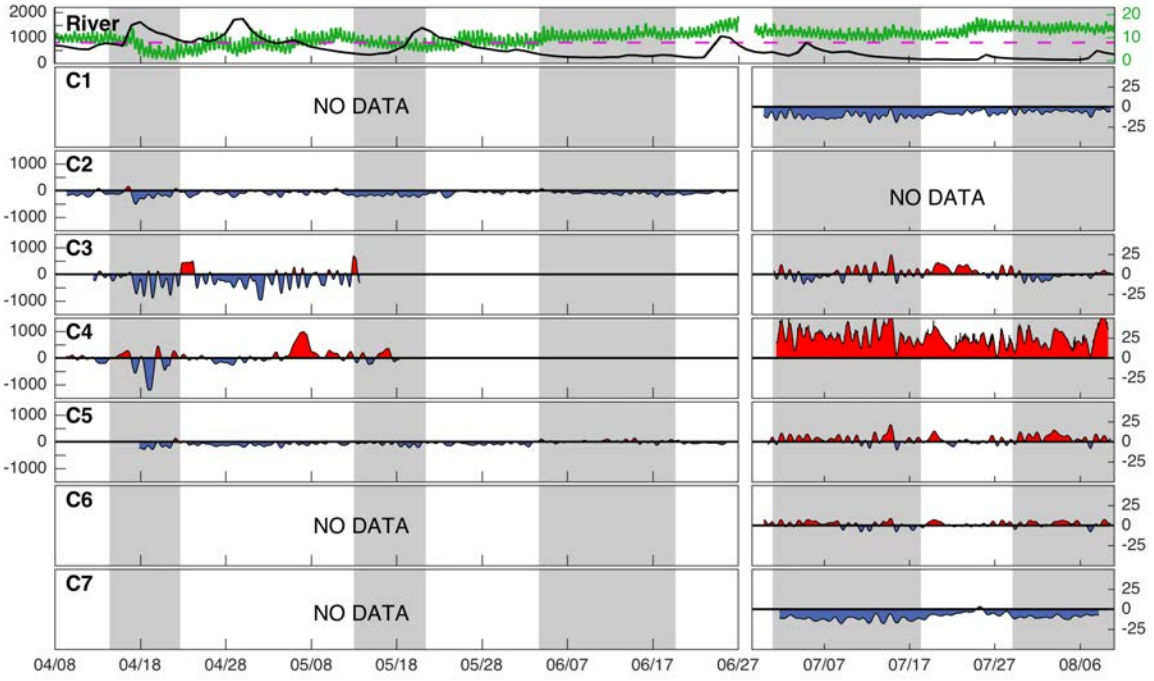

Figure 2.8 Instantaneous along-channel sediment transport by mean advection (g m^{-1} s^{-1}) at mooring locations C1–C7 (bottom panels). All other aspects of the figure are consistent with Figure 5.

Figure 2.8 shows the along-estuary sediment transport by mean advection alone. Notably, the spatial patterns are generally consistent with those described for tidal pumping. On the DE flank mean advection consistently drives sediment export, whereas the transport in the channel transitions from export to import as the river discharge weakens. Since the mean advective term contains both the riverine signal and estuarine exchange (e.g., gravitational circulation), we interpret the change in sign observed in the channel to relate to the dominant process driving advection. In the spring, advection down-estuary is likely controlled by river discharge and laterally-sheared exchange flow, whereas in summer, advection up-estuary may be driven by vertically-sheared exchange flow. The magnitude of sediment transport by mean advection is often greater than that driven by tidal pumping, but there are instances of fluctuating transport (latter half of the C3, C5 and C7 records) that result in mean advection contributing very little to the

integrated total transport. The mean advective transport (Figure 2.8) contains many sediment pulses, including those in response to river discharge and meteorological events, which clearly impact the total sediment transport (Figure 2.5).

The similar spatial and temporal patterns of mean advection and tidal pumping provide evidence that these two mechanisms are generally complementary. Mean advection tends to drive the total sediment transport, but tidal pumping contributes roughly 30% of the total. Though tidal pumping is variable, it is more directionally persistent. Thus, it is a particularly important transport mechanism during times of fluctuating transport by mean advection.

The sediment transport decompositions highlight the variable importance of tidal pumping, but further analysis is necessary to determine the cause of the variability. Figures 2.9 and 2.10 illustrate the decompositions for DE flank and channel mooring locations along with the coincident stratification for the first and second deployments, respectively. Since the river discharge conditions were quite different between the two deployments, Figures 2.9 and 2.10 are representative of how dynamics may differ in response to river flow. The magenta and yellow dots in plots C and E indicate the stratification at the end of flood and the end of ebb, highlighting the variability of tidally-controlled stratification at each site. Mooring C1 was selected to represent the flank dynamics during the low flow period due to C2 burial by muddy sediment early in the deployment.

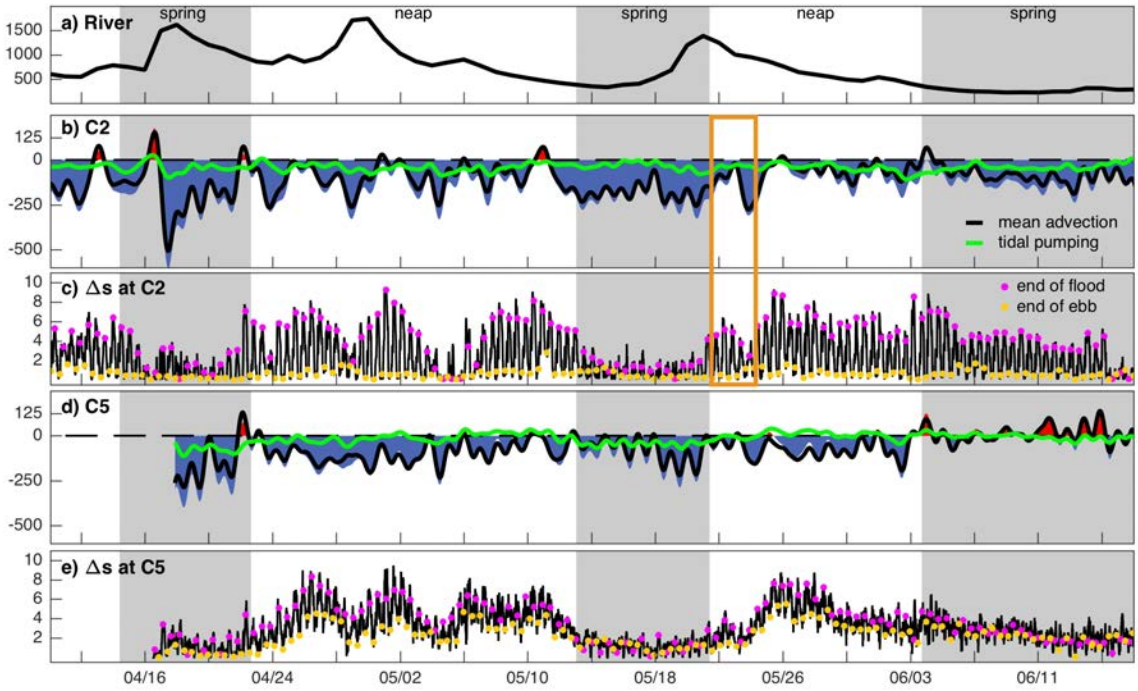

Figure 2.9 Channel-flank comparison of sediment transport and stratification during high river flow conditions. (a) River discharge (m3 s^{-1}) at Trenton. (b) Time series of the instantaneous along-channel total sediment transport (g m^{-1} s^{-1}) at C2 (DE flank) during the high flow deployment. The black line is the mean advective component of the flux and the green is the tidal pumping. (c) Stratification (psu) calculated by (bottom salinity-surface salinity) for C2. The magenta points indicate end of flood and the yellow points indicate end of ebb. (d) Same set up as Figure 2.9b but for C5. (e) Same set up as Figure 2.9c but for the Coast Guard buoy, located near C5. The gray shading highlights spring tides and white highlights neap. The orange box indicates the zoomed in period discussed in Figure 2.13.

There were large changes in stratification of the DE flank on a tidal timescale, with a clear spring-neap modulation of the stratification asymmetries (Figures 2.9c and 2.10c). For most of the observational period, the DE flanks experienced enhanced stratification at the end of flood tides. During spring tides and high river flow, for instance 14-22 April and 13-21 May, tidal variability in stratification was significantly reduced (Figure 2.9c) and tidal pumping had a weaker signal (Figures 2.9b and 2.7-C2). The combination of neap tides and high river flow, such as 23 April to12 May and 22 May to 2 June, created large tidal fluctuations of stratification on the flank and coincided with strong tidal

pumping. During times of low river flow, the spring-neap modulation of stratification asymmetries was weaker on the flank, but tidal pumping was elevated during the neap tide when tidal period variability in stratification was most pronounced, around 24-28 July (Figure 2.10b and 2.10c). Though the spring-neap variability of stratification on the flanks is apparent (Figures 2.9 and 2.10), the spring-neap variability of the tidal pumping signal is comparatively muted (Figure 2.7). We posit that this muted spring-neap transport signal results from competitive mechanisms: reduced tidal variability in stratification during spring tides would drive weaker transport whereas the stronger currents during spring tides would drive stronger transport. Since sediment transport by tidal pumping on the DE flank is stronger during neap tides, enhanced tidally asymmetric stratification is likely the more important mechanism controlling spring-neap variability of tidal pumping.

Stratification in the channel also varied on a tidal timescale (Figures 2.9e and 2.10e), though the tidal variability was much smaller than that observed on the DE flank (Figures 2.9c and 2.10c). For example, during the high river discharge period stratification tended to be greatest at the end of flood (Figure 2.9e) whereas during the low river discharge period stratification was often enhanced at the end of ebb (Figure 2.10e). This change coincides with tidal pumping transitioning from an export mechanism to an import mechanism. There was also spring-neap modulation of the baseline stratification in the channel, with stronger stratification during neap tides. Since tidal pumping was a stronger contributor during spring tides in the channel (Figure 2.7), it is likely that the stronger currents during spring tides drive the spring neap variability of sediment transport by tidal pumping. To elucidate the complex variability of tidal pumping in the

channel, in section 2.6.1 we look more closely at the driving mechanisms.

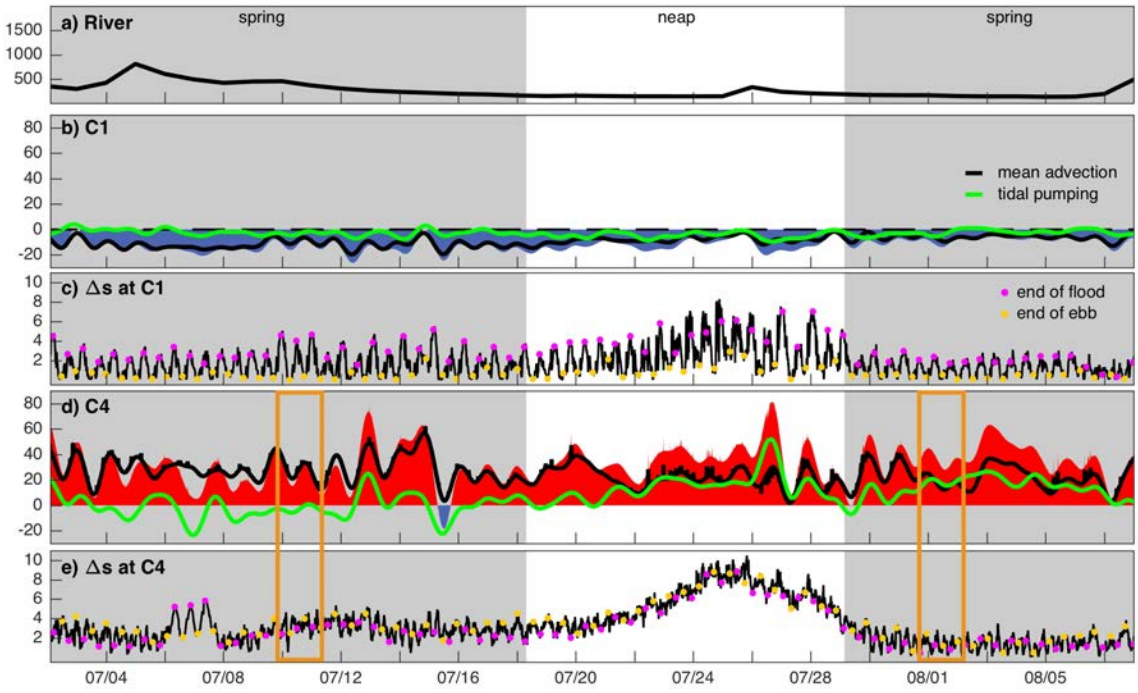

Figure 2.10 Channel-flank comparison of sediment transport and stratification during low river flow conditions. Same design as Figure 2.9, except for C1 (DE flank) and C4 (channel), respectively, during the low discharge deployment. The orange boxes indicate the zoomed in periods dis- cussed in Figures 2.14 and 2.17

2.5.4 Across-Channel Sediment Transport

The depth-averaged, instantaneous across-channel sediment transport at each mooring (Figure 2.11) revealed that there was divergence on the DE flank, with sediment moving towards the DE coast of the estuary at C2 and towards the NJ coast at C4. Lateral transport was extremely weak at C3 through both deployments. There was a convergence on the NJ side, centered between C4 and C5 during high river discharge and between C5 and C6 during low discharge. Unlike the along-channel sediment transport, the lateral fluxes in the channel did not change direction when the river discharge weakened. The

lateral variability in across-channel sediment transport was consistent over both deployments.

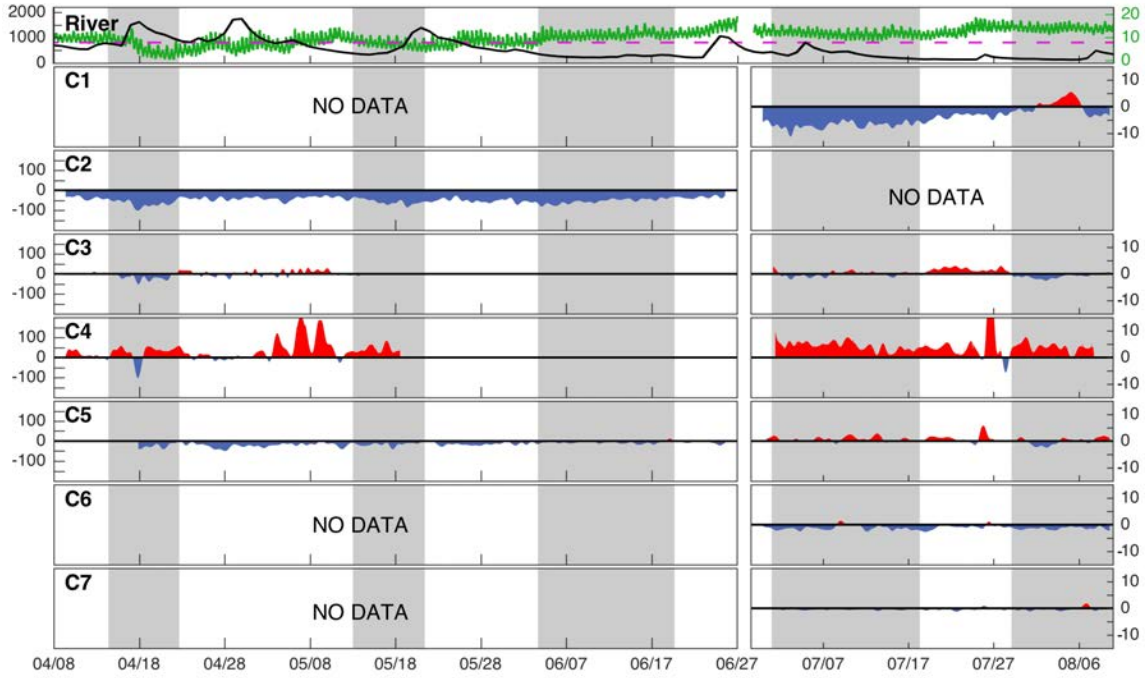

Figure 2.11 Instantaneous total across-channel sediment transport (g m^{-1} s^{-1}) at mooring locations C1–C7 (bottom plots). Gray shading indicates spring tides, white indi- cates neap. Positive fluxes (red) signify transport toward NJ, while negative fluxes (blue) indicate transport toward DE.

There were a few peaks in lateral transport, such as those around 18 April, 8 May, and 27 July, that were episodic and associated with river discharge pulses and meteorological events, as discussed in section 2.5.3.1. There was no apparent spring neap variability, and the fluxes were quite steady.

Notably, the across-channel sediment transport (Figure 2.11) was roughly an order of magnitude less than the along-channel transport (Figure 2.5). However, despite the magnitude differences of the instantaneous transports, the time-integrated across-channel and along-channel fluxes were of similar magnitude at the C2 and C4 locations, where lateral sediment transport was high (Figure 2.12). The lateral integrated fluxes at C2 and

C4 were particularly large because the instantaneous fluxes were quite steady. It is worth noting that, similar to the along-channel transport, the across-channel transport at C2 was more than three times that at C4.

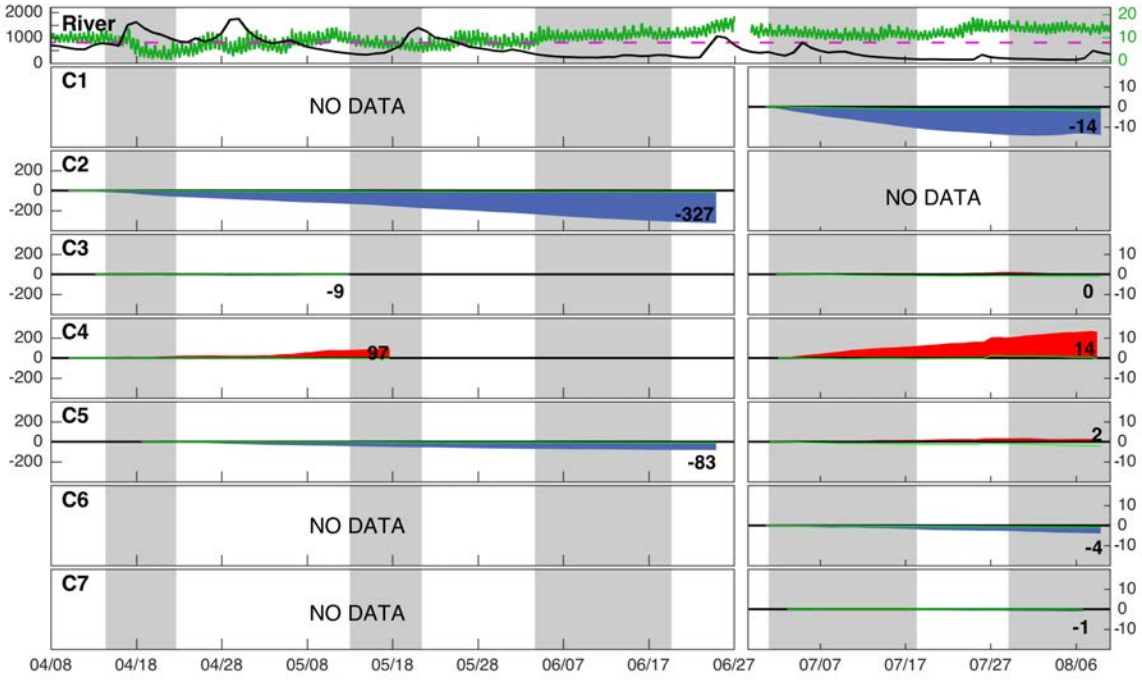

Figure 2.12 Integrated across-channel sediment transport per unit of width (metric tons m-1) at mooring locations C1-7 (lower panels). The numbers are the last integrated value at the end of the specific deployment. The green lines show the integrated contribution by tidal pumping. Positive fluxes (red) signify transport towards NJ, while negative fluxes (blue) indicate transport towards DE. All other aspects of the figure are consistent with Figure 2.11.

The integrated across-channel transport (Figure 2.12) highlights that there was persistent divergence on the DE flank, with sediment being moved from C2 and C1 toward the outer flank and from C4 toward the channel. The green lines in Figure 2.12 represent the integrated contribution by tidal pumping alone. It is clear that contribution from tidal pumping was negligible at all mooring sites, suggesting that mean lateral circulation was the primary control on across-channel sediment transport.

2.6 Discussion

2.6.1 Along-Channel Sediment Transport by Tidal Pumping

Two distinctive along-channel sediment-transport regimes are evident from the observations: (1) when tidal pumping contributed more significantly and (2) when tidal pumping was weak. To further explore why tidal pumping was so variable, we separated the data according to the relative contribution of tidal pumping to total transport. If tidal pumping contributed more than 30% of the total sediment transport at a given time, the data were categorized into the tidal pumping regime. Likewise, if the contribution was less than 30% of the total sediment transport, the data were categorized into the mean advective regime. Within the tidal pumping regime, the data were further separated to distinguish the mechanisms driving export from those driving import.

When tidal pumping was an important contributor, tidal asymmetries in stratification were key to the transport mechanism (Figures 2.9 and 2.10). From a synoptic picture of C2 on the DE flank, it is evident that stratification on a tidal timescale was opposite to that predicted by the axial tidal straining mechanism – stratification was strengthened over the flood and weakened on ebb (Figure 2.13). These stratification asymmetries are consistent with similar observations in other systems, such as the York and Chesapeake (Fugate et al., 2007; Scully and Friedrichs, 2007b), and underscore the importance of lateral processes in sediment transport. This stratification variability on the flank was driven by both along-channel advection of stratification and straining of the lateral density field (Aristizábal and Chant, 2014). In contrast, stratification within the channel during low river discharge conditions was consistent with that driven by the tidal straining mechanism, with stratification enhanced on ebb (Figure 2.14). These

observations agree with previous observations of stratification in the Delaware channel (Aristizábal and Chant, 2014) and indicate that along-channel processes overpower lateral straining in the channel at times. Tidal asymmetries in stratification thus may vary both spatially and temporally, which has significant implications for sediment transport.

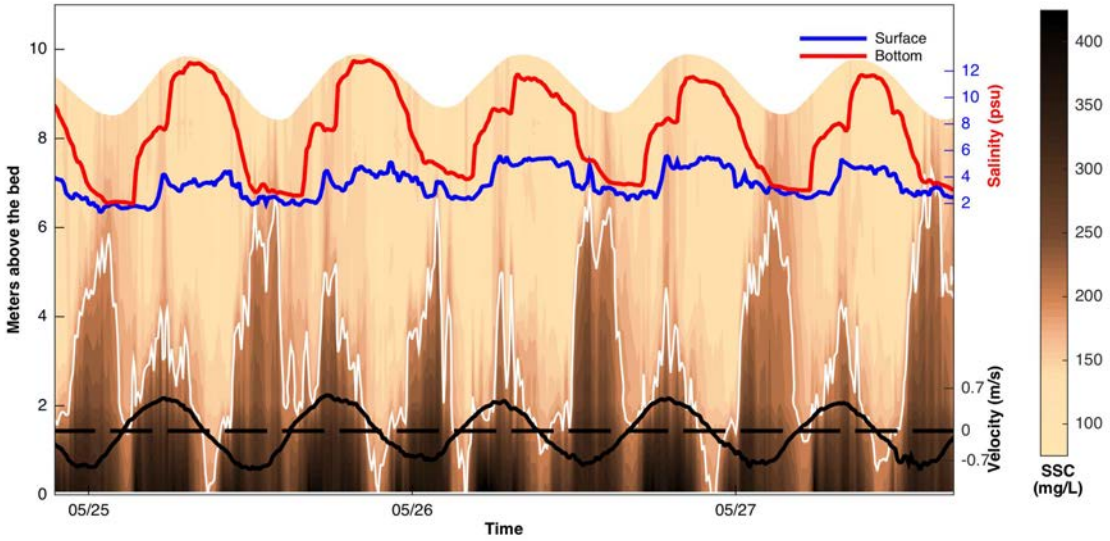

Figure 2.13 Timeseries at C2 mooring during a period of strong tidal pumping. Zoomed in image of sediment (brown colormap, mg/L), surface salinity (blue, psu), bottom salinity (red, psu), and depth-averaged along-channel velocity (black, m/s). The 225 mg/L contour is outlined in white.

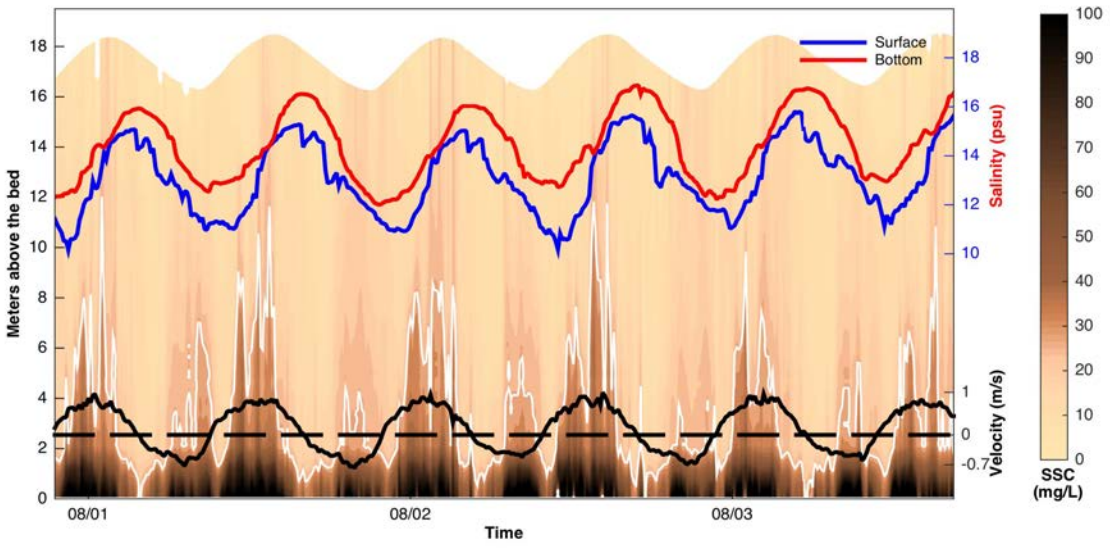

Figure 2.14 Timeseries at C4 mooring during a period of strong tidal pumping. Same layout as Figure 2.13, but the 30 mg/L contour is outlined in white.

Sediment export by tidal pumping can be explained by the coupled asymmetry of stratification and sediment resuspension. Data from 25 to 28 May at C2 illustrates that stratification on the flank was weak on ebb, resulting in higher resuspension of sediment and a longer settling time as the ebb relaxes (Figure 2.13). The enhanced stratification on flood limited resuspension to lower in the water column, and settling was quicker at the end of the flood tide. Since the tidal currents were symmetric, the stratification and resuspension asymmetries resulted in an ebb-driven flux down-estuary on the flanks. Moreover, with a vertically sheared flow, sediment flux was also elevated on ebb due to the greater currents aloft.

To corroborate the transport conditions over a few days, all of the C2 data identified by the tidal pumping regime were analyzed in terms of the height of resuspension, current velocities, and stratification. As illustrated in Figure 2.15, it is clear that enhanced stratification and weaker sediment resuspension were consistent features of the flood tide over the entire dataset. The dataset contains a range of stratification cases, including the

weakened stratification during spring and the enhanced during neap (Figure 2.9c), yet the pattern of tidally asymmetric stratification was consistent. Thus, we posit that the flood-ebb tidal asymmetry provides a mechanism to export sediment on the flank.

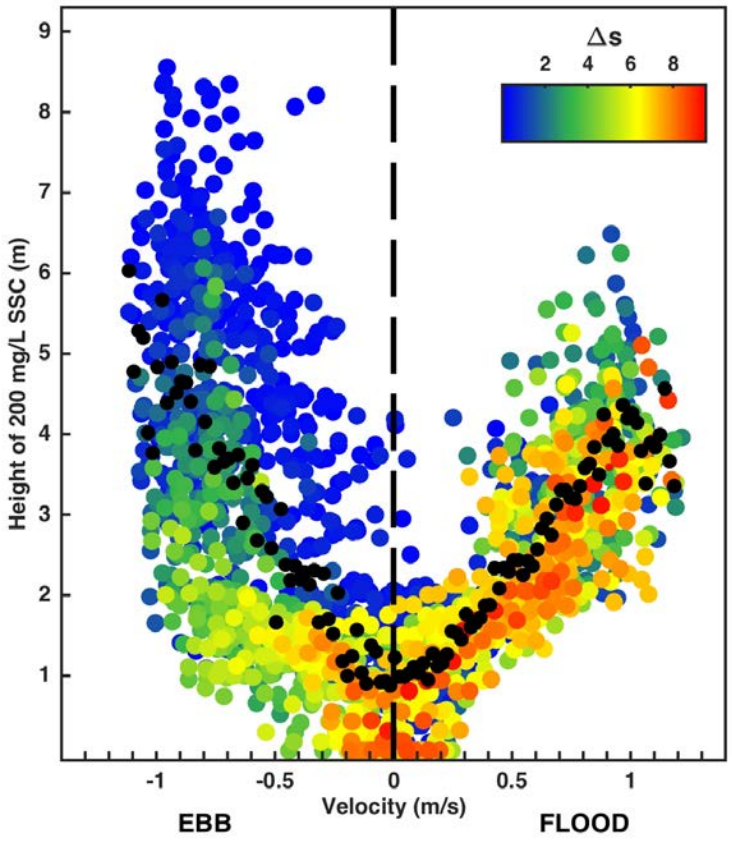

Figure 2.15 Data from C2 (DE) flank during the tidal pumping regime when sediment is exported. Colors represent stratification (calculated as the difference between bottom and surface salinity). Velocity is in m/s. Height of the 200 mg/L concentration is given in meters off the bed. The black dots represent the tidal phase averaged data.

The import of sediment by tidal pumping in the channel during low river discharge was also driven by asymmetries in stratification and resuspension. A snapshot of a 4-day record at C4 shows enhanced stratification on ebb that limits resuspension to lower in the water column (Figure 2.14). There was also a delayed resuspension response to increasing ebb velocities, suggesting that the stratification buffered the shear stress at the

bed. The water column became relatively well mixed on flood and strong currents generated resuspension high into the water column, resulting in a consistent, flood-driven sediment flux up-estuary. This mechanism is confirmed by the consistency of these attributes in all of the channel data where tidal pumping drives import (Figure 2.16). The asymmetry in stratification is somewhat obscured in Figure 16 since the data encompass a large range of stratification conditions, but change in stratification on the tidal timescale was consistent for each tidal cycle.

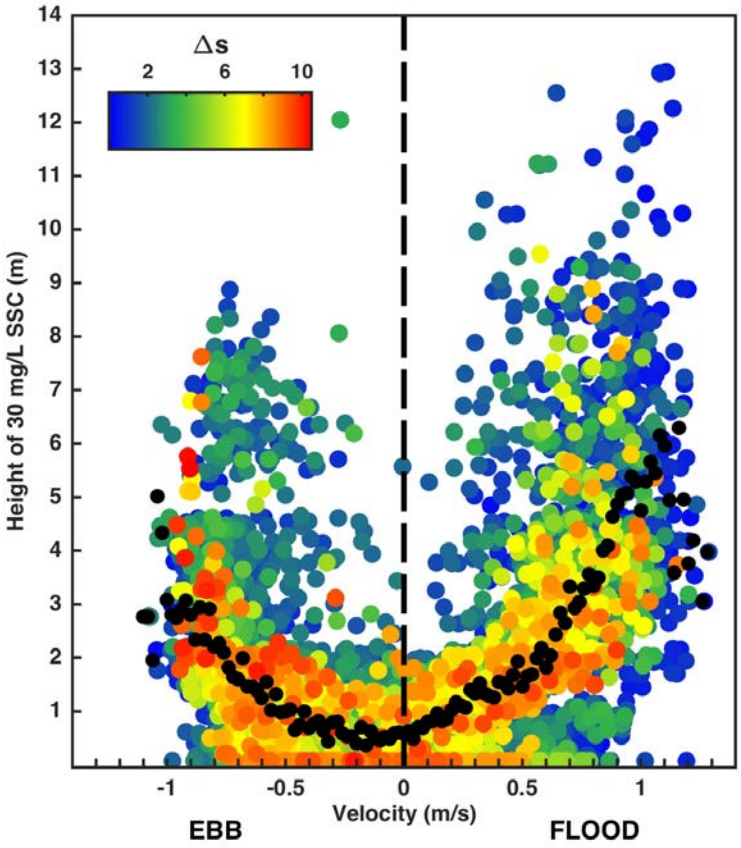

Figure 2.16 Data from the C4 mooring during the tidal pumping regime when sediment is exported. Height of the 30 mg/L concentration is given in meters above the bed. All other aspects of figure are the same as Figure 2.15.

Within the mean advective regime, stratification conditions were highly variable. Thus, data from C4 during a time of weak tidal pumping were isolated to determine why

tidal pumping is sometimes extremely weak (Figure 2.17). As shown in Figure 2.17, it is evident that stratification was relatively constant over the tidal timescale, perhaps due to balance between the along-channel straining of the density field and lateral-straining by cross-channel flows. Because of the persistent stratification in channel, the heights to which sediment was resuspended at peak ebb and peak flood were roughly similar. The lack of tidal asymmetries resulted in weak tidal pumping, and thus the depth-averaged mean flow drove the sediment transport. In the timeframe shown in Figure 2.17, there was a mean depth-averaged inflow of 0.03m/s that drove sediment into the estuary. While the stratification conditions may vary quite substantially during times of weak tidal pumping, it is the lack of stratification variability on a tidal timescale that ultimately shuts down the tidal pumping transport mechanism.

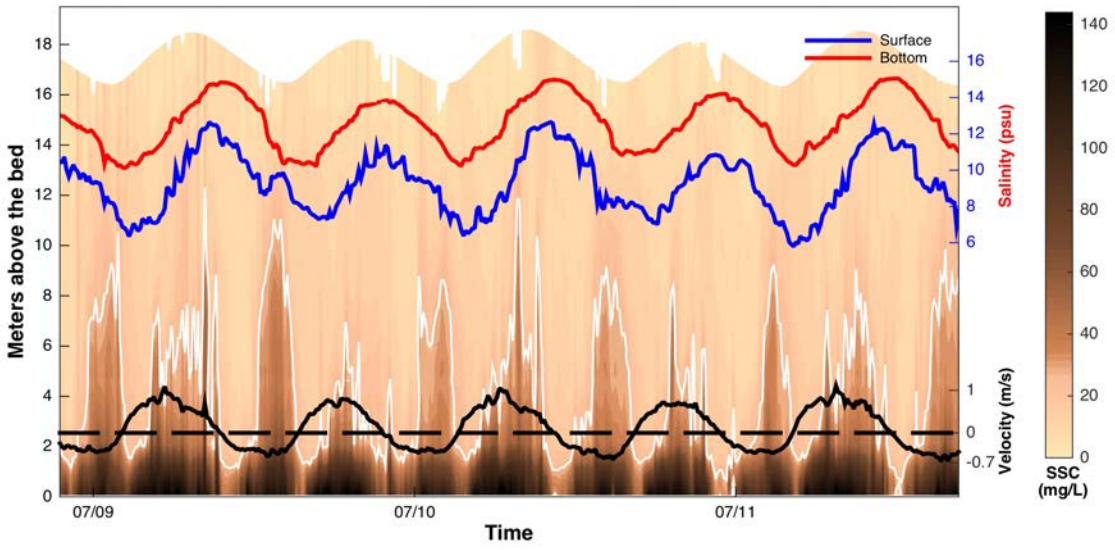

Figure 2.17 Timeseries at C4 mooring during a period of weak tidal pumping. Same layout as Figure 2.13, but the 30 mg/L contour is outlined in white.

2.6.2 Three-Dimensional Structure of Sediment Transport in the ETM Zone

The ETM zone traps sediment in an estuary through the convergence of mean advective and tidal sediment fluxes (Wellershaus, 1981; Geyer, 1993b; Burchard and Baumert, 1998). Cook et al. (2007) suggest that tidal pumping is an important mechanism maintaining the Delaware's ETM, particularly during periods of weak river discharge. They describe trapping to be dominated by a landward flux in the estuarine reach that overwhelms weaker landward fluxes in the tidal freshwater reach of the river. Our observations cannot quantify convergence, but do characterize the variability of the flux in the estuarine reach of the basin. While we also demonstrate that tidal pumping imports sediment in the channel during low river discharge conditions, our observations further reveal seaward sediment tidal pumping in the main channel during high river discharge. Moreover, our observations highlight persistent export due to tidal pumping on the Delaware flank, which occurs due to the enhancement of stratification at the end of flood relative to the end of ebb. While this tidal period variability in stratification is contrary to the classic model of axial tidal straining (Simpson et al., 1990), it has been documented to also occur in other estuarine systems (Fugate et al., 2007; Scully and Friedrichs, 2007b).

Interestingly, whereas tidal pumping is an important mechanism of along-channel sediment transport, it had very little impact on across-channel fluxes during the observational period. This is attributed to the fact that axial and lateral flows in the Delaware Estuary are out of phase such that the strongest cross-channel currents occur at slack water (Aristizábal and Chant, 2014). Since sediment settles to the bed at slack water, there is little sediment resuspended in the water column when tidal across-channel

flows are strongest. Hence, the across-estuary sediment fluxes due to tidal pumping are relatively weak.

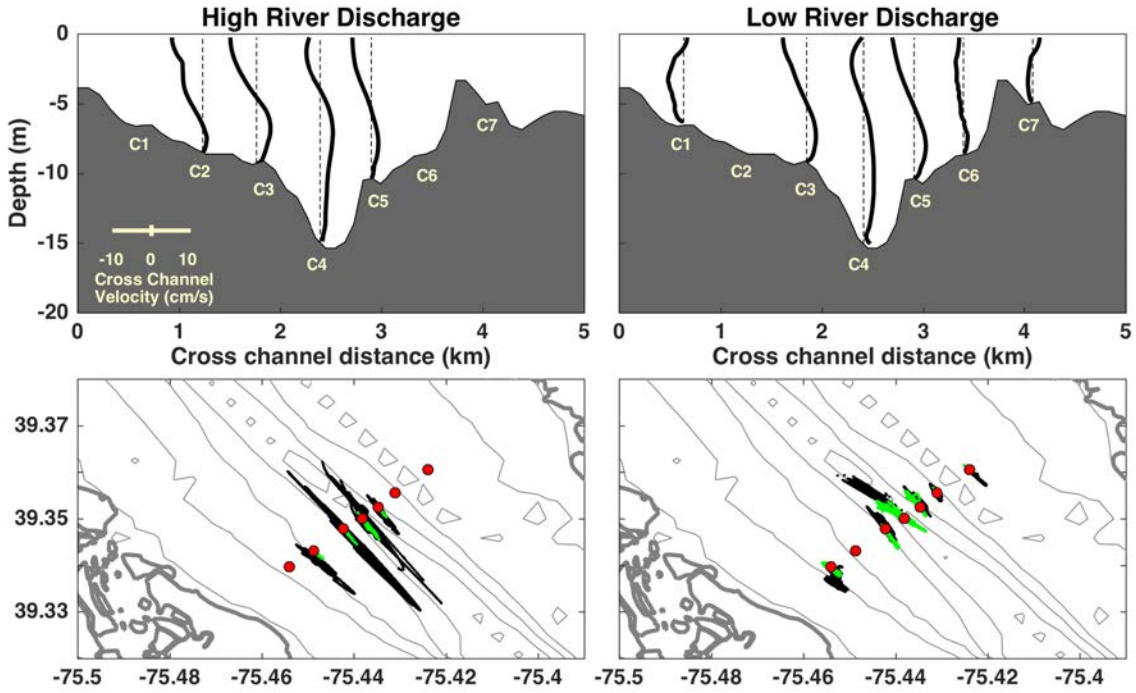

Figure 2.18 Mean cross-channel flows and mean advective sediment transport. (top) The mean cross-channel flow for (left) high and (right) low river discharges. (bottom) The corresponding maps of sediment transport by mean advection (black) and tidal pumping (green). The low river discharge case (bottom right) is an order of magnitude less in vector space than the high river discharge case.

The across-channel mean flow at each mooring and plan views of sediment transport in the ETM zone by mean advection and tidal pumping are shown in Figure 2.18 for high and low river discharge periods. Since across-channel transport is controlled almost entirely by mean advection, the residual across-channel velocity profiles highlight the divergence on the DE flank (Figure 2.18, top). Given the shear in the mean across-channel flow, we would expect a sediment transport towards the NJ coast at most locations (Figure 2.18, bottom). This is consistent with our estimates at C3 and C4 during both deployments and C5 during the low flow deployment. The sheared mean across-channel velocities suggest that the supply of sediment to the DE flank by the

along-channel sediment transport is then laterally transported to the deep channel. Notably, there is also a lateral transport of sediment from C2 towards the wetland coast which is driven by a depth-averaged mean flow towards DE. As the onshore flow must be balanced by an off-shore return flow off elsewhere to satisfy continuity, this non-zero mean flow highlights that there are three-dimensional flows unresolved by this dataset. It is thus likely that the mean-driven sediment export toward the wetland coast of the estuary is not a spatially persistent feature. The observed mean lateral flows are consistent with rotationally forced flows modified by bathymetry (Valle-Levinson et al., 2003). While tidally-variable lateral flows in this system have been shown to be driven by rotation and cross-channel density gradients (Aristizábal and Chant, 2014), detailed analysis of the subtidal flows are beyond the scope of this paper. Further work, involving numerical modeling and additional observations, is needed to explore the subtidal cross-channel circulation and lateral transport processes in full.

The spatial variability of sediment transport provides evidence that the ETM is laterally strained. When the river discharge is high, the transport on the DE flank is strongly down estuary and toward the DE coast while the transport in the channel fluctuates up-estuary and down-estuary with some transport towards the NJ coast. When the discharge is low, transport in the channel is into the estuary and toward NJ, while transport on the flank is down-estuary and toward DE. This spatial structure demonstrates that the flanks may export sediment out of the ETM zone towards the wetland coast of the estuary or to the upper bay, whereas the channel may be a mechanism of re-entraining sediment that has moved down the flank, into the channel, and back up-estuary (Figure 2.19). The mean lateral shear would facilitate cross-channel

sediment transport towards the channel, where it may be transported back up estuary during low flows. While sediment transport is much stronger during high river flows, low discharge conditions occur most of the year and would result in landward transport. Thus, the cumulative effect of the sediment recycling and import during the dry seasons could contribute significantly to the trapping efficiency of the ETM.

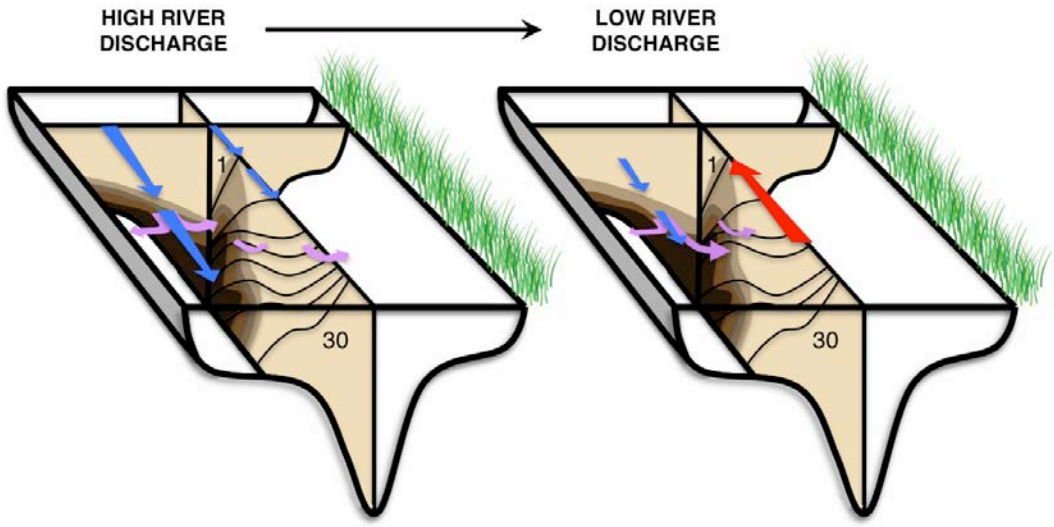

Figure 2.19 Schematic of the three-dimensional ETM structure influenced by lateral variability of along-channel sediment transport and divergence in across-channel transport on the DE flank. Blue arrows indicate export whereas red arrows indicate import. Purple arrows represent the observed across-channel transport at the mooring line.

2.7 Conclusions

Along-channel sediment transport in Delaware Estuary is driven primarily by mean advection, with tidal pumping accounting for about 1/3 of the total transport. These sediment transport mechanisms have distinct cross-channel variabilities that contribute to lateral straining of the ETM zone. Sediment transport by mean advection and tidal pumping have complementary spatial and temporal variability, contributing to a robust sediment transport pattern. Both mechanisms drive sediment export throughout the

estuary during high river discharge, but when river discharge weakens, they drive import in the channel and export on the flank. The variable transport associated with tidal pumping relates directly to tidal asymmetries in stratification and sediment resuspension. When tidal pumping drives import in the channel, stratification is strengthened during the ebb tide as predicted by axial tidal straining. Consequently, sediment is resuspended higher in the water column on flood tides and subjected to strong flood currents, resulting in a sediment flux up-estuary. When tidal pumping drives sediment export, lateral circulation and axial advection contribute to enhanced stratification on flood, which facilitates ebb-driven export.

Across-channel sediment fluxes also have a pattern of lateral variability that has important implications for total sediment transport. There is an area of divergence on the inner DE flank where sediment is moved towards the both the channel and wetland coast. These lateral fluxes are steady, transporting a significant amount of sediment on the flank. The lateral shear in the mean cross-channel flows facilitates transport from the DE flank into the deeper channel, possibly enhancing entrapment. The across-channel sediment transport is driven primarily by the mean circulation, as tidal pumping is observed to be extremely weak.

Our observations of spatially variable sediment transport in the Delaware Estuary emphasize that lateral processes strongly influence along-estuary and across-estuary transport. These observations shed light on the three-dimensional nature of estuarine sediment dynamics and provide new insights about sediment transport processes and pathways. Asymmetries in stratification facilitated by cross-channel flows enable sediment export by tidal pumping, particularly on the shallower flanks. These results

expand on the classic notion that sediment transport is primarily landward due to longitudinal baroclinicity, and suggest that observations based solely in the channel may overestimate the total entrapment of sediment in the ETM by excluding a key export mechanism. In order to better understand the three-dimensional nature of the ETM, we must further explore the unresolved circulation and the longitudinal variability of lateral flows to characterize the spatial patterns of channel-flank connectivity.

2.8 Acknowledgements

We thank Eli Hunter and Maria Aristizábal for their dedication to the field campaign and their insightful feedback during analysis. We also appreciate the efforts by Chip Haldeman, Ken Roma, and the *R/V Hugh Sharp* crew. We are grateful to two anonymous reviewers, whose careful insight led to great improvements in the paper. Data collection was funded through National Science Foundation grants OCE-0928567 and OCE-0825833 to R. Chant, and OCE-0928496 to C. Sommerfield. This material is also based upon work supported by the Institute of Marine and Coastal Sciences at Rutgers University and the National Science Foundation Graduate Research Fellowship under grant no. DGE-0937373. The data collected in this study can be accessed by contacting Robert J. Chant at chant@marine.rutgers.edu.

Chapter 3: Modeling Spatiotemporal Variability of Residual Sediment Fluxes in Delaware Estuary

3.1 Abstract

Spatial and temporal variability of sediment transport processes within an estuarine turbidity maximum (ETM) ultimately impact the trapping efficiency of a system. A Regional Ocean Modeling System (ROMS) coupled hydrodynamic and sediment model is used to evaluate the spatiotemporal variability of residual circulation and sediment transport in the Delaware Estuary. At seven cross-sections along the estuary's axis, the vertical structure of the annual-mean axial and lateral velocities are described. These are linked to a map of depth-averaged velocities, illustrating the complex structure of residual circulation caused by variable lateral bathymetry. The residual annual-mean sediment transport is similarly shown at these transects and from a plan view, detailing a pattern of sediment export along the shallow flanks and import within the deeper channel as well as a pattern of lateral sediment flux divergence in the middle reach of the ETM. To identify seasonal variability of residual sediment transport spatial patterns, data from both high and low river discharge periods are isolated. Maps of the mean depth-integrated sediment transport during these periods demonstrate that the along-estuary sediment transport pattern is significantly modulated by river discharge. In contrast, the across-estuary pattern does not vary seasonally but is influenced by tides and local topography. Timeseries at three locations reveal that spring-neap variability of residual sediment transport is spatially specific and that axial and lateral fluxes are modulated differently on spring-neap timescales due to the orthogonal flows being out of quadrature. Ultimately, this analysis demonstrates that spatial patterns on spring-neap, seasonal, and annual timescales drive along-channel sediment convergence and lateral fluxes that both laterally strain the ETM and reinforce sediment trapping.

3.2 Introduction

Estuaries have long been known to trap riverine and coastal sediment due to near bottom convergence and flocculation (Postma, 1967; Schubel, 1968; Meade, 1969). The estuarine turbidity maximum (ETM), a region of elevated suspended sediment concentrations (SSC) and intense sediment deposition, typically resides near the salt intrusion and is particularly important to the trapping and storage of sediment within an estuary. Classically, ETM formation is attributed to the convergence of the seaward flux driven by mean river discharge and the landward flux due to baroclinic estuarine flows. In recent decades, research has focused on different mechanisms that contribute to the ETM formation and impact a system's trapping efficiency. These mechanisms include asymmetries in stratification (Geyer, 1993b), velocity shear (Jay and Musiak, 1994; Burchard and Baumert, 1998), turbulent mixing (Scully and Friedrichs, 2007b), bed-stress (Scully and Friedrichs, 2007a), and lateral circulation (Becherer et al., 2015).

Since these asymmetries are controlled by river discharge, tides, and wind, sediment transport mechanisms ultimately vary on tidal, spring-neap, and longer timescales. For example, in the York River Estuary tidal-pumping by flood tides have been observed to drive an up-estuary sediment flux at both channel and shoal sites (Scully and Friedrichs, 2007a). Conversely, in the Delaware Estuary tidal pumping drives an up-estuary sediment flux in the channel and down-estuary sediment flux on the Delaware shoal (McSweeney et al., 2016a), exemplifying that tidal asymmetries in sediment transport can vary spatially within a single system. Similar to tidal variability, spring-neap variability of sediment transport differs among individual estuaries. In the Hudson Estuary and York River Estuary spring tides tend to drive a strong landward sediment flux (Geyer et

al., 2001; Scully and Friedrichs, 2007a). In the Delaware Estuary neap tides are dominant on the flank and spring tides are dominant in the channel but the direction of the fluxes is controlled by the seasonal conditions (McSweeney et al., 2016a). River discharge dominates sediment transport on longer timescales, with seasonal freshets and storm events delivering considerable amounts of new sediment to the turbidity maximum and/or exporting reworked sediment seaward of the ETM (Geyer et al., 2001; Cook et al., 2007; Ralston and Geyer, 2009; Cheng et al., 2013).

While efforts to characterize estuarine sediment transport mechanisms has been ongoing, there has been a recent focus on how transport mechanisms vary spatially. The cross-channel bathymetry characteristic of estuaries can drive a lateral circulation that modulates the lateral salinity gradient and impacts sediment distribution and resuspension (Huijts et al., 2006; Huijts et al., 2011; Ralston et al., 2012; Aristizábal and Chant, 2014; McSweeney et al., 2016a). Furthermore, lateral variations in stratification, bed stress, and resuspension can cause the dominant sediment transport mechanisms to vary between an estuarine channel and shoal. Bathymetric features can also produce salinity fronts and sediment convergence, ultimately creating depositional hotspots (Valle-Levinson et al., 2003; Ralston et al., 2012). Since the spatial variability of sediment transport mechanisms is system-specific, broadly understanding the impact that it has on the trapping efficiency of an estuary is extremely challenging and remains an open research question.

Our knowledge of spatiotemporal sediment transport patterns in the Delaware Estuary has improved significantly in the last decade. Observations of tidal sediment fluxes at two locations 40 km apart in the upper-estuary channel revealed that tidal pumping is an

important sediment transport mechanism in the ETM but less so further up-estuary where bed-sediment becomes depleted early in the tidal cycle (Cook et al., 2007). Furthermore, the relative importance of tidal and advective transport mechanisms have been observed to differ between the estuarine channel and shallower subtidal flanks (Sommerfield and Wong, 2011), with salinity stratification primarily modulating the contribution of tidal pumping (McSweeney et al., 2016a). While the spatial variability of tidal sediment pumping has been clearly linked to stratification processes (Aristizábal and Chant, 2014; McSweeney et al., 2016a), the factors controlling the spatial variability of the residual sediment flux is less understood. Observations from moorings deployed in the channel show that the residual flux can drive sediment either up- or down-estuary, depending on both the location and the spring-neap conditions (Sommerfield and Wong, 2011; McSweeney et al., 2016a). A cross-channel line of seven moorings in the vicinity of the ETM further revealed a that lateral residual circulation is the primary driver of lateral sediment transport in Delaware and that there is a persistent lateral sediment flux towards the Delaware (DE) coastline along with an area of lateral convergence on the Delaware side of the channel slope and divergence on the New Jersey (NJ) side of the channel slope (McSweeney et al., 2016a). This observation indicates that there must be an along-channel convergence or residual return flow towards New Jersey either up- or down-estuary from the mooring line to maintain continuity. However, the location of such a convergence or lateral return flow is unknown and could have significant impacts on the total sediment transport.

This study uses a Regional Ocean Modeling System (ROMS) coupled hydrodynamic and sediment model to describe the 3-dimensional residual circulation and

consequent sediment transport in the Delaware Estuary. We focus on the spatial and temporal variability of the residual sediment flux, with the ultimate goal of better understanding how residual transport mechanisms impact sediment trapping within the estuary. By looking at a series of estuarine cross-sections, we highlight the variable spatial distribution of sediment transport and the relative importance of residual sediment fluxes in different regions of the estuary. We examine annual, seasonal, and spring-neap timescales to elucidate key factors that influence the residual sediment fluxes and determine how these contribute to sediment storage within the ETM.

3.3 The Delaware Estuary

The Delaware Estuary is a coastal plain estuary in the Mid-Atlantic Bight that extends approximately 215 km from the oceanic mouth to the head of the tides, near Trenton, NJ. The system is funnel-shaped and with asymmetric cross-channel bathymetry resulting from decades of channel dredging (Figure 3.1). Semi-diurnal tides are the predominant tidal forcing, and maximum tidal velocities on the order of 1.5 m s^{-1}. The main source of freshwater to the system is the Delaware River, which has an annual mean discharge of 340 m^3 s^{-1} (1950-2015), followed by the Schuylkill and Cristina tributaries, which annual contribute approximately 80 and 20 m^3 s^{-1} (Mansue and Commings, 1974). River discharge usually peaks in the spring months though storms throughout the year can also drive significant discharge events, which are evident in the historic discharge record at Trenton, NJ (Figure 3.2). 2011, the study period for this analysis, was a particularly wet year with several historic storm events.

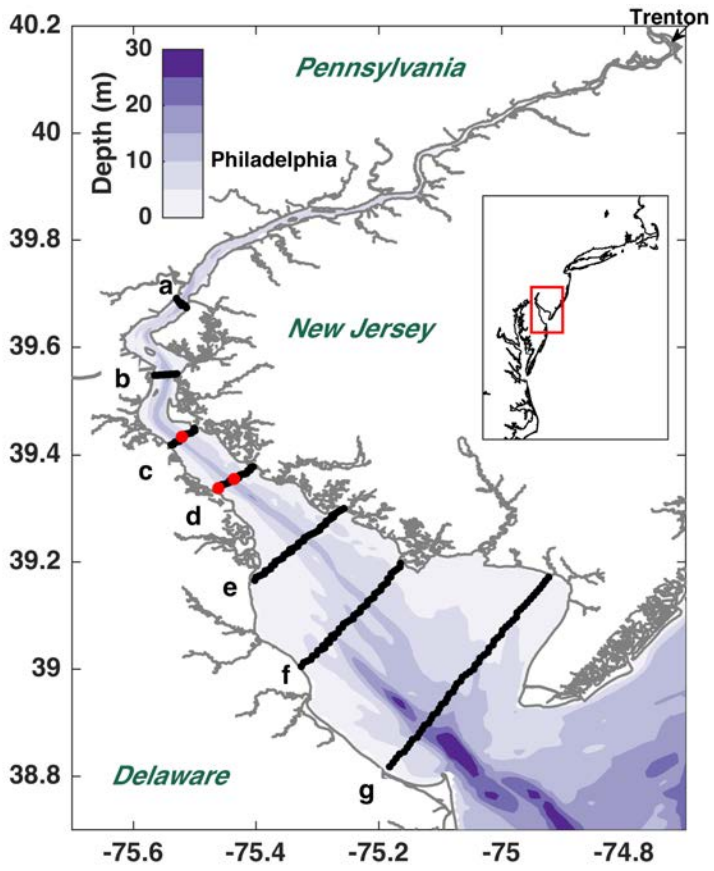

Figure 3.1 Map of the Delaware Estuary with depth contoured in purple and the cross-sections labeled a-g. The d cross section is in the same location as the McSweeney et al. (2016a) moorings. The red dots represent the locations shown in Figures 3.13, 3.14, and 3.15.

Suspended sediment delivery to the estuary is generally proportional to the fresh water discharge such that the greatest loadings are driven by freshest and storm events (Cook et al., 2007; Sommerfield and Wong, 2011). The Delaware and Schuylkill rivers deliver most of the new sediment, totaling roughly 1-2 $x10^{9}$ kg yr^{-1} (Mansue and Commings, 1974). In 2011, the sediment load at Trenton was approximately 7.8 x 10^{8} kg (McSweeney et al., 2016a). Suspended sediment concentrations are greatest in the ETM zone, which typically resides near the salt intrusion about 70-120 km up-estuary from the mouth. Sediment within in the ETM has been observed to be asymmetrically distributed

across-estuary, with the large deposition occurring over the Delaware side (McSweeney et al., 2016a).

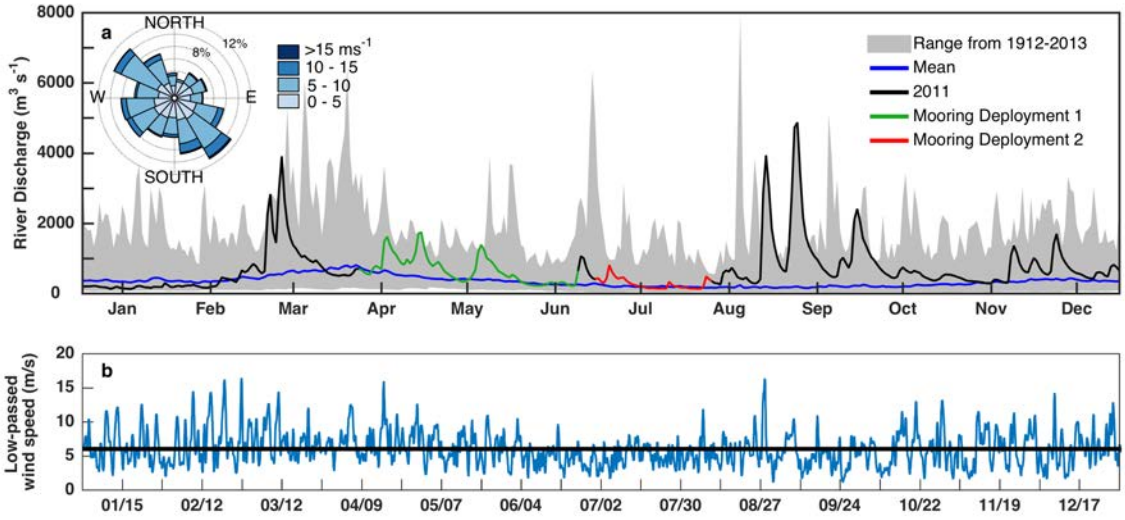

Figure 3.2 River and wind conditions during the 2011 model run. a) Mean daily discharge (m^3 s^{-1}) of the Delaware River at Trenton, 1912–2013 (blue line). Gray shaded region shows the range over the whole record. The solid black line is the 2011 discharge record and the green and red lines show the durations of mooring deployments discussed in (McSweeney et al., 2016a). The wind rose in the top left shows the direction wind is blowing towards colored by the wind speed for the year 2011. The dashed lines show the percent of time the wind is in a given direction over the entire year. b) The blue line is the low-pass filtered wind speed (m s^{-1}) at Ship John Shoal in the Delaware Estuary for the year 2011. The black line is the mean annual wind speed.

The subtidal currents and sea-level in the majority of the estuary are controlled by a combination of remote and local winds (Wong and Moses‐Hall, 1998). While remote winds are primarily responsible for the sea-level setup, local winds play a predominant role in modulating currents in the lower estuary. In 2011, the wind was most often oriented along the main axis of the estuary, as is typical of prevailing winds, and wind speeds were greatest in the winter besides a notable peak in August that coincided with Hurricane Irene (Figure 3.2).

Some studies have suggested that the Delaware Estuary is a well-mixed estuary (Beardsley and Boicourt, 1981; Garvine et al., 1992), but vertical stratification as strong as 10 psu have been observed in the estuary on both tidal, spring-neap, and longer timescales (Aristizábal and Chant, 2013; McSweeney et al., 2016a; McSweeney et al., 2016b). There is also a persistent lateral salinity gradient due to a laterally sheared exchange flow which causes the freshest water to hug the Delaware flank (Wong and Moses‐Hall, 1998; Aristizábal and Chant, 2013).

3.4 Numerical Model Description

3.4.1 Model Setup

In this analysis, we use a Regional Ocean Modeling System (ROMS) (Shchepetkin and McWilliams, 2005; Haidvogel et al., 2008) hydrodynamic model coupled with the Community Sediment Transport Modeling System (CSTMS) (Warner et al., 2008) to look spatiotemporal variability of residual circulation sediment transport in Delaware Estuary. The model uses a curvilinear 386 x 98 grid that has a horizontal resolution ranging from 2 km near the oceanic boundary to 200 m in the reach of the tidal river. There are 20 vertical terrain-following coordinate layers such that the vertical resolution ranges from 0.03 to 6.2 m, and the coordinate layers are stretched to increase resolution near the surface and bottom boundary layer. The tidal forcing includes the M_2, S_2, N_2, K_1, O_1, M_4, and M_6 tidal constituents, and there are six riverine point sources, including the Delaware, Schuylkill, Cristina, Rancocas, Cohansy, and Maurice rivers. We utilize the same grid as well as tidal, riverine, and atmospheric forcing files as Wang et al. (2012), so further details and hydrodynamic validation are not detailed here. The

model takes a little over a month to spin up, and then we run the simulation for the year 2011.

Since stratification in the channel and over the flanks is modulated by a combination of the lateral salinity gradient and the advection of the axial salinity gradient (Aristizábal and Chant, 2014) and given that stratification is key to sediment transport (McSweeney et al., 2016a), we validate the model further to ensure that it captures lateral salinity structure and main salinity dynamics. The modeled salinities were validated against data from seven cross-channel moorings that were deployed in the vicinity of the ETM April- July 2011. The details of the observations are described in Chapter 2 and McSweeney et al. (2016a). Figure 3.3 shows the Taylor diagram (Taylor, 2001) for model-data comparison of salinity, with the channel locations denoted by diamonds, the flank locations denoted by circles, and the two deployments denoted by different edge colors. Most of the flank data has a root-mean squared deviation (RMSD) less than 2 and a correlation coefficient greater then 0.8, indicating that the model is highly skilled at capturing the salinity over the shallower flanks. The channel data have an RMSD less than 3 and a correlation coefficient greater than 0.7, indicating good agreement between the model and observed salinities in the channel. We have fewer surface salinity timeseries in the channel, but validation against tidal surveys (not shown) indicates that the model is skilled at capturing surface salinities there as well. There is no clear difference between how the model agrees with data from the first and second deployments, which provides confidence that the model is behaving well through time.

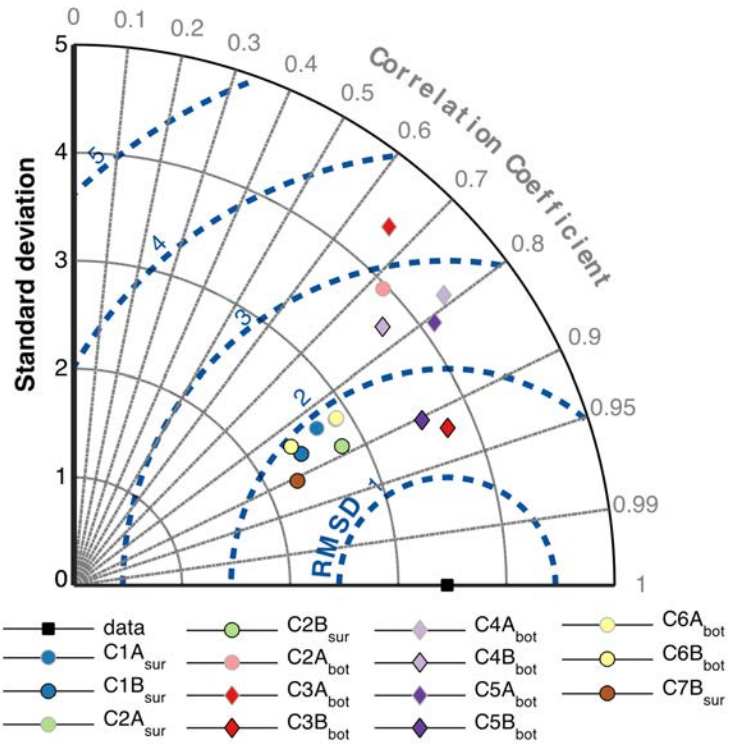

Figure 3.3 Taylor diagram for modeled salinity compared to observed salinity (Taylor, 2001). The black square shows the data itself to demonstrate the best possible model result. Circles represent flank locations and diamonds represent channel locations. The locations C1-C7 coincide with line d in Figure 3.1 and the specific lateral locations for C1-C7 are described in (McSweeney et al., 2016a). The A and B notations after the locations indicated the first or second mooring deployment, respectively.

3.4.2 Sediment Model

The sediment model includes three noncohesive sediment types, whose properties are detailed in Table 3.1. There two active bed layers, whose thickness changes in time through erosional and depositional processes described in Warner et al. (2008). The model is initialized with a uniform bed composed of 60% medium sand, 25% fine sand, and 5% silt which evolves during spin-up. Modeled sediment types are ultimately characterized by settling speeds, and we select settling speeds that mimic those of floc particles for the fine and medium sands. This model design permits us to better capture settling velocities realistic for the ETM without modeling flocculation.

During the simulation year, sediment is delivered with the Delaware River at the northern boundary of the grid. We estimate sediment delivery from river discharge by the following rating curve estimated at Trenton by Nash (1994):

$$Q_s = 0.01 \cdot Q_R^{1.8} \tag{3.1}$$

where Q_s is the sediment delivery (tons day^{-1}) and Q_R is the river discharge (m^3 s^{-1}). In contrast to the composition of the initial bed, the sediment delivered by the river is a mix of 20% medium sand, 75% fine sand, and 5% silt. It is known that flocculated matter plays an important role in Delaware's ETM, but the model does not include cohesive particles. Therefore, we assign different sediments compositions to the bed and riverine sediment so that sediment in the lower bay and the ETM have properties that are more representative of those observed in each region.

Sediment Class	**Sinking velocity (mm s-1)**	**Critical erosion stress (N m^{-2})**	**Critical deposition stress (N m^{-2})**	**Fraction in bed initialization**	**Fraction in riverine delivered**
Medium sand	40.0	0.5	0.5	60%	20%
Fine sand	3.0	0.1	0.1	25%	75%
Silt	1.0	0.05	0.05	15%	5%

Table 3.1 Modeled sediment properties.

3.4.3 Coordinate System and Sediment Flux Calculations

In order to distinguish axial and lateral sediment transport, we rotate the velocities to the axis of the along channel flows. First, the *u* and *v* components of the velocity are averaged to the center of each grid cell where salinity is calculated. Then, we take a month worth of hourly velocity data and find the rotation angle of the depth-averaged

maximum currents at each grid point. All velocity data is finally rotated according to these rotation angles. For all figures presented here, flows or fluxes up-estuary and towards NJ are positive.

The data are analyzed in two different frames of reference: looking at depth-dependent transport at different cross-section (Figure 3.1) or looking plan views of depth-averaged or depth integrated data. For the depth-dependent analysis, we isolate the residual velocities and sediment transport using hourly sediment, salinity, and rotated-velocity data that are low-pass filtered with a Lanczos filter (72-hour half window). For the depth-averaged and depth-integrated analyses, we calculate the residual velocities or transports using 12-hour data that is averaged over a specific timeframe (annual, seasonal, or spring-neap).

For the depth-dependent analysis, the residual sediment fluxes are calculated at a given horizontal location as follows:

$$Q_{s\ residual}(t,\sigma) = U_{residual}(t,\sigma) \cdot C_{residual}(t,\sigma) \tag{3.2}$$

where t is time, σ is the terrain-following vertical coordinate, $U_{residual}$ is the residual rotated velocity, $C_{residual}$ is the residual sediment concentration. In the depth-integrated analysis, the residual sediment fluxes are calculated at every horizontal grid point as such:

$$Q_{s\ residual}(t) = H\int_0^1 \left[U_{residual}(t,\sigma) \cdot C_{residual}(t,\sigma)\right]\partial\sigma \tag{3.3}$$

where H is depth. This decomposition method isolates the residual sediment flux from tidally-driven sediment transport such that the residual flux contains the influence of the river, estuarine exchange, and meteorologically-driven circulation (Geyer et al., 2001;

Chant et al., 2010; Sommerfield and Wong, 2011). For this analysis, we focus on residual fluxes rather than sediment transport by tidal pumping for two main reasons: 1) the mechanisms controlling tidal pumping and how they vary spatiotemporally have previously been described (McSweeney et al., 2016a), and 2) the residual transport contributes significantly to axial sediment fluxes and dominates the lateral sediment fluxes, providing motivation to understand what is driving spatiotemporal patterns of the underlying mechanisms.

3.4.4 Momentum Balance

To understand the mechanisms controlling lateral circulation in different regions of the estuary, we look at the across-estuary momentum balance at transects B, D, and F (Figure 3.1). In Cartesian coordinates, the balance is:

$$\underbrace{\frac{\partial v}{\partial t}}_{Acceleration} + \underbrace{u\frac{\partial v}{\partial x} + v\frac{\partial v}{\partial y}}_{Horizontal\ Advection} = \underbrace{-g\frac{\partial \eta}{\partial y} - \frac{g}{\rho_o}\frac{\partial \rho}{\partial y}}_{Pressure\ Gradient} + \underbrace{fu}_{Coriolis} + \underbrace{\frac{1}{\rho_o}\frac{\partial \tau}{\partial z}}_{Vertical\ Stress\ Divergence} \tag{3.4}$$

where v is the cross-channel velocity, u is the along-channel velocity, y is the cross-estuary direction, x is the along-channel direction, z is the vertical direction, t is time, g is the acceleration due to gravity, ρ is the density, f is the Coriolis parameter, and τ is the stress. The description of each term is noted in Equation 3.4.

For our timeseries analysis, we spatially average the momentum terms to reduce the influence of localized circulation and describe the circulation characteristic of the estuarine regions. We laterally- and axially average 15 grids, which are arranged in a 5 (lateral) x 3 (axial) formation centered at the thalweg of the given transect.

3.5 Results

3.5.1 Distribution of Sediment

Figure 3.4 shows a 7-day average sediment and salinity distribution for 31 May – 6 June 2011 and depicts an ETM spanning roughly 40 km along-estuary, extending from the 10 psu isohaline to the tidal-freshwater reach north of the salt-intrusion front. During low river flows, a substantial amount of sediment is resuspended tidally just northward of the salt intrusion front (Figure 3.4), but most of this sediment gets transported and trapped oceanward of the 0.5 psu isohaline during higher river discharge conditions (not shown). Transects along the thalweg illustrate that the ETM has a distinct along-estuary structure, where sediment is resuspended through the entire water column at the northern edge where there is no stratification and sediment is trapped in the lower portion of the water column by stratification in the southern half of the ETM (Figure 3.4b, c, d).

The lateral salinity is strained such that the DE coastline is freshest, the channel is saltiest, and the NJ coastline has a salinity value somewhere in between. This lateral salinity structure coincides with a cross-channel sediment distribution with sediment most concentrated on the DE flank (Figure 3.4a, e). A cross-section in the middle of the ETM (Figure 3.4**e**) shows that stratification over the DE flank limits sediment from being resuspended to the surface, whereas sediment is more well-mixed on the NJ flank where stratification is very weak. These lateral patterns are consistent with observations described by Aristizábal and Chant (2015) and McSweeney et al. (2016a).

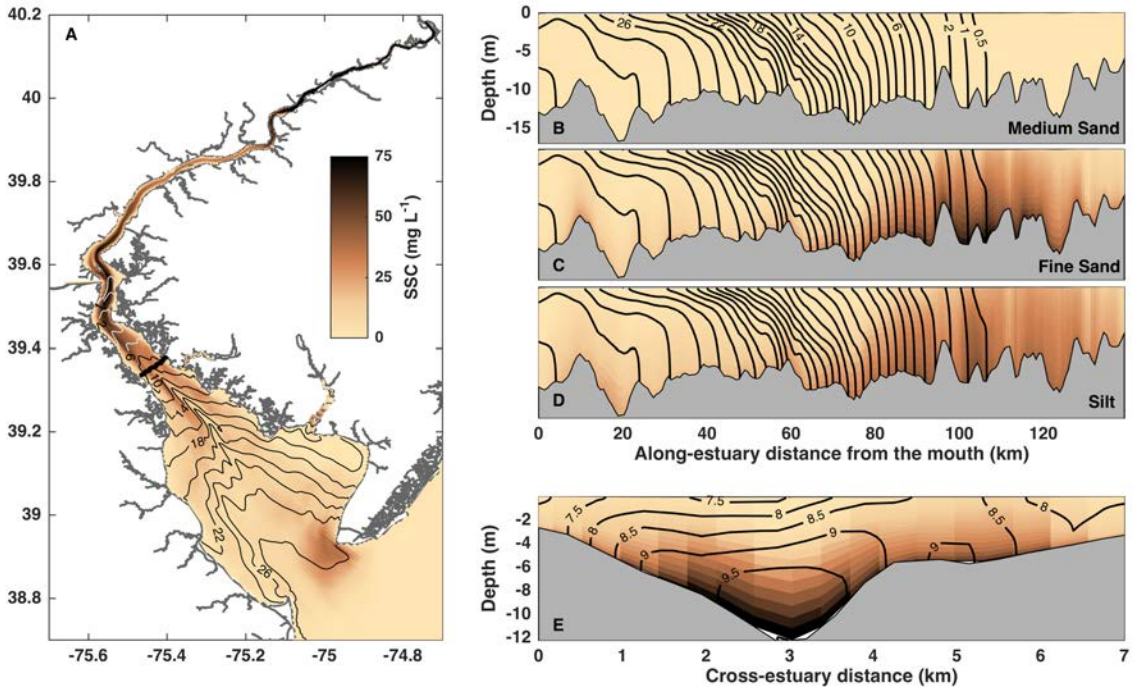

Figure 3.4 Sediment distributions from the 2011 model simulation. All panels show week-long averaged data for 31 May – 6 June from a 2011 year-long model simulation. All SSC data corresponds to the colorbar in panel A. A) plan view of the depth-averaged SSC (brown) contoured with salinity. B-C) Along-channel distributions of SSC for medium sand, fine sand, and silt sediment types (Table 3.1) respectively. The along-channel distance follows the thalweg. E) Across-channel distribution of SSC (sum of all sediment types).

Sediment types with unique settling velocities have different axial and lateral distributions. The fine sands (3 mm s^{-1}), which are most abundant in the model, clearly illustrate the axial structure of the ETM (Figure 3.4c) and mostly settle to the bed at slack tide in the southern portion of the ETM and on the shallow flanks (not shown). The silts (1 mm s^{-1}) are most easily resuspended and do not settle completely within a tidal cycle, resulting in an axial (Figure 3.4d) and lateral distribution (not shown) that is more vertically uniform. The medium sand (40 mm s^{-1}) has the highest critical erosion stress and is thus most difficult to resuspend. It also settles out of resuspension very quickly, so is less often advected by suspended transport.

3.5.2 The Relative Contribution of Residual Sediment Fluxes

To quantify the contribution of residual fluxes to total sediment transport, we plot the along-channel (Figure 3.5) and across-channel (Figure 3.6) instantaneous sediment transport (g m^{-1} s^{-1}) at locations across transect D (Figure 3.1) that correspond to the mooring locations described in McSweeney et al. (2016a). For the along-channel transport, the residual fluxes comprise roughly half of the total sediment transport (Figure 3.5) and are directed mostly down-estuary, through there are times of weak import, particularly in the channel. In contrast, the residual fluxes account for nearly all the lateral sediment transport and are directed mostly towards DE. Notably, the residual sediment fluxes in both the axial and lateral direction are much stronger on spring tide than neap. The spatiotemporal patterns of the tidal (total minus residual) and residual fluxes are generally consistent with those observed from the moorings (McSweeney et al., 2016a), which instills confidence that the model is capturing the important sediment dynamics. Though we only show timeseries at a handful of locations in Figures 3.5 and 3.6, the contribution of residual sediment fluxes described above holds true throughout the ETM, including locations where the direction of the fluxes are different.

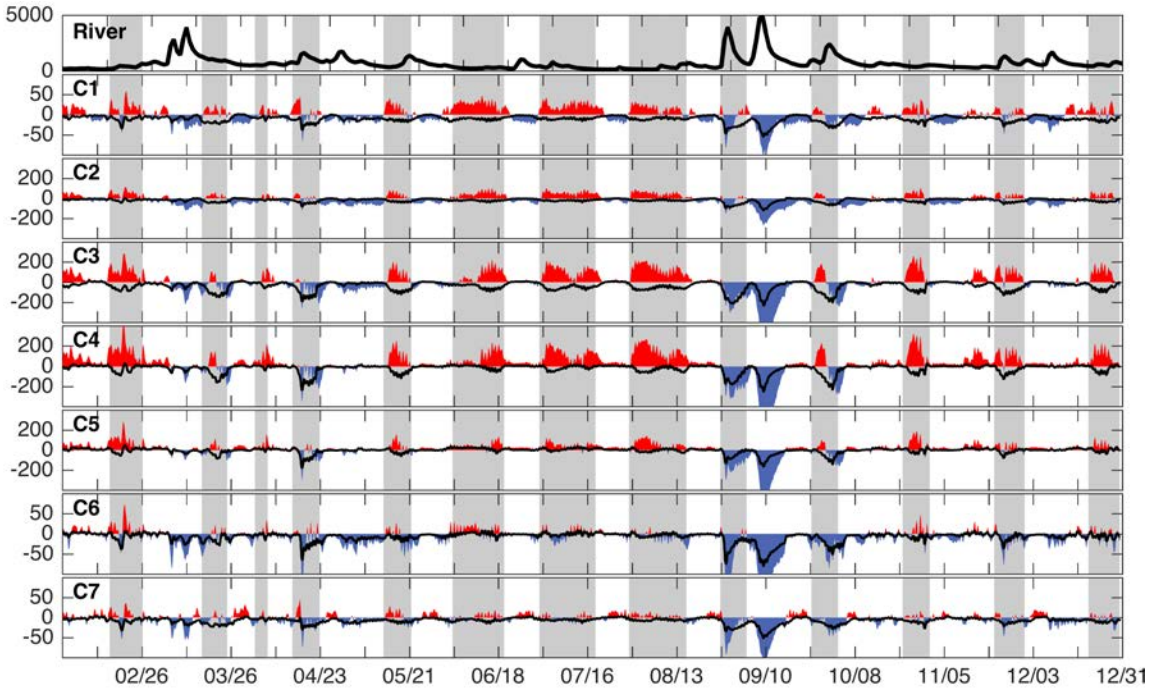

Figure 3.5 Time series of modeled instantaneous total along-channel sediment transport. (top) River discharge at Trenton ($m^3 s^{-1}$) in black (bottom) Time series of modeled instantaneous total along-channel sediment transport ($g m^{-1} s^{-1}$) at mooring locations C1–C7 from McSweeney et al. (2016a), which are located along the D transect line in Figure 3.1. Gray shading indicates spring tides, white indicates neap. Positive fluxes (red) signify import into the estuary, while negative fluxes (blue) indicate export. The black lines indicate the residual sediment fluxes.

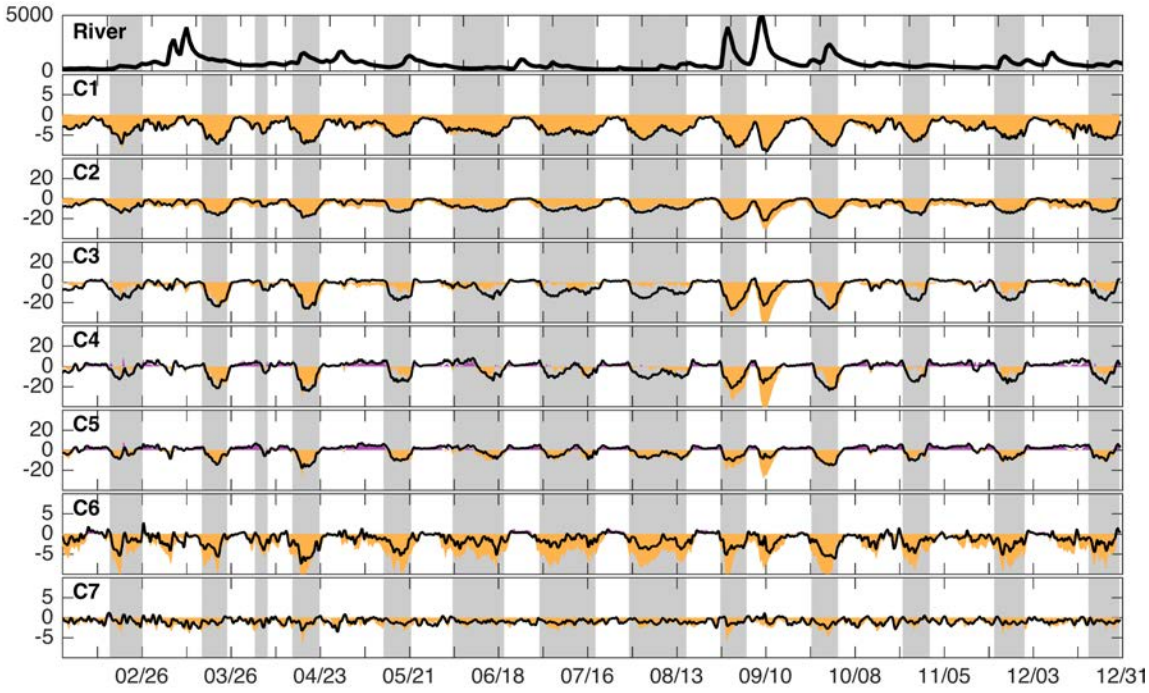

Figure 3.6 Time series of modeled instantaneous total across-channel sediment transport (g m^{-1} s^{-1}). Orange is towards DE and purple is towards NJ. All other figure details are identical to Figure 3.5.

3.5.3 Annual-mean Residual Circulation

To understand the 3-dimensionality of the annual-mean residual circulation, we look at the along-channel and across-channel flows at seven cross-sections up the estuary (Figure 3.7).

In the three northern transects, the mean residual velocity is oceanward at all depths, driven primarily by the river outflow (Figure 3.7a, b, c). Despite the similar along-estuary circulation, the cross-channel flows at these transects are quite different. At the northernmost section, flow is mostly towards NJ with a weak flow towards DE at the bottom (Figure 3.7aa). At transect B, the lateral flows are strongly sheared vertically such that there is a mean clockwise-circulation (Figure 3.7bb) with flow toward NJ at the surface and flow toward DE at the bottom. This lateral flow is consistent with secondary

circulation driven by flow curvature, which consists of flows in lower layer directed towards the inside of the curve bend and flows at the surface layer directed away the bend (Rozovskiĭ, 1957). At Transect C, the cross-channel flows are more spatially complex and there is a lateral shear acting on a 2-layered velocity structure which results in laterally divergent velocities (Figure 3.7cc).

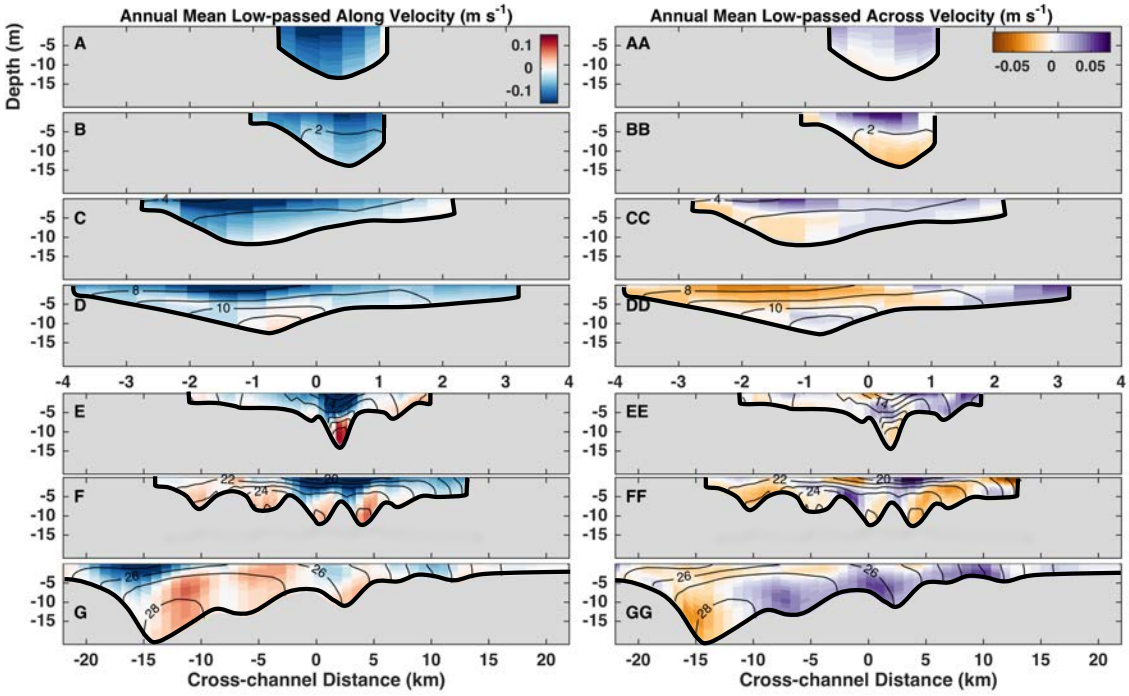

Figure 3.7 Lateral transects of mean-annual low-passed filtered velocities A-G) The mean annual low-passed filtered along-channel velocity (m s^{-1}) for cross-sections a-g (shown in Figure 3.1). Perspective is looking into the estuary, with Delaware (DE) on the left and New Jersey (NJ) on the right. Red is up-estuary, blue is down-estuary. Salinity is contoured in black. AA-GG) The corresponding mean annual low-passed filtered across-channel velocity (m s^{-1}) for each cross-section. Orange is towards DE, purple is towards NJ.

At transect D, the location of the mooring line described in Section 3.1, there is a strong down-estuary flow at the surface and a weaker up-estuary flow at the bottom (Figure 3.7d) due to both the influence of river discharge and the estuarine-exchange flow. Here, there is a lateral divergence over the NJ flank just eastward of the channel

slope and a counter-clockwise circulation in the main channel (Figure 3.7 dd). Further south, the estuarine exchange flow becomes stronger and the 2-layer axial circulation strengthens (Figure 3.7e). Notably, the estuary is much wider at transect E than transect D, and there is also a weak 2-layer exchange flow over the shallower flanks. The spatial variability of lateral flows is quite complex at transect E (Figure 3.7ee). On the DE flank there is a weak clockwise circulation, whereas on the NJ flank flows are generally towards NJ. In the channel, the transverse flows are 3-layered with flow towards DE at both the surface and bottom and flow towards NJ in the middle of the water column. Near the channel-shoal slope on the DE side there is a lateral converge at the surface and divergence at the bottom, which would drive downwelling.

In the lower estuary, the transverse bathymetry becomes more complex and there are multiple channels that impact the residual circulation. There is still mostly 2-layer flow with outflow at the surface and inflow at the bottom, but this pattern is spatially variable. At transect F, the estuarine exchange is quite weak over the DE flank and the inflow is stronger than the outflow such that the depth-averaged velocity would be up-estuary (Figure 3.7f). In the channel, the outflow dominates the inflow and there is a bathymetric high in the middle of the channel where there is no inflow at the bottom layer. Thus, the depth-averaged velocity in the channel would be down-estuary at transect F. On the shallow NJ flank, the flow is predominantly down-estuary, though the velocities are much weaker (Figure 3.7f). The lateral velocity structure at transect F also has complex spatial variability. There are four separate circulation cells alternating between clockwise and counter-clockwise.

At the southernmost cross-section, where the transverse bathymetry is asymmetric with the channel located westward of the center of the cross-section, the estuarine exchange is laterally- sheared such that the surface outflow is on the DE side of the channel and the bottom inflow is on the NJ side of the channel (Figure 3.7g). Over the shallower, NJ flank, the along-channel velocity patterns are spatially variable, with areas of weak 2-layer flows and a reach of weak down-estuary flows. There is a strong divergence in lateral flows in the main channel, and across-channel velocities are towards NJ over most of the NJ flank (Figure 3.7gg).

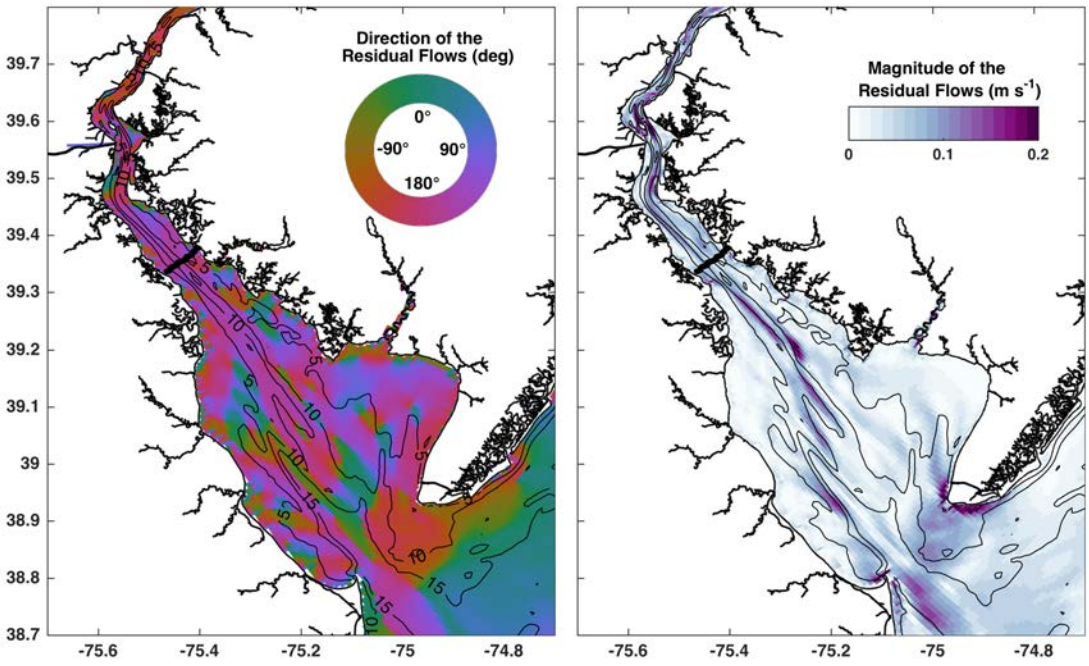

Figure 3.8 Map of the depth averaged residual flows. Left) the velocity direction (in degrees) Right) The velocity magnitudes (m s^{-1})

While Figure 3.7 illustrates that the mean depth-varying circulation is spatially variable, it also hints that the lateral variability in residual flows changes significantly along the main axis of the estuary. To gain a sense of the spatial variability of the residual circulation, we plot the direction and magnitude of the depth-averaged residual

(annual mean) velocities (Figure 3.8). There is a clear outflow in the main channel, but the residual circulation is spatially complex over the shallower flanks and in the lower estuary. There are locations, especially near the channel bends and over the flanks, where lateral flows are clearly important (Figure 3.8a, yellow and blue colors). In the region where the ETM typically resides, the along channel flows are consistently directed southeast approximately 150-160°. The spatial complexity of the residual circulation in the lower estuary clearly is connected to bathymetry, as is seen in the inflow along the eastern 10m isobath. Though lateral circulation appears to become increasingly important in the wider, lower bay, the magnitude of the residual flows is much weaker there (Figure 3.8b). The strongest residual velocities are focused in the channel, and the velocities over the flanks are stronger in the narrower reach of the estuary compared to those in the lower bay. Notably, velocities within the typical vicinity of the ETM are quite strong.

For comparison, Figure 3.9 shows the direction of the axial tidal flows. Note that the direction ranges from -90° to 90°, as opposed to -180° to 180°. In contrast to the residual flows, the tidal velocities appear less connected bathymetry features. However, the lateral flows (lighter colors in Figure 3.9) are similarly most important at the channel bends and in the lower estuary.

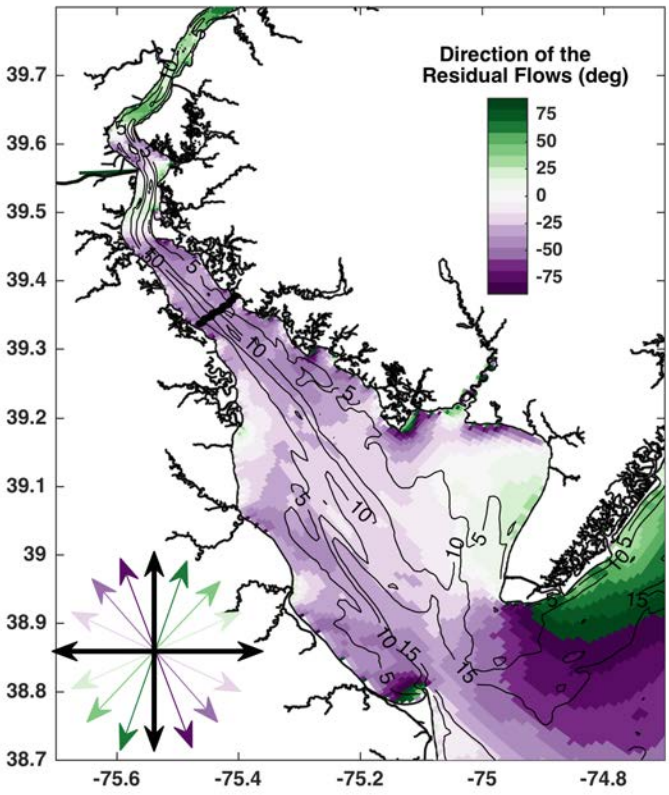

Figure 3.9 Map of the axial tidal flows. The direction (in degrees) of the axial tidal flows from 2 months of hourly model output of depth-averaged velocity. 0° is east, 90° is north, and -90° is south.

The spatial maps of the tidal and residual circulation indicate that the northern region of the ETM is influenced strongly by lateral flows due to channel curvature and strong velocities driven by narrowing of the estuary width. The central and lower regions of the ETM are dominated axial flows that are more consistently directed southeast, so lateral processes may contribute less to sediment transport there. The channel widening around transect E (Figure 3.1) likely plays an important role in the dynamics of southern edge of the ETM, as the cross-channel variability of the axial direction and flow magnitude become significant there

3.5.4 Annual-mean Residual Sediment Transport

To evaluate the annual-mean residual sediment transport, we similarly plot the depth-varying sediment transport at various cross-sections (Figure 3.10) and a plan-view of the depth-averaged sediment transport (Figure 3.11).

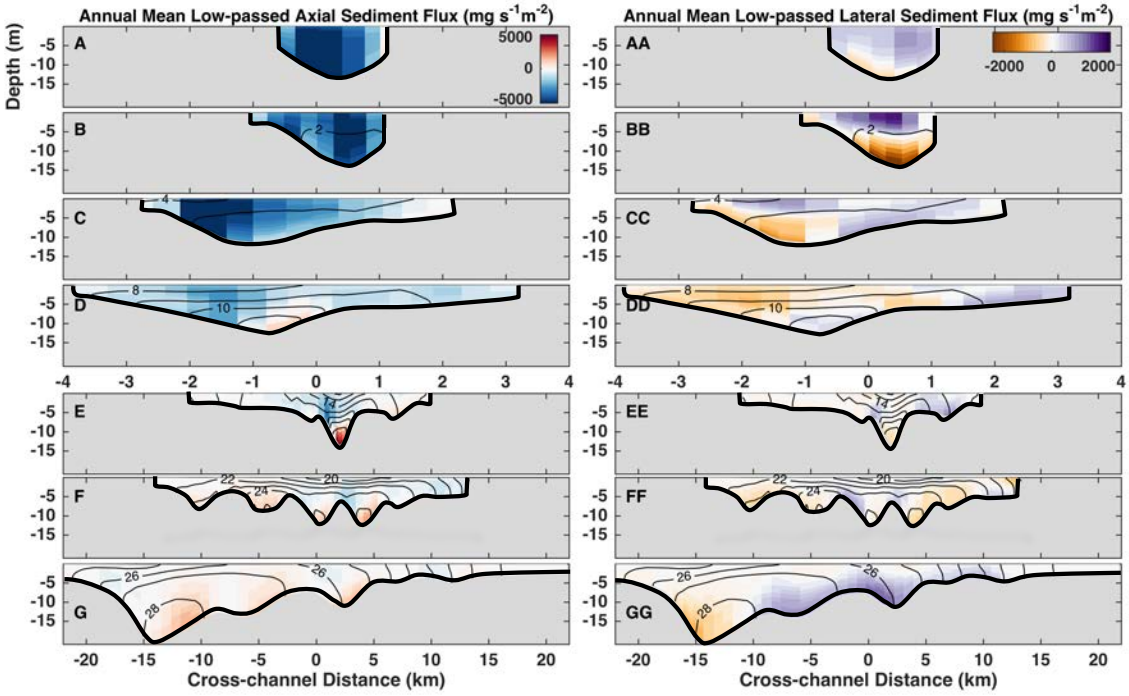

Figure 3.10 Lateral transects of mean-annual low-passed filtered sediment fluxes A-G) The mean annual low-passed filtered along-channel residual sediment fluxes (mg s^{-1} m^{-2}) for cross-sections a-g (shown in Figure 1). AA-GG) The corresponding mean annual low-passed filtered across-channel residual sediment fluxes (mg s^{-1} m^{-2}) for each cross-section. Same perspective and colors as Figure 3.7.

Looking at Figure 3.10, it is intuitive that the sediment transport spatial patterns are very similar to those of the residual velocities Figure 3.7, though unsurprisingly the fluxes are strongest in the lower water column. Along-estuary sediment fluxes are strongest between transects A and D (Figure 3.10a-g), where sediment concentration is greatest (Figure 3.10). The northern transects are dominated mostly by down-estuary transport (Figure 3.10a-d), while the southern transects are dominated weaker up-estuary

transport (Figure 3.10f,g). Transect E marks the transition between these two patterns, with a 2-layer structure of transport down-estuary in the surface and up-estuary at the bottom (Figure 3.10e). Along-estuary sediment fluxes are also notably stronger in the channel than over the flanks, especially in transects E and F. It is clear from these along-channel transport patterns that sediment is converging within the ETM on an annual timescale between transects D and F.

The cross-estuary residual sediment fluxes (Figure 3.10 aa-gg**)** also resemble the spatial patterns of the lateral mean velocities (Figure 3.7 aa-gg), but the sediment transports are not quite as spatially complex. In the two northernmost transects, there is a clockwise sediment transport pattern that becomes stronger down-estuary. In the center of the ETM, between transects C and D, there is a lateral sediment flux divergence along the axis of the estuary, with sediment on the western side being transported towards DE and sediment on eastern side being transported towards NJ. This lateral divergence is also prominent in in the lower estuary, although there is additional complexity with areas of lateral sediment convergence over bathymetric features.

A plan view of the depth-integrated along- and across- estuary sediment transports (Figure 3.11) provides a clearer picture of how the spatial variability of annual residual sediment fluxes ultimately impact the shape and sediment inventory of the ETM. Figure 3.11a highlights that there is a strong oceanward sediment flux that is centered in the channel and extends from the upper-estuary to mid-estuary, near the vicinity of the D transect. Lower in the estuary, just south of the D transect, there is an up-estuary sediment flux that is strongest in the main channel but also significant in the network of channels in the wider bay. The along-estuary convergence of sediment in the ETM is

obvious from this plan view, emphasizing that residual sediment transport mechanisms reinforce the trapping ability of the ETM.

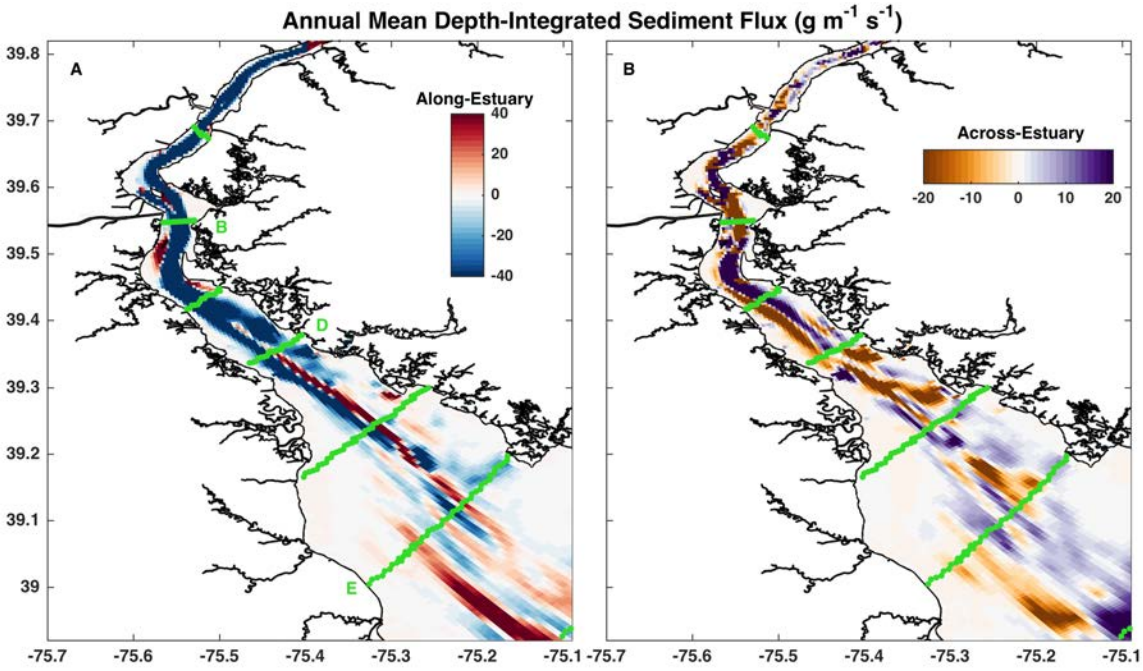

Figure 3.11 Map of the annual-mean depth-averaged along- and across- channel sediment transports (g s^{-1} m^{-1}) for the 2011 simulation. Red is up-estuary, blue is down-estuary. Orange is towards DE, purple is towards NJ.

Lateral sediment fluxes also contribute significantly to the trapping efficiency of the ETM, as is evidenced in the plan view of the depth-integrated cross-channel sediment transports (Figure 3.11b). There is a clear lateral sediment divergence that runs along the axis of the estuarine channel, which is consistent with that seen in Figure 3.7cc-gg. Furthermore, the lower estuary has several areas of additional convergence and divergence, which coincided with bathymetric lows.

In conjunction with the along-estuary sediment flux spatial patterns, the across-channel sediment fluxes rework sediment within the turbidity maximum. For example, sediment that originates in the channel near transects C may be transported down-estuary

and towards the DE coast until it reaches south of transect D, where it will move further south but towards NJ until it ultimately reaches the channel. In the channel, between D and E, it will then be transported up-estuary, where it may be further transported or trapped through deposition.

3.5.5 Seasonal Variability of Residual Sediment Transport

To evaluate how residual sediment transports vary over seasonal timescales, we identify high and low river discharge periods to isolate the impact of river discharge. Figure 3.12 shows the high (green) and low (red) discharge periods, along with the average river discharge for those times. The average discharge during the low flow period is roughly 1/3 of that during the high flow period and represents a typical summer in Delaware. The high flow period, in contrast, is representative of the spring season which includes freshet events.

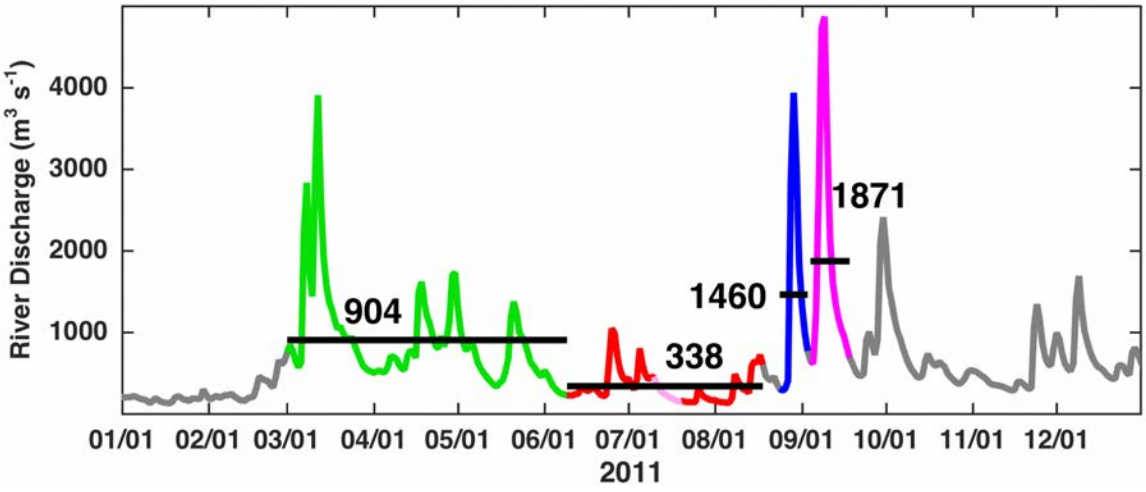

Figure 3.12 2011 river discharge at Trenton, NJ (m^3 s^{-1}). The high flow regime is colored green, the low flow is colored red, Hurricane Irene is colored blue, and Tropical Storm Lee is colored magenta. The black vertical lines indicate the average discharges for the two regimes and two storms. The light pink subsection of the low flow regime indicates the spring-neap cycle shown in Figures 3.15, 3.16 and 3.17.

The spatial patterns of the depth-integrated sediment fluxes averaged over the high-flow period (Figure 3.13) are quite similar to those for the annual-average (Figure 3.11). There is strong export throughout the upper-estuary, followed by import in the channel and export over the flanks in the mid- to lower-estuary. Though the spatial patterns are similar, the export magnitudes are greater than those seen in the annual-mean. Despite the strong riverine influence, there is still weak transport up-estuary in most of the wider, lower estuary which drives a convergence in the ETM.

During low river discharge, up-estuary sediment transport is much stronger in the channel, lower bay, and across regions of the shallower flanks (Figure 3.14a). Import in the channel extends landward to roughly transect C, which is much further than that seen in the high river discharge period. There is still significant sediment export in the channel in the upper estuary and over the flanks mid-estuary, but the magnitudes are significantly weaker than those during high river flows. While the along-channel sediment convergence by residual transport is evident during low flow conditions, it is clear that sediment will be reworked further north into the ETM during this time.

The across-channel sediment fluxes during both high (Figure 3.13b) and low (Figure 3.14b) river discharges are strikingly similar to the annual mean (Figure 3.11b). The lateral sediment fluxes have complex spatial variability in lower bay, while in the lower reach of the ETM it is predominantly towards DE, in the middle reach of the ETM it is divergent along the thalweg, and in the upper ETM it is predominantly towards NJ. This finding that lateral residual sediment fluxes are insensitive to river discharge indicates that the cross-estuary sediment transport mechanisms are seasonally-independent and influenced most strongly by local topography and tides.

Since river discharge has a consistent seasonal cycle of high flows during the spring, low flows during the summer, and moderate flows during the fall and winter (Figure 3.2), the sensitivity of residual sediment transport to river discharge implies that ETM sediment dynamics have a seasonal cycle. That is, during spring season, sediment within the ETM will be transported down-estuary by residual fluxes. Then, in the summer months, the ETM will migrate back up-estuary with residual sediment fluxes driven by the estuarine exchange flow. In the fall and winter months, the spatial patterns will likely resemble those of the annual mean, with sediment dynamics being controlled by a combination of riverine export and estuarine exchange import. Since the cross-estuary fluxes do not vary seasonally, the axial location of the ETM will determine whether sediment is reworked from the flanks back into the channel or exported toward the estuarine coastlines.

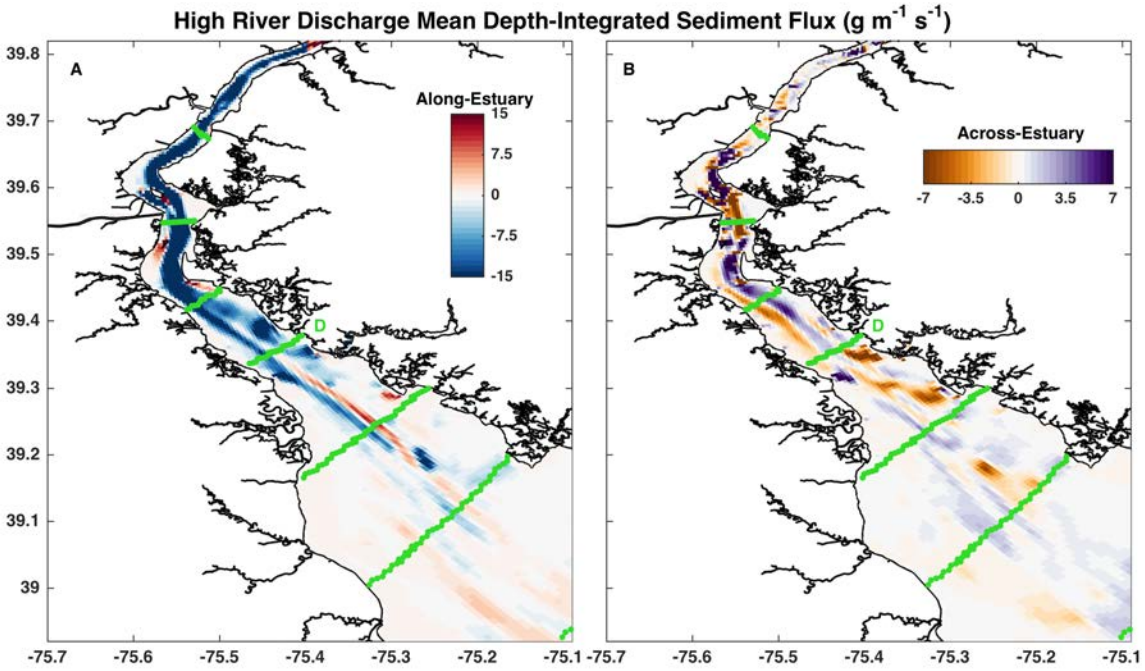

Figure 3.13 Map of the mean depth-averaged along- and across- channel sediment transports for the high river flow regime identified in Figure 3.12 (g s^{-1} m^{-1}). Red is up-estuary, blue is down-estuary. Orange is towards DE, purple is towards NJ. The green transects are the same shown in Figure 3.1.

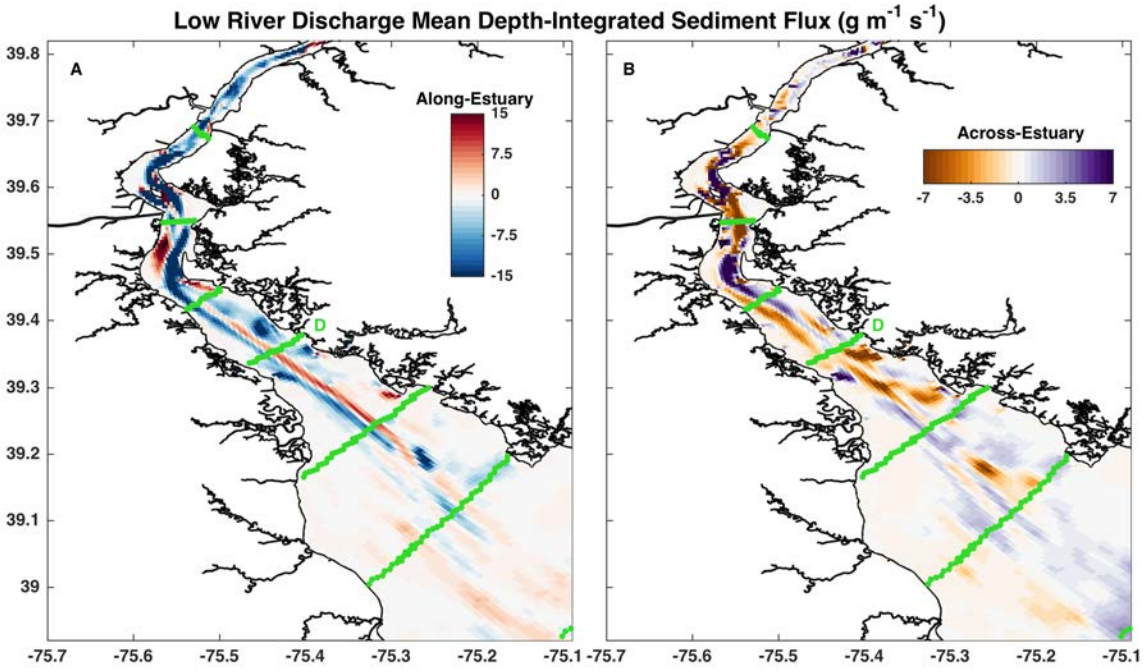

Figure 3.14 Map of the mean depth-averaged along- and across- channel sediment transports for the low river flow regime identified in Figure 3.12 (g s^{-1} m^{-1}). Figure layout is otherwise the same as Figure 3.13.

3.5.6 Spring-Neap Variability of Residual Sediment Transport

From the timeseries of along-channel and across channel sediment fluxes, it is clear that magnitude of residual sediment transport varies significantly on spring-neap timescales (Figures 3.5 and 3.6). To evaluate this variability, we look at the residual circulation and sediment transport over a spring-neap cycle at three different locations – in the channel at transect D, on the DE flank at transect D, and in the channel at transect C (Figure 3.1). We focus on a spring neap cycle in July when river discharge is low and fairly constant (Figure 3.12) in order to reduce variability driven by river discharge changes. The spring and neap tides are identified by demodulating the hourly velocity data for the entire year such that spring tides have a demodulated tidal velocity being greater than the annual mean and neap tides have a demodulated tidal amplitude less than the annual mean. While we focus our attention on spring-neap variability of residual processes (and not tidal pumping), we note that tidal timescales will impact spring neap variability.

In the channel at transect D, the transition from spring to neap tide is characterized by a weakening in the along-channel velocities and a shift from a lateral circulation that switches between clockwise and counter-clockwise on a tidal timescale to a lateral circulation that is predominantly counter-clockwise (Figure 3.15a-c). There is also a significant decrease in the amount of resuspended sediment during neap tide compared to spring (Figure 3.15d). The along-estuary sediment transport is significantly stronger during spring tide (Figure 3.15e,g), and the cumulative sediment flux is up-estuary (Figure 3.15g). In contrast, lateral sediment fluxes are strongest during the transition from spring to neap (Figure 3.15f,h). During peak spring tide (10-14 July) the

lateral fluxes reverse on a tidal timescale, resulting in a near-zero cumulative lateral sediment flux. This lateral reversal in the flow is consistent with that observed by (Aristizábal and Chant, 2014), and is driven by Coriolis and the across-channel pressure gradient. As the spring tide weakens and transitions to neap (14-18 July), the clockwise circulation on flood is stronger than the counter-clockwise circulation on ebb, which drives a net sediment flux towards DE. During neap tide (20-26 July), the lateral circulation is dominated by counter-clockwise velocities and sediment is transported predominantly towards NJ. Looking at a timeseries of the cumulative lateral sediment flux, it is clear that transport towards DE during the spring-neap transition dominates the weak transport toward NJ during neap (Figure 3.15h).

The spring-neap variability on the DE flank at transect D is quite different than that in the channel, demonstrating that there is important spatial variability on spring-neap timescales (Figure 3.16). The along-estuary velocities show relatively weak spring-neap variability, whereas the lateral circulation shifts from flowing mostly towards DE to becoming more tidally variable as the tide transitions from spring to neap (Figure 3.16a-c). Similar to the channel, sediment resuspension is greater during spring tide and weakens during neap (Figure 3.16d). Both axial and lateral sediment fluxes are greater on spring than neap, and the net transport is directed up-estuary and towards DE (Figure 3.16e-h). Notably the up-estuary transport on the flank is very spatially specific, as flank locations just slightly up- or down- estuary of this D location strongly export (Figure 3.14a).

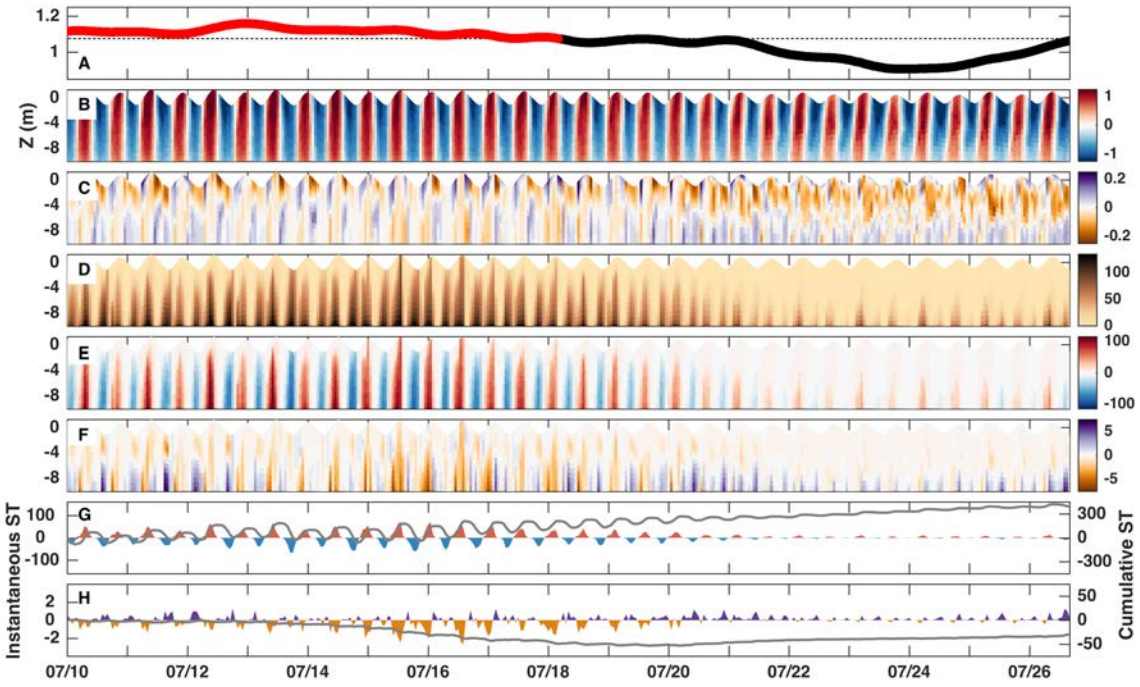

Figure 3.15 Timeseries at a location in the channel from cross-section D in Figure 3.1. A) Demodulated tidal amplitude. Black denotes neap tide, red denotes spring tide, and the dashed line marks the annual mean demodulated tidal amplitude. B) Along-channel velocities (m s^{-1}). C) Across-channel velocities (m s^{-1}). D) SSC (mg/L) E) Instantaneous along-channel sediment transport (mg m^{-2} s^{-1}). F) Instantaneous across-channel sediment transport (mg m^{-2} s^{-1}). G) Instantaneous (mg m^{-1} s^{-1}, colored, left y-axis) and cumulative (mg m^{-1}, gray, right y-axis) depth-averaged along-channel sediment transport. H) Instantaneous (mg m^{-1} s^{-1}), colored, left y-axis) and cumulative (mg m^{-1}, gray, right y-axis) depth-averaged across-channel sediment transport. For panels B, E, and G, red is up-estuary and blue is down-estuary; for panels C, F, and H, orange is towards Delaware and purple is towards New Jersey.

Further up-estuary, in the channel at transect C, the spring-neap variability of velocity and sediment transport is once again unique (Figure 3.17). Similar to the channel location at D, along-channel velocities noticeably weaken during neap tide and there is shift in the vertical structure of the cross-channel velocities (Figure 3.17a-c). Through the spring tide, lateral flows are quite weak and flow towards NJ during flood but are counter-clockwise during ebb; whereas during the neap tide, lateral flows are very strong and clockwise during flood and counter-clockwise during ebb (Figure 3.17c). It is

important to note that bottom cross-channel velocities are surprisingly stronger on neap than spring tide. Sediment resuspension is greatest during spring tide (Figure 3.16d), resulting in heightened along-estuary sediment transport that cumulatively pumps sediment up-estuary (Figure 3.17e,g). Since the weak near-bottom lateral velocities coincide with strong sediment resuspension during spring tide and the strong near-bottom lateral velocities coincide with weak sediment resuspension during neap tide, the magnitude of cross-channel sediment transport is fairly constant over a spring-neap cycle (Figure 3.17f,h). However, sediment transport is predominantly towards NJ during spring tide and fluctuates during neap, resulting in a net transport toward NJ (Figure 3.17h).

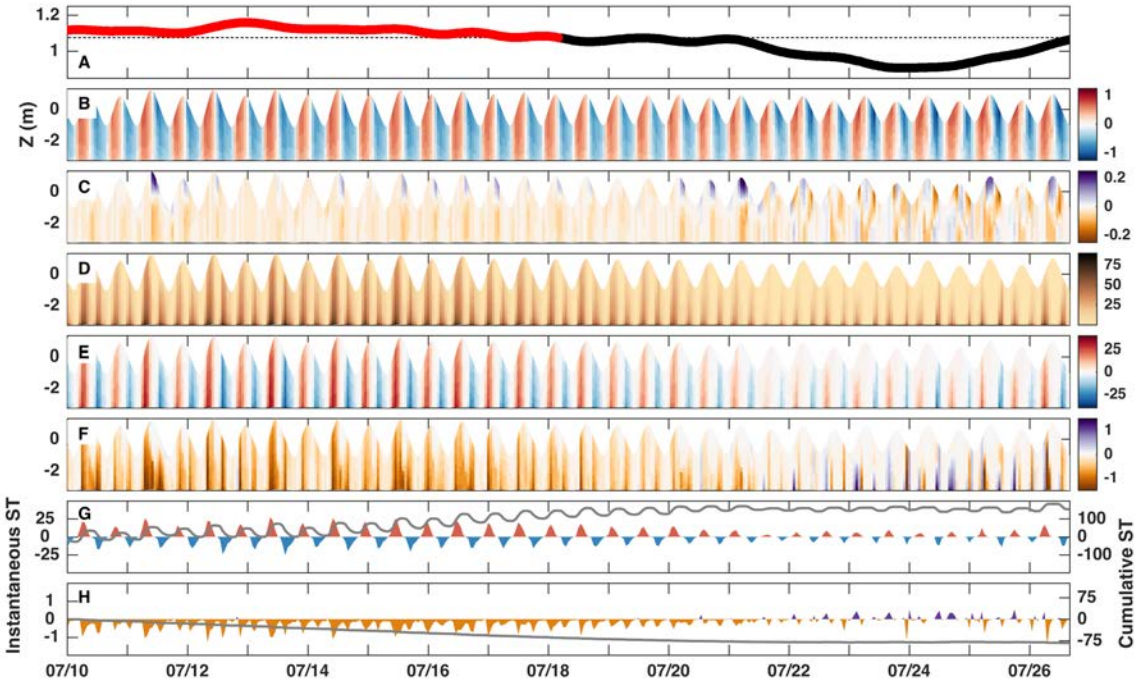

Figure 3.16 Timeseries at a location on the DE flank from cross-section D in Figure 3.1. All other aspects of the figure are the same as Figure 3.15.

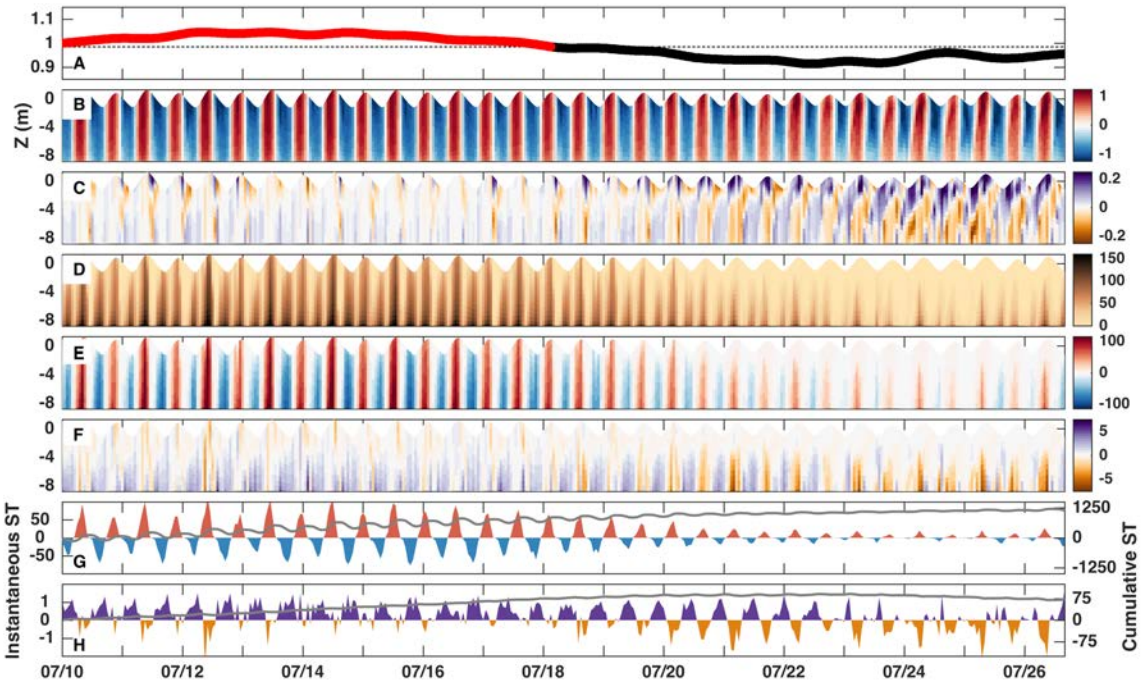

Figure 3.17 Timeseries at a location in the channel from cross-section C in Figure 3.1. All other aspects of the figure are the same as Figure 3.15.

While both axial and lateral sediment transport vary on spring-neap timescales, the variability appears to be spatially specific. To address how spring-neap variability impacts the spatial patterns of residual sediment fluxes in Delaware Estuary, we plot a map of the depth-integrated sediment fluxes averaged over a given spring (Figure 3.18) and neap tide (Figure 3.19). We select these specific tides during which river flow is both low and steady to minimize the influence of river discharge. Comparing Figures 3.18 and 3.19, it is clear that sediment import in the channel is much stronger during spring tides, but the sediment export on the flanks and in the upper ETM is of similar magnitude during spring and neap. Spatially, the two maps of along-channel transport are very similar. In contrast, the lateral sediment fluxes have greater spatial variability between spring and neap. During spring tide, the main stretch of the ETM (latitude 39.3-39.5) is characterized by a strong divergence along the thalweg, with fluxes towards DE

on the west flank and fluxes towards NJ in the channel (Figure 3.18c). During neap tide, divergent lateral fluxes there are much weaker and at the southernmost bend, where sediment fluxes are divergent during spring tide, the fluxes are directed strongly towards NJ (Figure 3.19c). Overall, the lateral sediment fluxes are stronger on spring tide than neap. We conclude that spring-neap variability has the greatest impact on lateral sediment fluxes, but that it also strongly modulates axial transport within the channel as observed by Sommerfield and Wong (2011).

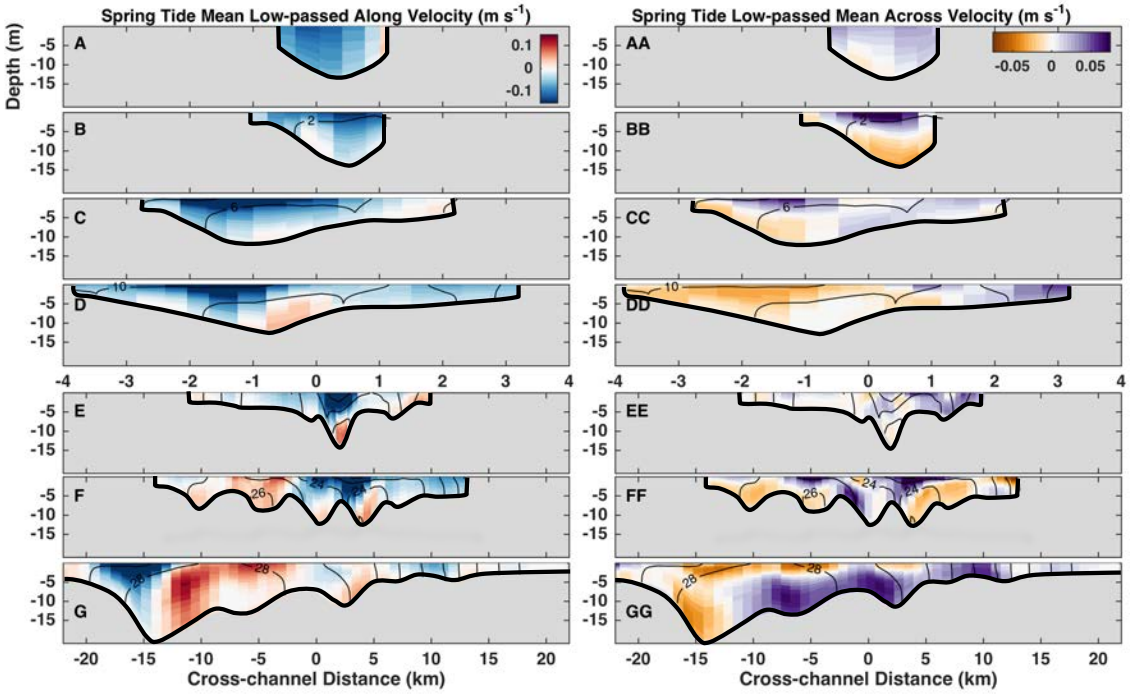

Figure 3.18 The spring tide mean low-pass filtered along-channel and across-channel velocities (m s^{-1}). Same figure design as Figure 3.7.

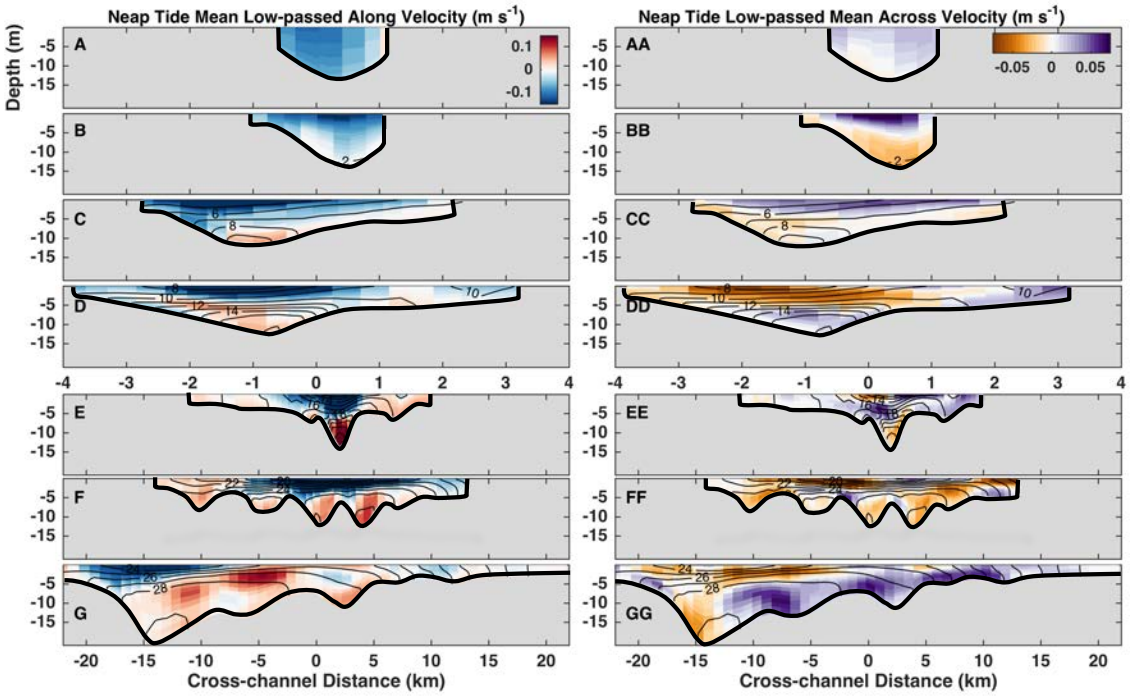

Figure 3.19 The neap tide mean low-pass filtered along-channel and across-channel velocities (m s^{-1}). Same figure design as Figure 3.7.

To assess why spring-variability plays such an important role in modulating lateral sediment transport, we plot the residual circulation at each transect location averaged over the same spring (Figure 3.20) and neap (Figure 3.21) tides. While the along-channel velocity structure is extremely similar for spring and neap, there are significant differences in the lateral flows. For example, at transect C there is a 2-cell circulation during spring tide with a clockwise cell on the DE side and a counter clockwise cell on the NJ side (Figure 3.20cc) but a 1-cell clockwise circulation during neap tide (Figure 3.21cc). Similarly, at transects D-G the secondary circulation becomes more pronounced during neap tides.

Notably, the stratification conditions vary significantly on spring-neap timescales and have a spatial structure that tends to coincide with that of the circulation features. During spring tides, the estuary is partially stratified and the secondary circulation is

quite weak, particularly in the narrower region of the estuary (transects A-E, Figure 3.20). The lateral flows tend to consistent of multiple cells such that there are many areas of convergence and divergence. In contrast, during the neap tide the estuary becomes strongly stratified within the salt intrusion and the secondary circulation becomes more pronounced (Figure 3.21). The lateral circulation becomes more vertically sheared, with a layering that follows the stratification.

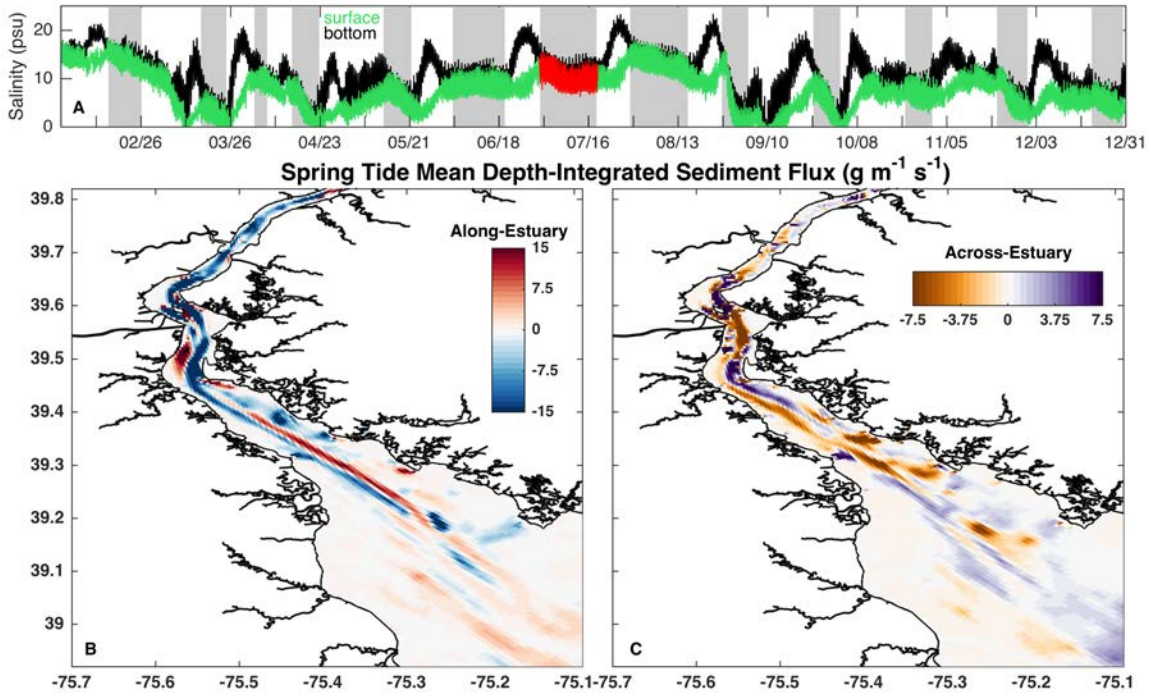

Figure 3.20 Map of the mean depth-averaged sediment transport during spring tide. A) Timeseries of the surface (green) and bottom (black) salinity at a location in the middle of the channel at Transect D (Figure 3.1). Spring tides are denoted by the gray shading. The red time highlights the spring tide that sediment fluxes are averaged over in the below panels. B-C) The mean depth-averaged along- (B) and across-(C) channel sediment transports (g s^{-1} m^{-1}) for the spring tide shown in red in A. Red is up-estuary, blue is down-estuary. Orange is towards DE, purple is towards NJ.

Despite secondary circulation being stronger during neap tides (Figure 3.21), spring tides generally drive stronger lateral sediment fluxes (Figure 3.18) due to the persistent spring-neap asymmetry in SSC resuspension (Figures 3.12-3.14). This finding

is consistent with observations that the along-channel tidal flows resuspend the majority of the sediment but that, due to the axial and lateral flows being out of quadrature, much of the SSC settles back to the bed before the lateral flows strengthen (McSweeney et al., 2016a). We conclude that the spatial variability of spring-neap residual flows is modulated primarily by asymmetries in the secondary circulation but that the magnitude of the spring-neap sediment flux variability is controlled resuspension asymmetries.

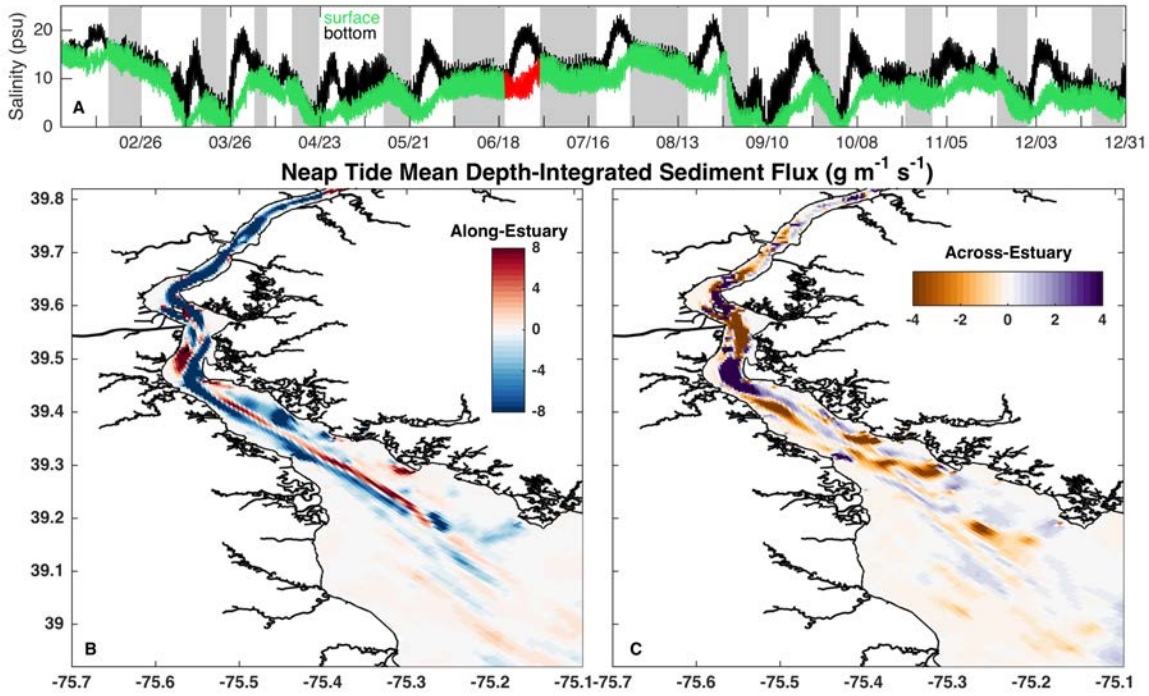

Figure 3.21 Map of the mean depth-averaged sediment transport during neap tide. All other aspects of the figure design are the same as Figure 3.20.

3.6 Discussion

3.6.1 Weighing the Importance of Different Timescales on Residual Sediment Fluxes

Estuarine sediment transport is known to vary on tidal (Scully and Friedrichs, 2007a; McSweeney et al., 2016a), spring-neap (Cook et al., 2007; Sommerfield and Wong, 2011), seasonal (Woodruff et al., 2001), annual (Ganju and Schoellhamer, 2006),

and longer timescales (Nash, 1994; Ralston and Geyer, 2009), but it is an ongoing challenge to understand the relative importance of these timescales and the combined impact they have on sediment dynamics within the ETM of a specific system. This analysis evaluates how residual sediment transport varies over spring-neap, seasonal, and annual timescales in the Delaware Estuary, with additional attention to spatial patterns of variability.

Along-estuary sediment transport is generally stronger on spring tides than neap and contributes significantly to cumulative transport over a spring-neap cycle. Though spring-neap variability in sediment transport varies spatially, the spatial patterns seem to be set up by longer timescales. For example, river discharge conditions clearly influence the location of the ETM and the spatial patterns of export and import such that the seasonal cycle controls the spatial transport pattern on an annual timescale. Though not the focus of this analysis, it is important to acknowledge that episodic events can drastically affect the sediment system due to their large river discharges and/or strong winds (Ralston et al., 2013) and therefore influence the annual residual sediment transport. Since 2011 contained several large storms, the annual sediment transport patterns discussed in this analysis are biased towards high river discharge conditions. A parallel analysis of a drier year would likely yield annual residual sediment flux patterns that are more consistent with those seen in the low river flow period.

As has been observed in the estuary (Aristizábal and Chant, 2013), the along- and across- channel velocities are out of quadrature (Figures 3.15-3.17), which cause the axial and lateral sediment fluxes to vary differently on spring-neap timescales. Since the width to depth ratio is linked to the phase difference between the axial and lateral flows such

that the velocities are further out of quadrature when the channel is narrower (Aristizábal and Chant, 2015), the spring–neap modulation of lateral sediment fluxes has a spatial component. Unlike the axial sediment fluxes, the magnitude of the lateral sediment fluxes varies spatially on a spring-neap timescale. The spring-neap variability is different in various regions of the estuary and is largely controlled by the spring-neap asymmetry in the lateral circulation, a finding consistent with observations of spring-neap variability in the James River (Valle‐Levinson et al., 2000; Huguenard et al., 2015). Looking at seasonal and annual timescales, one could conclude that the lateral circulation and sediment fluxes are time independent, but there is clear spring-neap modulation of both the lateral circulation and sediment fluxes. Thus, the lateral circulation and sediment transport vary on spring-neap timescales, but these variations are dominated by seasonal and annual variations when looking at longer timescales.

The spring-neap and seasonal patterns described in this analysis agree well with observations of sediment transport in the vicinity of the ETM (Sommerfield and Wong, 2011; McSweeney et al., 2016a) but provide further insight about how these timescales impact sediment fluxes on an annual scale and also how they are influenced by spatial patterns. Since observations are both temporally and spatially limited, a numerical model is necessary to provided broader context for sediment transport observations.

3.6.2 The 3-Dimensional Structure of Residual Circulation and the ETM

Many previous observational and modeling studies of the Delaware have hinted at the 3-dimensional complexity of the estuarine circulation, but this analysis advances our understanding of how the residual circulation driven by the river, estuarine exchange,

topography, and meteorological forcing varies spatially. We also address how this 3-dimensional circulation ultimately influences the structure of the ETM and the sediment distribution within the ETM.

In his analysis of the transverse variability in the lower Delaware Estuary, Wong (1994) described a strong inflow in the deep channel accompanied by weaker outflows over the shallower flanks. Our findings demonstrate that the spatial variability of the mean-flows is complex enough that the location of the cross section will significantly impact the observed transverse pattern. For example, in Figure 3.7g the along-estuary flows are fairly consistent with those observed and modeled by (Wong, 1994), but those in Figure 3.7e differ significantly. A map of the depth-averaged annual mean flows illustrates that the lateral variability of the along-estuary flows is strongly impacted by transverse bathymetry and varies significantly with along-estuary distance.

While Aristizábal and Chant (2014) describe a lateral circulation that shifts from a clockwise rotation to a counter-clockwise rotation over a tidal cycle, our findings demonstrate that this pattern holds true at specific times and locations but that the residual lateral circulation varies spatially and on spring-neap timescales. The model suggests a complex lateral circulation that sometimes consists of multiple cells, which resembles an analytical solution for the transverse velocities during flood that are driven by the semi-diurnal component of the cross-estuary density gradient (Huijts et al., 2011). The modeled lateral circulation is clearly influenced by local topography and thus becomes more complex in the lower estuary.

We also provide evidence that the exchange flow is laterally-sheared (Wong and Moses‐Hall, 1998; Aristizábal and Chant, 2013; McSweeney et al., 2016a) due to the

cross-estuary density gradient, generating what Valle-Levinson et al. (2003) described as "a 'sideways' estuarine circulation". This lateral straining of the flow drives a spatial pattern of residual sediment export on the DE flank and import within the channel. Coupled with a lateral sediment transport that is divergent along the thalweg in the middle reach of the ETM, the axial sediment fluxes cause the ETM itself to be laterally strained. That is, there is transport down-estuary and towards DE on the Delaware side of the channel and transport up-estuary and towards NJ in the channel. These model results explain the underlying factors controlling the residual circulation that ultimately cause lateral straining of the ETM and advection of the ETM structure up- and down-estuary in response to river discharge, which have both been observed but unexplained (McSweeney et al., 2016a). These findings provide a broader context to explain how a mooring transect can observe sediment export at all lateral locations during high river flow and then export over the flank and import in the channel during low flow (McSweeney et al., 2016a).

3.6.3 Across-Estuary Momentum Balance

To identify the important drivers of lateral circulation in the different regions of the estuary, we examine the across-channel momentum balance in the upper estuary, ETM region, and bay (Figure 3.22). Looking at the timeseries of the depth-averaged momentum terms and the vertical profiles of the spring tide, neap tide, and annual averages, it is clear the lateral circulation dynamics vary spatially. In the upper estuary (Figure 3.22a), the dominant time-varying balance is between the lateral pressure gradient and horizontal advection. From the vertical momentum profiles (Figure 3.22d,

g, j), it is clear that the pressure gradient is balanced by horizontal advection at the surface and by the vertical stress divergence in the lower layer. These momentum balances, along with the surface flow directed away from the bend and bottom flow directed toward the bend (Figure 3.7bb), are consistent with those associated with flow curvature (Geyer, 1993a; Chant, 2002). The barotropic pressure gradient is much more important than the baroclinic, likely due to the set up at the bend.

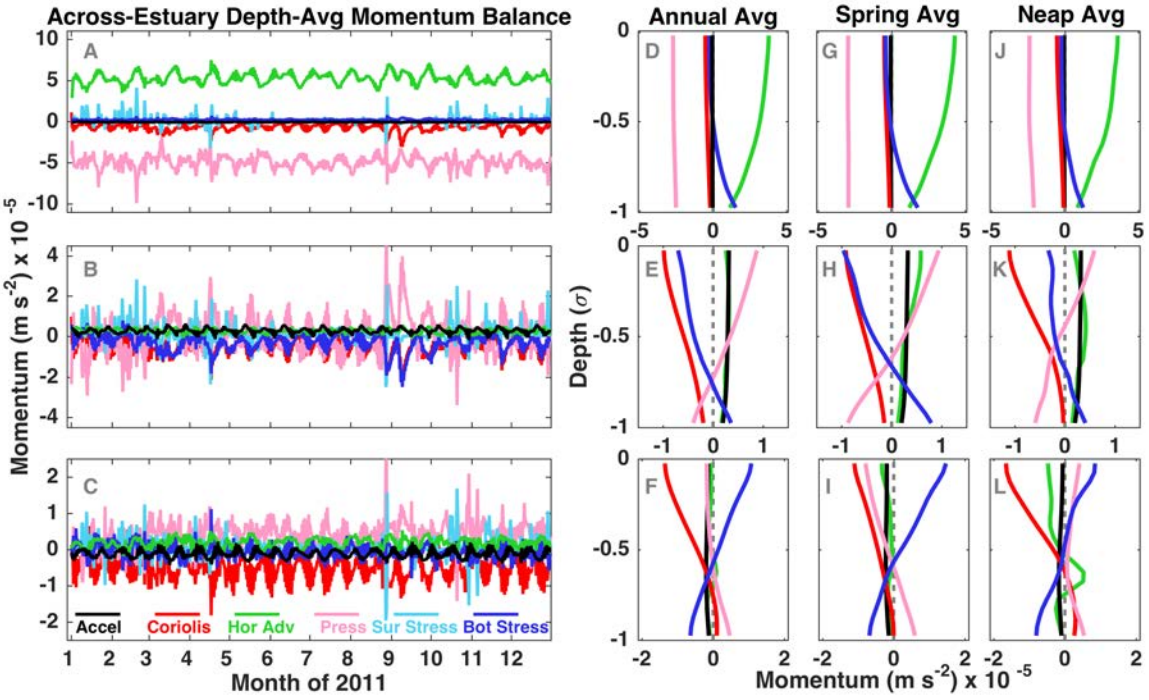

Figure 3.22 Across-estuary momentum balance for the 2011 model run. A-C) Timeseries of depth-averaged momentum terms (m s^{-2}) at locations up estuary (A, transect B in Figure 3.1), in the ETM (B, transect D), and in the lower estuary (C, transect F). The momentum balance includes acceleration (black), Coriolis (red), horizontal advection (green), the pressure gradient (pink), surface stress (light blue), and bottom stress (dark blue). D-L) Vertical profiles of the momentum terms averaged over 2011 for the upper estuary (D, G, J), ETM (E, H, K), and lower estuary (F, I, L). The colors are the same as A-C, with the exception of the blue, which describes the vertical stress divergence in D-L. D-F show the annual average, G-I show the terms averaged over a spring cycle, and J-L show the average over a neap cycle. All terms were obtained by averaging the values from a 5 x 3 grid centered on the thalweg location of each transect. Thus, the terms are laterally averaged across 5 grid points and axially averaged across 3 points to reduced the influence of localized circulation features.

The mechanisms driving lateral circulation are more complex in the ETM, and every term is significant in the momentum balance (Figure 3.22b, e, h, k). In general though, geostrophy and differential advection appear to be dominant. The pressure gradient, which is clearly both barotropic and baroclinc, is balanced nearly equally by Coriolis and the vertical stress divergence. Looking at the mean lateral circulation in that region (Figure 3.7dd), the flow towards DE is likely geostrophic whereas the clockwise circulation is probably driven by differential advection. When a lateral pressure gradient due to differential advection is balanced by the vertical stress divergence, a lateral circulation characterized by 2 cells that converge on flood and diverge on ebb tends to develop (Nunes and Simpson, 1985). However, due to tidal asymmetries in stratified estuaries, the lateral flows on flood tide can dominate those on ebb, resulting in a pattern of convergence in the thalweg (Lerczak and Geyer, 2004). In our case, both stratification and the geostrophic current likely mute the circulation features associated with differential advection. It is also worth noting that the acceleration and horizontal advection terms are significant and both drive momentum towards NJ.

In the lower estuary, the lateral circulation is mostly driven by Ekman transport (Figure 3.22c, f, i, l). From the vertical profiles, it is clear that the dominant balance is between the vertical stress divergence and Coriolis. However, from the timeseries of depth-averaged momentum, it is evident that the vertical stress divergence is also balanced by the baroclinic pressure gradient caused by differential advection. The lateral circulation driven by both of these mechanisms explains the multiple cells that are seen in Figure 3.7, which converge and diverge at different locations across the channel.

The timeseries of the momentum also sheds light on the impact storms can have on the estuarine lateral circulation. The increased wind speeds caused by Hurricane Irene are obvious in the surface stress peaks seen in late August at all 3 locations. The pressure gradient also peaks at that time due to the set-up from the winds, and the momentum balance is temporarily anomalous from the mean. However, it is clear that the estuary quickly returns to its normal state despite the magnitude of the event. Tropical Storm Lee, which had less wind but more rain, also perturbed the normal lateral circulation but had a weak influence in the upper estuary. Lee caused an increased pressure gradient due to the heavy rains, which therefore increased the geostrophic circulation and lateral flows due to differential advection.

Notably, the momentum balance varies on a spring-neap timescales, though the relative contributions of each term and the vertical profiles do not appear to be strongly influenced. This is surprising since both the estuarine stratification and lateral circulation have clear spring-neap variability. We conclude that the mechanisms driving lateral circulation do not change on spring-neap timescales, but that the magnitude of the lateral circulation is driven by the spring-neap variability in stratification.

3.6.4 Pathways of Sediment Reworking and Export

With this analysis, we ultimately aim to describe how residual sediment transport impacts the trapping within the ETM and identify key pathways of sediment reworking and export. In general, the residual circulation drives an along-estuary convergence of sediment but also laterally-strains the ETM. The seasonal river discharge cycle reinforces the trapping efficiency of the ETM by driving sediment down-estuary

(particularly over the DE flank) during high river flows and then, after sediment is driven back towards the channel by lateral circulation, back up-estuary in the channel during low river flows.

We identify three main pathways of sediment export: one driven by high river flow that is focused in the channel, a second that drives export to the DE coast on an annual timescale, and a third that exports sediment to the NJ coast on an annual timescale. The first is evident in Figure 3.12, where we see that there is strong sediment export along the DE slope of the channel. Just south of transect D, there is a cross-estuary transport driving sediment towards NJ until it hits an area of lateral-convergence that coincides with weak channel export. One can visualize that during a high river discharge pulse, sediment could be transported out of the ETM via this pathway, particularly during spring tides when stratification is reduced and more sediment is resuspended into high-velocity surface waters (Sommerfield and Wong, 2011). The second and third export pathways are evident in the annual-mean depth-integrated sediment transport map (Figure 3.11). There we see sediment export along the DE flank that eventually runs into an area (just south of transect D, where the estuary widens) of extremely weak transports up-estuary and towards DE. Through this export pathway, sediment could be transport slowly towards the fringing marsh, where it then becomes subjected to wave and marsh dynamics. Similarly, the third export pathway delivers sediment from the NJ flank to the shallower coastline just south of where the estuary widens (between D and E). There, an along channel export along the NJ flank bumps into an area dominated by lateral transport towards NJ, driving sediment towards the coastline.

To explore how these sediment transport pathways relate to the ultimate storage or export of sediment, we look at the change in bed thickness over an annual timescale to identify erosional and depositional hotspots with the ETM (Figure 3.23). There is incredible spatial variability in the bed change, but generally the DE side of the estuary is erosional and the NJ side is more depositional. There are two main hotspots of deposition that coincide with areas of channel curvature, where there is a tendency for up-estuary transport and lateral fluxes directed towards the inside of the bends. Erosion is dominant along the transitional slope between the DE flank and channel, where sediment export is often greatest.

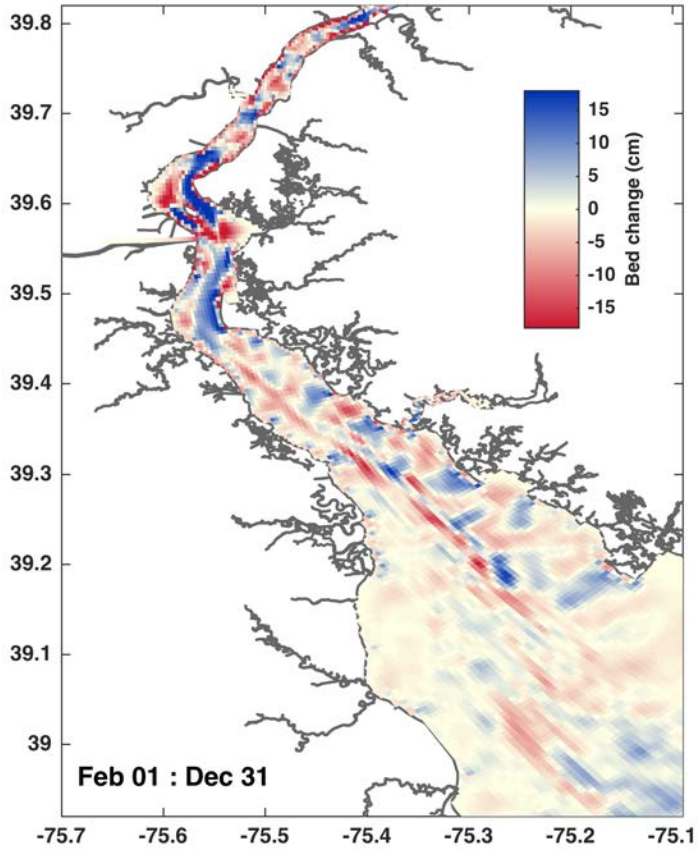

Figure 3.23 Map of the annual bed thickness change (from 1 February to 31 December 2011, cm). Positive values (blue) indicate deposition, negative values (red) indicate erosion.

Whereas the annual mean bed change is indicative of longer-term transport pathways, the bed change on shorter timescales is valuable to further access the role of discharge events and spring-neap variability. A comparison of the bed thickness change during high and low river discharge periods (Figure 3.24) illustrates that the spatial patterns of erosion and deposition are not sensitive to discharge. The magnitude of the bed change is predictably greater during higher river flows, but the processes controlling the spatial variability do not appear to vary. In contrast, there is significant spatial variability in erosion and deposition on spring-neap timescales (Figure 3.25). Most notably, the ETM region (in the vicinity of transect D) transitions from mostly depositional on spring to mostly erosional on neap. However, in both spring and neap, the spatial variability of erosion and deposition remains complex. The bed thickness changes are of similar magnitude on spring and neap in the upper estuary and ETM, but are much larger in the lower estuary during spring tide.

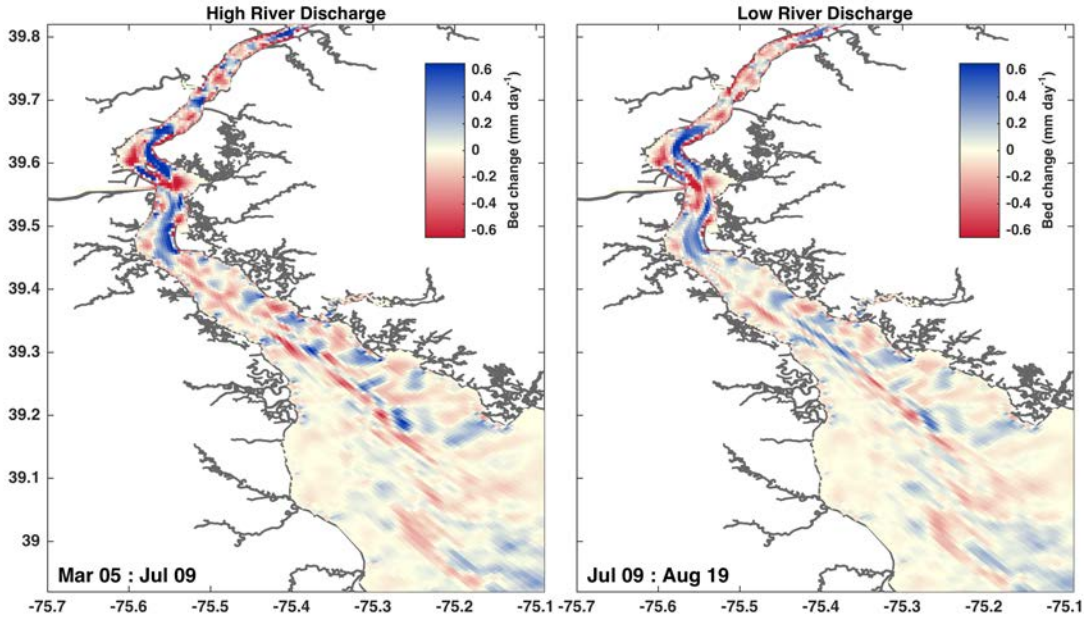

Figure 3.24 Map of the bed thickness change during high and low river discharges normalized by the day (mm day^{-1}). Positive values (blue) indicate deposition, negative values (red) indicate erosion.

The maps of erosion and deposition illustrate the spatial scales of important sediment transport pathways may be small yet have a large impact on the function of the sediment system as a whole. The estuary's ability to trap and store sediment is dependent on small-scale features that are challenging to identify through observations along. With our modeling approach this analysis identifies key pathways of reworking and export, providing key insight about the estuary's ability to trap, store, and export sediment over multiple timescales.

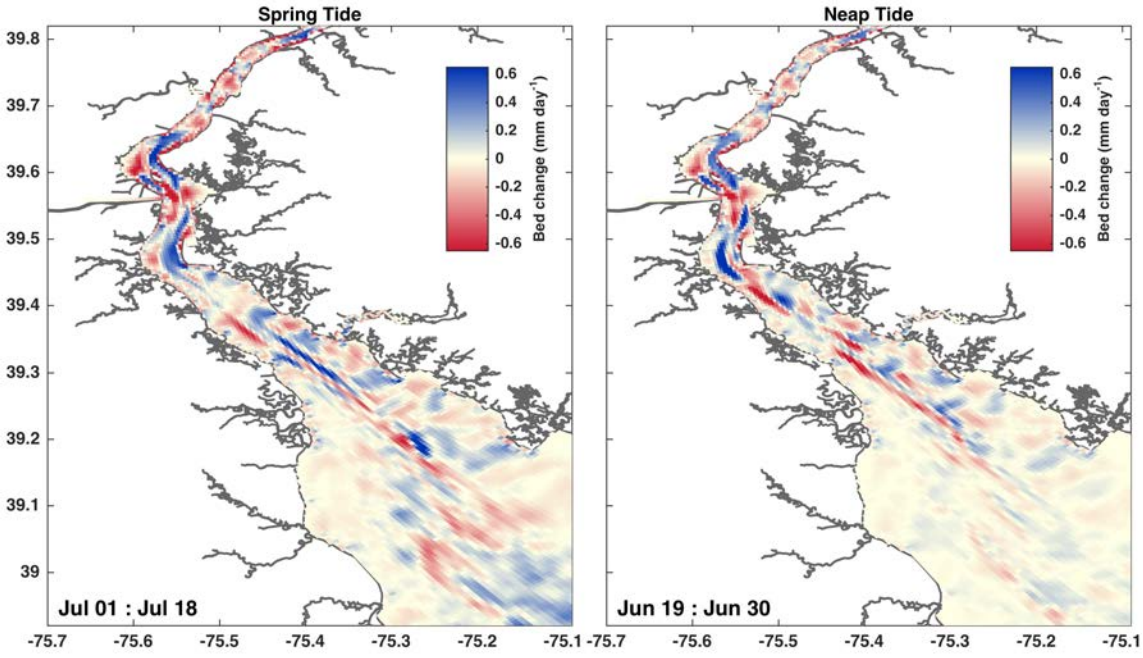

Figure 3.25 Map of the bed thickness change during spring and neap tides normalized by the day (mm day^{-1}). Positive values (blue) indicate deposition, negative values (red) indicate erosion.

To confirm that the estuary indeed traps sediment through convergence on an annual timescale, we examine the width-, time-, and depth- integrated annual along-channel sediment fluxes as a function of axial distance from the mouth for the 2011 simulation (Figure 3.26). In the upper estuary, particularly between transects A-D, there is a net sediment flux down-estuary, whereas in the lower estuary, between the mouth and

transect F, there is a weak flux up-estuary. Sediment converges between D and E, where the sediment flux is nearly zero. The bed thickness change and the average SSC values clarify that much of the sediment trapped through convergent processes remains in the water column rather than being deposited on the bed. We note that the estuary mouth is very dynamic, but that the effects remain local and do not strongly impact the sediment dynamics within the estuary itself. Despite high river flows during 2011, sediment does not get transported out of the estuary, indicating that reworking within the ETM is hugely important in the Delaware Estuary.

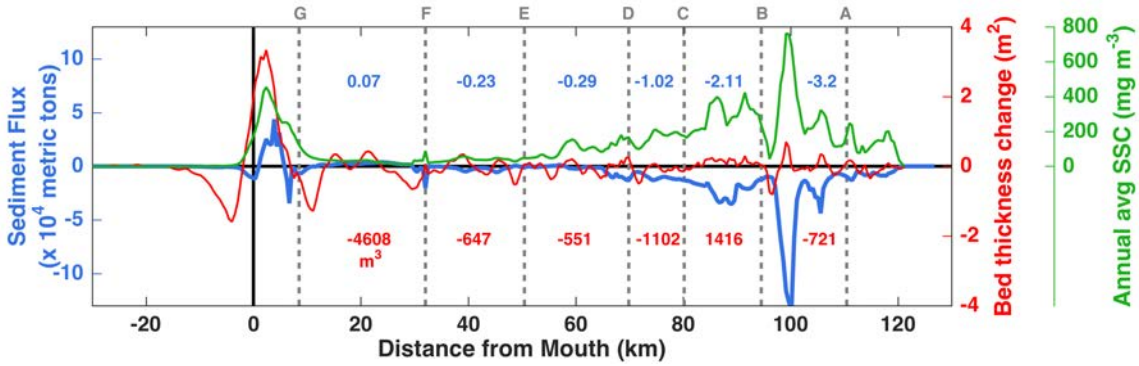

Figure 3.26 Integrated (in width, depth and time) annual along-channel sediment fluxes (x10^4 metric tons, blue) and bed thickness change (m^2, red) as well as the annual averaged , depth averaged SSC (mg m^{-3}, green) as a function of distance from the mouth (km). The cross-section locations (Figure 3.1) are noted in the gray dashed lines. The average of the fluxes (x10^4 metric tons) and the axially-integrated bed thickness change (m^3) between cross-sections are noted in blue and red respectively. Positive flux values indicate up-estuary transport, negative indicate down-estuary. Positive bed changes indicate deposition, negative indicate erosion.

3.7 Conclusions

This analysis uses a ROMS coupled hydrodynamic and sediment model to look at spatial patterns of residual circulation and sediment transport over spring-neap, seasonal, and annual timescales. We evaluate the relative importance of these different timescales

to sediment reworking and trapping within the ETM, paying particular attention to the role of spatial variability of sediment transport patterns. The model illustrates that along-estuary sediment transport is significantly modulated by river discharge, whereas the lateral fluxes are less seasonally variable and more influenced by spring-neap variability. Flow curvature drives the lateral circulation up-estuary, but in the ETM differential advection and geostrophy are more significant, and in the lower estuary lateral flows are Ekman driven. This analysis highlights the 3-dimensional nature of estuarine residual circulation and demonstrates that its spatial variability is complex enough that observations of lateral patterns are extremely sensitive to the location of the cross section. We conclude that the residual sediment transport on an annual timescale laterally strains the ETM and reinforces sediment reworking and trapping within the ETM, although there are also multiple export pathways that persist on seasonal and annual timescales which may facilitate sediment transport towards the estuarine coastlines.

3.8 Acknowledgements

We thank Eli Hunter, Maria Aristizábal, Alex Lopez, Dave Ralston, and Rocky Geyer for insightful conversations during the model setup and analysis. Data collection was funded through National Science Foundation grants OCE-0928567 and OCE-0825833. This material is also based upon work supported by the Institute of Marine and Coastal Sciences at Rutgers University and the National Science Foundation Graduate Research Fellowship under grant no. DGE-0937373. The model output from this study can be accessed by contacting Jacqueline McSweeney at jmcsween@marine.rutgers.edu.

Chapter 4: Sediment Impacts on Light-limited Productivity in Delaware Estuary

4.1 Abstract

The Delaware Estuary has a history of high anthropogenic nutrient loadings, but has been classified as a high-nutrient, low-growth system due to persistent light limitation caused by turbidity. While biogeochemical implications of light limitation in turbid estuaries have been well-studied, there has been minimal effort focused on the connectivity between hydrodynamics, sediment dynamics, and light-limitation. Our understanding of sediment dynamics in Delaware Estuary has advanced significantly in the last decade, and this study describes the impact of spatiotemporal variability of the estuarine turbidity maximum (ETM) on light-limited productivity.

This analysis uses data from eight along-estuary cruises from March, June, September, and December 2010 and 2011 to look at the impact of the turbidity maximum on production. Whereas the movement of the ETM is controlled primarily by river discharge, the structure of the ETM is modulated by stratification, which varies with both river discharge and spring-neap conditions. We observe that the ETM's location and structure control spatial patterns of light availability. To evaluate the relative contributions of river discharge and spring-neap variability to the location of phytoplankton blooms, we develop an idealized 2-dimensional Regional Ocean Modeling System (ROMS) numerical model. We conclude that high river flows and neap tides can drive stratification that is strong enough to prevent sediment from being resuspended into the surface layer, thus providing light conditions favorable for primary productivity. This study sheds light on the role of stratification in controlling sediment resuspension and promoting production, highlighting the potential limitations of biogeochemical models that neglect sediment processes.

4.2 Introduction

Light-limited production in estuaries has been a topic of much research in the last few decades. The Hudson Estuary (Stross and Sokol, 1989), San Francisco Bay (Cloern, 1991; May et al., 2003), the Chesapeake Estuary (Malone et al., 1988), and the Delaware Estuary (Pennock, 1985; Fisher et al., 1988) all demonstrate light-limitation. While the temporal and spatial patterns of light-limitation vary between systems, the underlying physics that control light-availability is a common issue for these turbid estuaries. That is, light is attenuated by sediment, chlorophyll, chromophoric dissolved organic matter (CDOM), and the water itself. The distribution of these light-absorbers is spatiotemporally variable, and light attenuation is therefore modulated by stratification, mixing, and circulation.

Suspended sediment has important implications in turbid estuaries with high nutrient loadings, where it may be the dominant factor limiting light available for primary production. Estuaries trap sediment from both riverine and coastal sources, and the estuarine turbidity maximum (ETM) zone, an area of elevated suspended sediment concentrations (SSC), is a region of active sediment trapping, resuspension, and deposition. Because sediment suspended in the surface waters attenuates light, low-light conditions can persist in high resuspension regimes (Biggs et al., 1983). Light limitation due to sediment ultimately depends on the frequency and duration of resuspension, particle size and density, and sediment concentration. The mechanisms that control sediment transport may vary spatially and temporally (McSweeney et al., 2016a), impacting the distribution of sediment within the estuary. Understanding the dynamics

that control sediment distribution and resuspension is fundamental to understanding how the optical environment is modified, especially within an estuary's ETM.

While others have acknowledged the importance of light limitation in turbid estuarine and coastal systems (Desmit et al., 2005; Arndt et al., 2007; De Swart et al., 2009) and investigated the role of hydrodynamics influencing estuarine sediment and light fields (Lawson et al., 2007; Devlin et al., 2008; Ganju et al., 2014), we present field observations and idealized model runs to explain these mechanisms in greater detail with the specific goal of relating spatiotemporal variations in stratification to patterns of primary production. This study focuses on the linkages between hydrodynamics, sediment dynamics and light-limitation in the Delaware Estuary, focusing on the importance of river discharge and spring-neap variability. The underlying mechanisms we discuss are broadly applicable to turbid estuarine systems and could provide insight into lingering questions about light-limitations.

Early modeling of light-availability and chlorophyll in the Delaware estuary highlights that suspended matter is the primary regulator of light-limitation and productivity under non-stratified conditions (Wofsy, 1983). However, stratification can persist in the Delaware on both tidal and longer timescales. For instance, stratification on a tidal timescale is modulated by a combination of along-channel and across-channel processes such that the flood can be either more or less stratified than the ebb tide (Aristizábal and Chant, 2014; McSweeney et al., 2016a). There is also spring-neap variability of stratification, with neap tides more stratified than spring tides (Aristizábal and Chant, 2014; McSweeney et al., 2016a). High river discharge during the spring season also favors persistently stratified conditions, which have been observed to increase

light availability and coincide with the initiation of phytoplankton blooms (Pennock, 1985). Spatiotemporal patterns in stratification always impact primary production through the critical depth average light availability, but this analysis emphasizes that there is also an indirect affect of stratification on light due to interactions between stratification and suspended sediment. Recent advances in our understanding of stratification mechanisms (Aristizábal and Chant, 2014) and sediment dynamics (McSweeney et al., 2016a) provide insight about the spatial and temporal patterns of stratification and how they may impact the optical environment by modulating sediment resuspension.

Despite an abundance of anthropogenic nutrient input, the Delaware Estuary has been described as a high nutrient, low growth environment because the attenuation of light by turbidity limits primary production and suppresses excessive blooms (Sharp et al., 1986; Pennock, 1987; Yoshiyama and Sharp, 2006). Production is maximal down-estuary of ETM, but levels of production are seasonally variable, with low values in the winter compared to the spring (Biggs et al., 1983). Observations indicate that the upper, turbid reach of the estuary is light-limited year-round, while the lower- and mid- estuary are not always light-limited March through September (Pennock and Sharp, 1994). The upper-estuary, in the known vicinity of the turbidity maxima, is geochemically filtered such that certain constituents are removed by flocculation reactions compared to the lower-estuary, which is more driven by biochemical filtration and removal by organismic processes (Biggs et al., 1983; Sharp et al., 1984). However, high flushing rates in the upper estuary during the spring cause the residence time to become shorter than the

chemical kinetics, decreasing the influence of geochemical filtration (Sharp et al., 1984) and the proportion of flocculated material in the turbidity maximum.

While there have been many regional studies focused on the variability of light-limitation and the feedbacks on productivity and biogeochemistry, the linkages between the sediment system itself and light availability is far less studied in the Delaware. Our understanding of sediment dynamics within the estuary has developed significantly in the last decade (Cook et al., 2007; Sommerfield and Wong, 2011; McSweeney et al., 2016a) and could provide important insight about spatiotemporal patterns of light limitation. Whereas previous studies have indicated that high nutrient loads in the Delaware do not elicit excessive blooms due the lack of summer stratification (Sharp et al., 2009), the present research emphasizes that the estuary has intermittent stratification that effectively limits sediment resuspension enough to permit primary production. This study focuses on the linkages between the sediment dynamics and optics with the ultimate goal of advancing our understanding of the primary controls on productivity, which is essential to improving our ability to model estuarine biogeochemical processes and would be useful when light data may be limited compared to sediment observations. We also discuss the seasonal variability of the location of turbidity maximum, drawing attention to the connection between the structure and location of the ETM and spatial patterns of phytoplankton biomass.

4.3 Regional Background

The Delaware Estuary is a coastal plain estuary in the mid-Atlantic region. It extends approximately 215 km from the mouth of the bay to the head of the tides near

Trenton, NJ (Figure 4.1). The Delaware River has a mean annual discharge of 330 $m^3 s^{-1}$ and is the main source of freshwater input to the estuary, followed by the Schuykill and Christina river tributaries, which contribute 77 and 19 $m^3 s^{-1}$ respectively. From the historic US Geological Survey discharge record, it is evident that discharge (Q_R) is typically maximal in March and minimal in September (Figure 4.2). Suspended-sediment delivery is proportional to the freshwater discharge. Thus, the highest sediment loadings to the system typically accompany the spring freshet. The sediment load in tons day^{-1}, Q_s, has been estimated as $Q_s \sim a \cdot Q_R^{\ b}$,where a is 0.01 (tons day^{-1} m^{-3} s) and b is 1.8 for the Delaware River at Trenton (Nash, 1994). The mean supply of all riverine sediment is estimated to be about 1-2 x 10^9 kg yr^{-1} (Mansue and Commings, 1974) and, using the rating relationship above, we estimate that the sediment loading at Trenton was 2.5x10^8 kg in 2010 and 7.3x10^8 kg in 2011. Notably, because 2011 was an anomalously wet year with several large storms, the sediment load in 2011 was nearly triple that of 2010.

The upper estuary bed is predominantly muddy compared to the sandy lower estuary (Delaware Bay), and mid-estuary tends to be a mixture of sand and mud (Weil, 1977; Biggs and Beasley, 1988; Sommerfield and Madsen, 2004). The New Jersey (NJ) side is dominated by sands from the continental shelf, whereas the Delaware (DE) side is a mix of fluvial and coastal plain sources (Neiheisel, 1973). Flocculation rates are maximal within the ETM region, and mudfloc sizes thus increase with proximity to the salt intrusion front; comparatively, the tidal river and lower bay tend to have lower SSC values and smaller particle aggregates (Gibbs et al., 1983).

The along-channel structure of Delaware's ETM is such that the landward leading edge is characterized by sediment mixed throughout the water column whereas the interior (or tail) has sediment that is constrained to lower in the water column by stratification (McSweeney et al., 2016a). In the lateral direction, sediment concentrations are consistently greater on the DE side of the estuary compared to the NJ side. Observations of sediment transport within the ETM region indicate that the ETM structure is laterally strained by tidal and subtidal processes that drive export on the DE flank and import within the channel (Sommerfield and Wong, 2011; McSweeney et al., 2016a).

The tidal freshwater Delaware River flows past the city of Philadelphia, which houses the fifth largest metropolitan population in the country (US Census 2010) and the Wilmington-Philadelphia port complex, one of the largest US shipping ports both historically and presently. Due to the level of urbanization, the estuary has extremely high nutrient loadings (Sharp et al., 2009). The chemical and biological response to high nutrient conditions has been monitored regularly since systematic sampling was initiated by Sharp et al. (1982), resulting in the finding that Delaware Estuary, unlike the neighboring Chesapeake, does not experience episodes of eutrophication.

The upper estuary bed is predominantly muddy compared to the sandy lower estuary (Delaware Bay), and mid-estuary tends to be a mixture of sand and mud (Weil, 1977; Biggs and Beasley, 1988; Sommerfield and Madsen, 2004). The New Jersey (NJ) side is dominated by sands from the continental shelf, whereas the Delaware (DE) side is a mix of fluvial and coastal plain sources (Neiheisel, 1973). Flocculation rates are maximal within the ETM region, and mudfloc sizes thus increase with proximity to the

salt intrusion front; comparatively, the tidal river and lower bay tend to have lower SSC values and smaller particle aggregates (Gibbs et al., 1983).

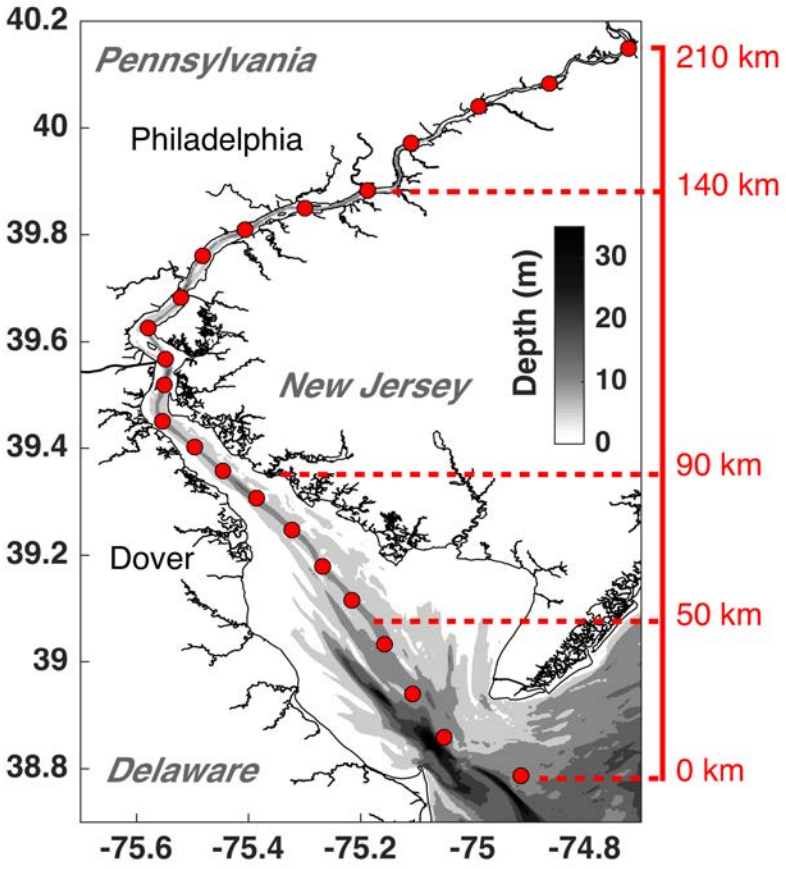

Figure 4.1 Map of the Delaware Estuary with grayscale depth and red dots indicating the 23 stations included in the along channel surveys. The along channel distance (km) is noted in red right of the figure. The approximate locations of ocean, lower-estuary, mid-estuary, upper-estuary, and tidal river are 0-14 km, 14-50 km, 50-90 km, 90-140 km, and 140-210 km respectively.

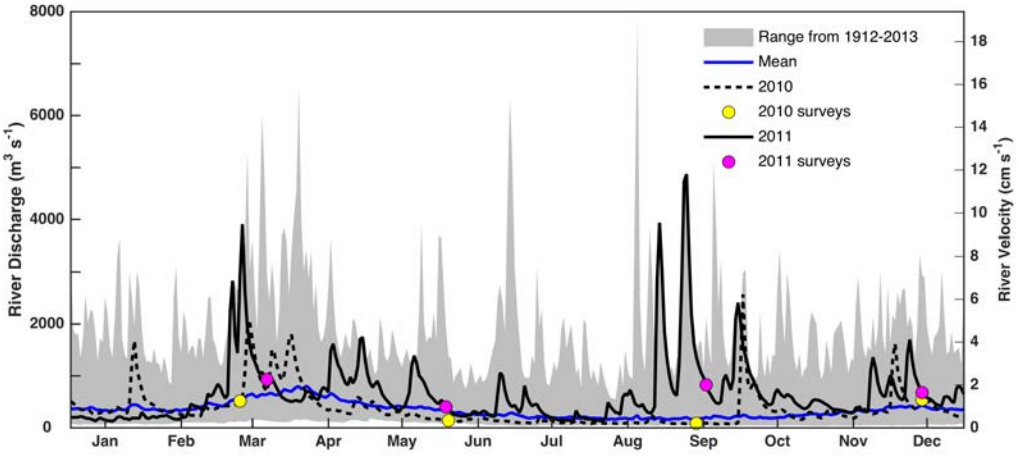

Figure 4.2 USGS River discharge data from 1912-2014 plotted by yearday. The grey shaded region is the range of historic data, the blue line is the historic mean, the dotted black line is the 2010 record, the solid black like in the 2011 record, and the yellow and purple dots indicate the discharge conditions during the 2010 and 2011 along-channel surveys respectively. The right y-axis is the river velocity (cm s^{-1}), which is the river discharge divided by the approximated cross-sectional area in the vicinity of the ETM.

4.4 Methods

4.4.1 Observations

Along-estuary surveys were conducted in March, June, September, and December of 2010 and 2011. Each survey took about 2 days, and there were 23 sampling stations along the thalweg from outside the mouth of the estuary to Trenton, NJ spanning the ocean, the lower-, mid-, and upper- estuary, and the tidal river (Figure 4.1). Vertical profiles were taken at each station with an instrument package that included an RBR CTD sensor to measure temperature and salinity, an optical backscatter (OBS) sensor, a Chelsea Aquatraka fluorometer, an Aanderra Optode oxygen sensor, and a Satlantic SUNA nitrate sensor. A shipboard flow-through fluorometer also collected fluorometry data at the surface.

Chlorophyll concentrations were estimated from the profiling fluorometer using the instrument's factory calibration. Due to instrument issues with the profiling fluorometer, we only had surface fluorometry data from the ship-mounted fluorometer in March 2010. To maintain consistency with the chlorophyll estimations, we calibrated the June 2010 profiling and boat-mounted fluorometers against each other and used this calibration to calibrate March 2010 boat-mounted fluorometer.

Water samples were collected with a pump one meter below the surface and 0.5 meters above the bed at each station. These samples were filtered to yield suspended sediment concentrations (SSC, mg/L). The OBS was then calibrated to SSC following the methods described by Kineke and Sternberg (1992).

Vertical profiles of downward-irradiance were collected with a Profiling Radiance Radiometer 600 (PRR) from Biospherical Instruments Inc. PRR cast depths were dependent on the irradiance penetration and typically ranged between 5 and 7 meters. PRR casts were only done during daylight, leading to limited spatial sampling during some cruises. Due to instrument issues, we were unable to collect optical data in September 2010 and June 2011.

The PRR collected data at six specific wavelengths, so Photosynthetically Active Radiation (PAR) was calculated by approximating the integral of the spectrum from 400 to 700 nm using the following equation:

$$PAR = \sum_{i=1}^{n} I_1 \Delta\lambda_1 + I_2 \Delta\lambda_2 + ... + I_n \Delta\lambda_n \approx \int_{400}^{700} I(\lambda) \partial x \qquad (1.1)$$

where I is the light intensity of a given wavelength λ. The depth-varying light attenuation can be described by

$$\alpha(z) = \frac{\partial I}{\partial z} \cdot \frac{1}{I_{avg}} \tag{1.2}$$

where α is the diffuse absorption coefficient, z is the depth, and I_{avg} is the average irradiance at a given depth. For a constant α, the solution for Equation 4.2 is an exponential profile.

The diffuse absorption coefficient can be further decomposed to isolate the attenuating factors important in estuarine systems:

$$\alpha = \alpha_{sw} + \alpha_{chl}[Chl] + \alpha_{CDOM}[CDOM] + \alpha_{sed}[SSC] \tag{1.3}$$

where α_{sw} is the absorption due to seawater, α_{chl}, α_{CDOM}, and α_{sed} are the specific absorption coefficients for chlorophyll, CDOM and sediment respectively, and [*Chl*], [*CDOM*], and [*SSC*] are the concentrations of chlorophyll, CDOM, and suspended sediment (Gallegos et al., 2005). Because CDOM has been found to minimally impact light attenuation in the turbid salinity reach of the Delaware estuary (Sharp et al., 2009), we neglect the $\alpha_{CDOM}[CDOM]$ term in Equation 4.3 to focus of the dynamics within the turbidity maximum. We estimate the α_{sw}, α_{chl}, and α_{sed} by iteratively minimizing the root mean squared error (RMSE) between the observed irradiance profiles and the modeled irradiance solution, which relies on measurements of chlorophyll and SSC along with initial best estimates for α_{sw}, α_{chl}, and α_{sed}. The best fit coefficients are listed in Table 1, along with values from literature for comparison.

Notably, our estimate for α_{sw} is high compared to values in the literature due to the inclusion of data from the tidal fresh reach. Whereas Sharp et al. (2009) concluded that CDOM was a relatively unimportant attenuator in the salty regions of the estuary, they found it to be more important in the fresh tidal reach. Our analysis focuses on the

dynamics within the ETM rather than those in the fresh reach, but we include the data from all the transects in our estimation of the attenuation coefficients to best estimate irradiance throughout the entire estuary. The exclusion of α_{CDOM} likely increases α_{sw}, though we are unable to confirm this since we do not have measurements of CDOM. Despite the inflation of the α_{sw} estimate, our results of the ETM dynamics are robust because turbidity is the dominant control on light availability in the ETM. Results in the tidal fresh reach, in contrast, entail more uncertainty due to the influence of CDOM but are not the focus of this analysis.

The estimated sediment and seawater coefficients were then used as inputs in the idealized ROMS model described in Section 4.4.2. We selected to use the chlorophyll-specific attenuation from Pennock (1985) to parameterize the ROMS model rather than use our estimate, which was based on fluorescence calibrations rather than direct observations, because ROMS models chlorophyll biomass, not fluorescence.

Parameter	Symbol	Value	Reference
Incoming shortwave radiation below the sea surface (W m^{-2})	I_0	**340**	
Fraction of shortwave radiation that is photosynthetically active	*par*	**0.43**	
attenuation coefficients for estuarine water (m^{-1})	α_{sw}	0.095 **0.40**	Pennock (1985) this study
attenuation coefficients for chlorophyll (m^{-1}/(mg L^{-1}))	α_{chl}	**0.020** 0.050	Pennock (1985) this study
attenuation coefficients for sediment (m^{-1}/(mg L^{-1}))	α_{sed}	0.075 0.0589 **0.065**	Pennock (1985) (Arndt et al., 2007) this study

Table 4.1 Optical properties estimated from data (as described in Section 4.4.1) compared to those in the literature. The values that are bolded were used to parameterize the idealized ROMS model.

4.4.2 Idealized Model

We use a Regional Ocean Modeling System (ROMS) hydrodynamic model (Haidvogel et al., 2000; Shchepetkin and McWilliams, 2005) coupled with a biogeochemical model (Fennel et al., 2006) and the Community Sediment Transport Modeling System (CSTMS) sediment model (Warner et al., 2008) to investigate the impacts of the sediment on light-limited production in an idealized estuary. The model is quasi-2D, focusing on the along-estuary direction without the influence of changing estuary width, lateral bathymetry, or lateral circulation. Since the spatial sediment and chlorophyll patterns in Delaware have been observed to have a strong along-channel signal, we use the 2-dimensional framework to focus on the axial processes. The turbidity maximum indeed has important 3-dimensional structure (McSweeney et al., 2016a), and, as discussed further in Section 4.5.4, the importance of lateral processes is something to explore in future work.

The model estuary is 150 km long (200 grid points) and 500 m wide (7 grid points) with a depth that linearly decreases from 15 m at the mouth to 4 m at the head. There are 20 vertical terrain-following coordinate layers stretched to weight resolution toward the surface and bottom boundary layers. The sides and head of the estuary are closed boundaries, and the mouth is an open boundary with combined radiation and nudging conditions (Marchesiello et al., 2001) for nitrate, oxygen and temperature, and radiation conditions (Orlanski, 1976) for all other tracers. Chapman/Flather conditions are used for sea level and depth-average velocity in conjunction with imposed tidal

variability in the form of a simple harmonic progressive wave. A gradient condition is used for 3D momentum. We use the generic length scale (GLS) $\kappa - \varepsilon$ vertical turbulence closure scheme (Umlauf and Burchard, 2003), and a constant quadratic bottom drag coefficient. The model includes M_2 tides and Coriolis, but no wind. Each model run has a constant river discharge, which will be discussed further in the Section 4.5.3. The model is initialized with a constant horizontal nitrate and salinity gradient that is vertically well-mixed, and then nitrate, oxygen, and sediment are all delivered with a point source riverine input at the head. The delivery of nitrate, oxygen, and sediment is constant and independent of river discharge, so that the river discharge model simulations compare varying physical controls alone. Because there is an excess of nutrients, nitrate supply is not a limiting factor for production in any of the discussed cases.

The sediment model includes three noncohesive sediment classes and there are two active bed layers that vary in thickness depending on the erosion and deposition, as described by Warner et al. (2008). In the Delaware, suspended-sediment characteristics in the vicinity of the ETM vary from those in the lower bay. Because production is most often light-limited in the region of the turbidity maximum, the model is designed to represent the sediment dynamics in this region. Consequently, we initialize the model with a Gaussian distribution of sediment that is centered in the expected vicinity of the ETM and prescribed sediment characteristics typically of those observed in the Delaware's ETM (described in Table 4.2).

Settling Velocity ($mm\ s^{-1}$)	**Erosion Rate ($kg\ m^{-2}\ s^{-1}$)**	**Critical Stress for Erosion ($N\ m^{-2}$)**	**Critical Stress for Deposition ($N\ m^{-2}$)**
3.0	5×10^{-4}	0.05	0.10

8.0	5×10^{-4}	0.05	0.10
10.0	5×10^{-4}	0.05	0.10

Table 4.2 Model sediment properties.

In the biogeochemical model described by Fennel et al. (2006), phytoplankton growth depends on the available PAR, which is controlled by light attenuation from the seawater and chlorophyll. To include the absorption by sediment, we modify the equation for the absorption of photosynthetically available radiation (*I*) as follows:

$$I = I(z) = I_o \cdot par \cdot \exp\left\{-\left(\alpha_{sw} + \alpha_{chl}\int_z^0 Chl(\sigma)\partial\sigma + \alpha_{sed}\int_z^0 SSC(\sigma)\partial\sigma\right)\cdot z\right\} \quad (1.4)$$

where I_0 is the incoming light in the surface water, *par* is the fraction of light that is photosynthetically available, $Chl(\sigma)$ and $SSC(\sigma)$ are the chlorophyll and suspended sediment concentrations at sigma layer σ, and *z* is depth. The constants α_{sw} and α_{sed} are iteratively estimated from an nonlinear fit to the solution of Equation 4.3 (as described in Section 4.4.1), and we use α_{chl} from Pennock (1985) (Table 4.1). We ran two sets of runs with different α_{sed} values to compare our estimations with those by Pennock (1985), though as discussed in Section 4.5.5 we only show results from the models with α_{sed} = 0.065 $m^{-1}/(mg\ L^{-1})$ because we determined the model to be insensitive to the two different values.

In order to address the role of spring-neap variability, we also run a case of constant river discharge (75 $m^3\ s^{-1}$) that has M2 and S2 tidal constituents of equal magnitude. The spring-neap case is discussed in Section 4.5.4.

4.5 Results and Discussion

4.5.1 Light Limitation Due to Sediment

In June 2010, the observed along-channel suspended-sediment concentrations are greatest near the salt front (Figure 4.3a). Here, the water column was well-mixed and resuspended sediment reaches the surface layer. SSC were also elevated roughly 20 km down-estuary of the salt front, though the resuspension did not reach as high in the water column due to stratification. Within the vicinity of the ETM, light absorption by surface sediment caused the 1% light level to be very shallow at approximately 3 meters below the sea surface (Figure 4.3b). Chlorophyll concentrations were maximal up- and down-estuary of the ETM, where light penetrated deeper. Observations of nitrate and oxygen provide supporting evidence that primary production was occurring in these regions, as the highest chlorophyll concentrations coincide with an uptake of nitrate and the production of oxygen (Figure 4.3c, d). Primary production appears to have shut down in the vicinity of the ETM where light levels were lowest, and the minimal oxygen levels indicate respiration.

The nitrate signal in Figure 4.3c is consistent with that reported by Sharp et al. (2009), who found nitrate to be high at the head of the tide, increase in the reach of the urban river, and then decrease towards the mouth due to dilution with coastal ocean water. While our observations are consistent with this described pattern and the depletion of nitrate towards the mouth may reflect some dilution with coastal water, we posit that the coincidence of nitrate depletion, oxygen production, and increased chlorophyll biomass is also indicative of uptake due to primary production. To confirm this, we plot the nitrate-salinity relationship from all the June 2010 casts against the theoretical conservative mixing curve (Figure 4.4). The concave deviation from conservative

mixing is consistent with that predicted for biogeochemical filtration (Sharp et al., 1984), indicating that nitrate is being removed by biological uptake.

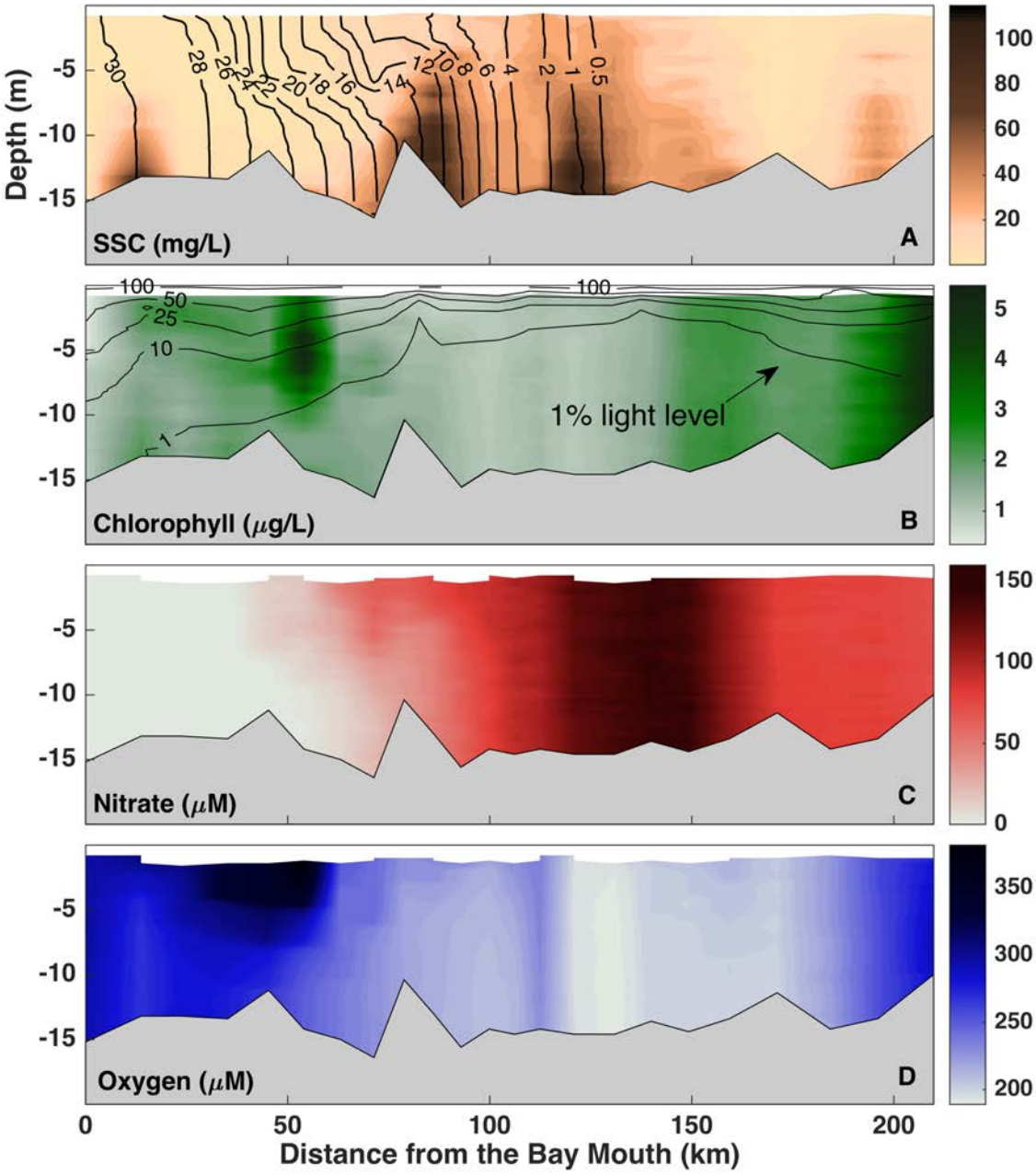

Figure 4.3 June 2010 along channel distribution of sediment (mg/L), chlorophyll $(\mu g / L)$, nitrate (μM), and dissolved oxygen (μM). Black contours in top panel are salinity and contours in second panel are PAR as a percentage of that at the surface.

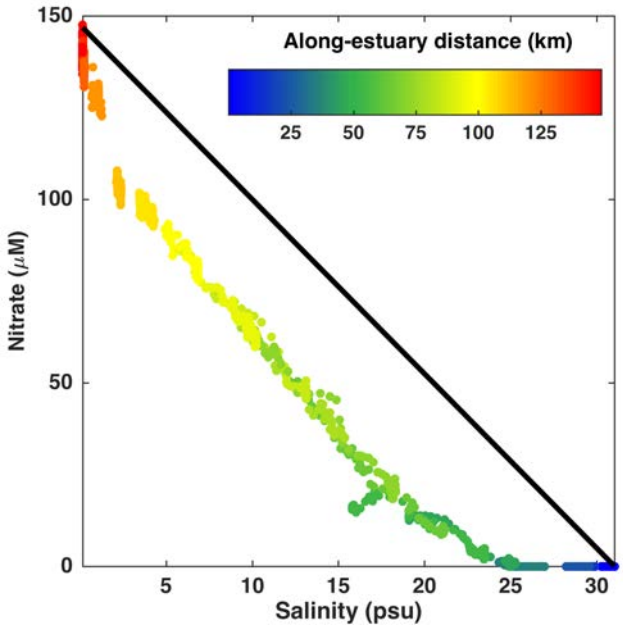

Figure 4.4 Nitrate concentrations (μM) versus salinity (psu) for the June 2010 cruise (dots) colored by the along-estuary distance compared to the theoretical conservative mixing curve connecting the high and low nitrate endpoints (black line).

To quantify the relationship between the sediment concentration and light absorption, we use a light-attenuation model based on our estimations of the specific attenuation coefficients (described in Section 4.4.1) as well as sediment and chlorophyll profiles. Figure 4.5 shows modeled and observed irradiance profiles for June 2010 and model-observation comparison for all June 2010 and September 2011 data. We show specific June 2010 mid-bay and upper profiles (Figure 4.5a) to illustrate that the fit can either overestimate or underestimate irradiance in the upper 1m of the water column, but that there is strong agreement between the model and observation below 1m depth. We note, though, that the upper- and mid- profiles shown in Figure 4.5a are not representative of all profiles in those vicinities; we show the poorer fits to illustrate the possible error but most of the profiles have a better fit.

Despite uncertainties in the light-attenuation model, the main conclusions of this analysis are robust. We ran sensitivity analyses with a range of model parameters to confirm the consistency of the described sediment-light paradigm.

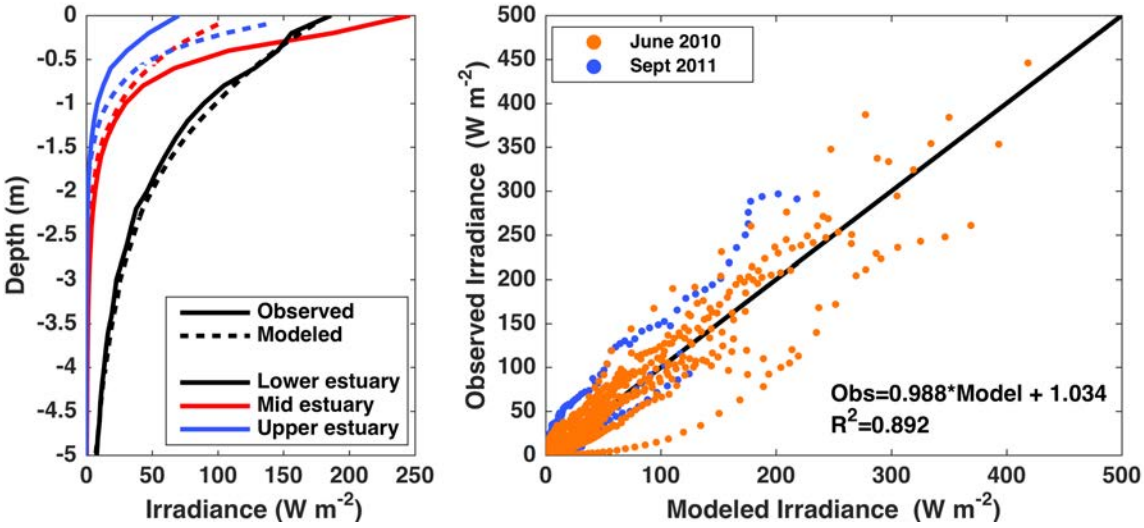

Figure 4.5 Comparison of observed and modeled irradiances. a) the observed irradiance profiles (solid lines) and the modeled irradiance profiles derived from Equation 4.3 (dotted lines) for locations in the lower (black), mid (red), and upper (blue) estuary in June 2010. b) The modeled irradiance versus the observed irradiance for all June 2010 and September 2011 data.

4.5.2 The Structure and Location of the Turbidity Maximum and Consequences for Productivity

The position of the salt intrusion front and the location of the ETM are modulated by river discharge (Figure 4.6), which generally has a seasonal cycle (Figure 4.2). During high river discharge, such as during the December months, the salt front and ETM move oceanward. In contrast, during low discharge the salt front and ETM migrate landward, as is seen in the June months. Since the salt front has a faster response time to river discharge changes, the movement of the ETM can lag such that the ETM is temporarily not co-located with the salt front. For example, in September 2011, a large

discharge peak pushed the salinity front down estuary but the ETM had not yet migrated oceanward (Figure 4.6).

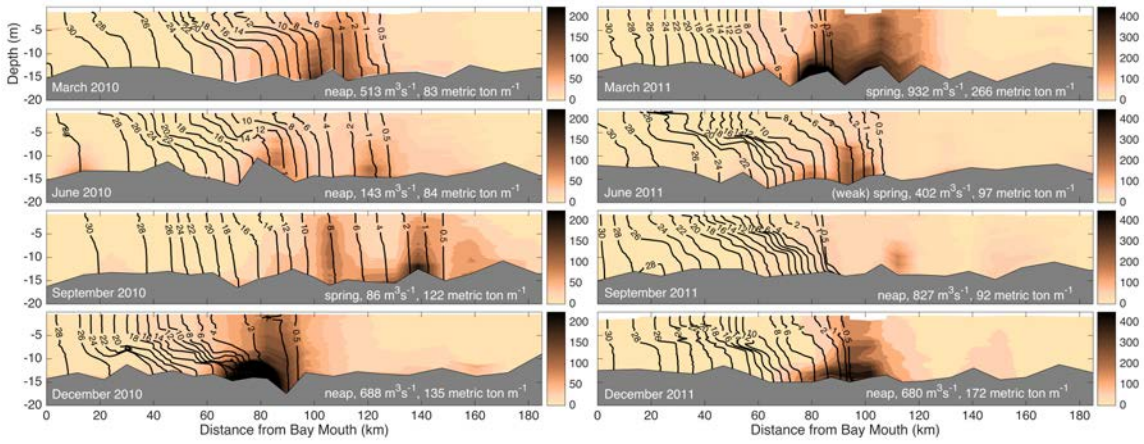

Figure 4.6 Suspended sediment concentrations (mg/L) for the 8 along-estuary surveys with salinity contoured in black. The river discharge and spring-neap conditions for each survey are noted in the bottom right of the panels.

Stratification conditions, which are modulated by both river discharge and spring-neap variability, play an important role in regulating the structure of the ETM. Whereas neap tides and high river flows drive more stratified conditions, the estuary tends to be well-mixed during low flow and spring tides. Though stratification in Delaware is usually very weak during spring tides, high river flows can drive persistent stratification even during spring tides (Aristizábal and Chant, 2014). At the leading landward edge of the salt front and ETM, the water column is often well-mixed and sediment is resuspended throughout the entire water column. In the interior (or tail) of the ETM, resuspension is most often limited to lower in the water column by stratification. This ETM structure is particularly evident in March, June, and December of both 2010 and 2011.

The ETM structure in the September months is more variable due to the combinations of river and tidal conditions. In September 2010, low river flows and

spring tides result in a mixed conditions throughout the estuary, which cause sediment that is normally limited to the lower layer to be resuspend throughout the water column and to the surface. In September 2011, high river flows and neap tides result in strongly stratified conditions, but the ETM is up-estuary of salt front due to the lagged migration of the ETM. Furthermore, the September 2011 cruise occurred after Tropical Storm Lee, and the observed sediment was likely remobilized recently from the tidal river. Sediment cores after Tropical Storm Lee confirmed that the bed was scoured in the reach of the fresh tidal river and that there was rapid deposition downstream of the salt wedge after the event (Duval, 2013). Since river discharge conditions in September are typically similar to those in 2010 (Figure 4.2), we posit that the along-channel salinity and ETM structure in 2010 is more representative of a typical September, in the absence of tropical storms.

Because Figure 6 shows snapshots from 2-day surveys, some of the turbidity structure may be associated with tidal aliasing. However, the range of tidal conditions that are encompassed in the observations along with the consistency of the observed ETM structures provide confidence that our results are robust. Stratification plays an important role in limiting the height of resuspension, particularly in the tail of the ETM, and Figure 4.6 clearly illustrates the linkage between the structure of the salt field and the height of suspended sediment. The seasonal cycle of river discharge and spring neap-variability clearly impact the surface SSC in the ETM zone, which has direct implications on the light available for production and consequent biogeochemical processes in the estuary.

Since primary production occurs at the water surface, the temporal sediment pattern at the surface is ultimately important. Figure 4.7 highlights sediment concentration, stratification, and chlorophyll concentrations 1.5 m below the surface as a function of river distance for the March, June, September, and December months. The consistency of the 2010 and 2011 surface data indicates that the sediment and stratification patterns are seasonal features. Surface sediment concentrations are highest in March and December, with notably heightened concentrations that coincide with river discharge peaks. Though high river flows drive strong stratification, the leading edge of the salt intrusion remains well-mixed even during these discharges and sediment is resuspended into the surface layer (Figure 4.6). Thus, the heightened sediment supply in March and December months is evident in the surface sediment concentrations (Figure 4.7).

The seasonality of stratification and surface SSC imply that spatial patterns of light attenuation also generally have a seasonal cycle. As such, light-limitation would spatially coincide with the ETM and the light environment would be more conducive to production down-estuary of the ETM. Indeed we observe that, aside from December when there are light and temperature limitations, the chlorophyll maximum is persistently found down-estuary of the ETM. This finding is consistent with historical observations (Pennock, 1985). There is also a chlorophyll peak up-estuary of the ETM in June, which we posit is likely due to a combination of elevated short-wave radiation and flushing rates that are slow enough for significant biomass to accumulate. Flushing times in the upper estuary, which is quite narrow, are sensitive to river discharge (Ketchum, 1952), resulting slow flushing rates during the dry months (Figure 2). Chlorophyll concentrations are

highest in March and minimal in December. The March chlorophyll maximum is consistent with the notion that stratification induced by the spring freshest limits sediment from being resuspended to the surface and permits the initiation of the spring bloom in the surface mixed layer. Though the discharge conditions similarly stratify the water column in the winter (Figure 4.6), there is significantly less sunlight in December to support productivity.

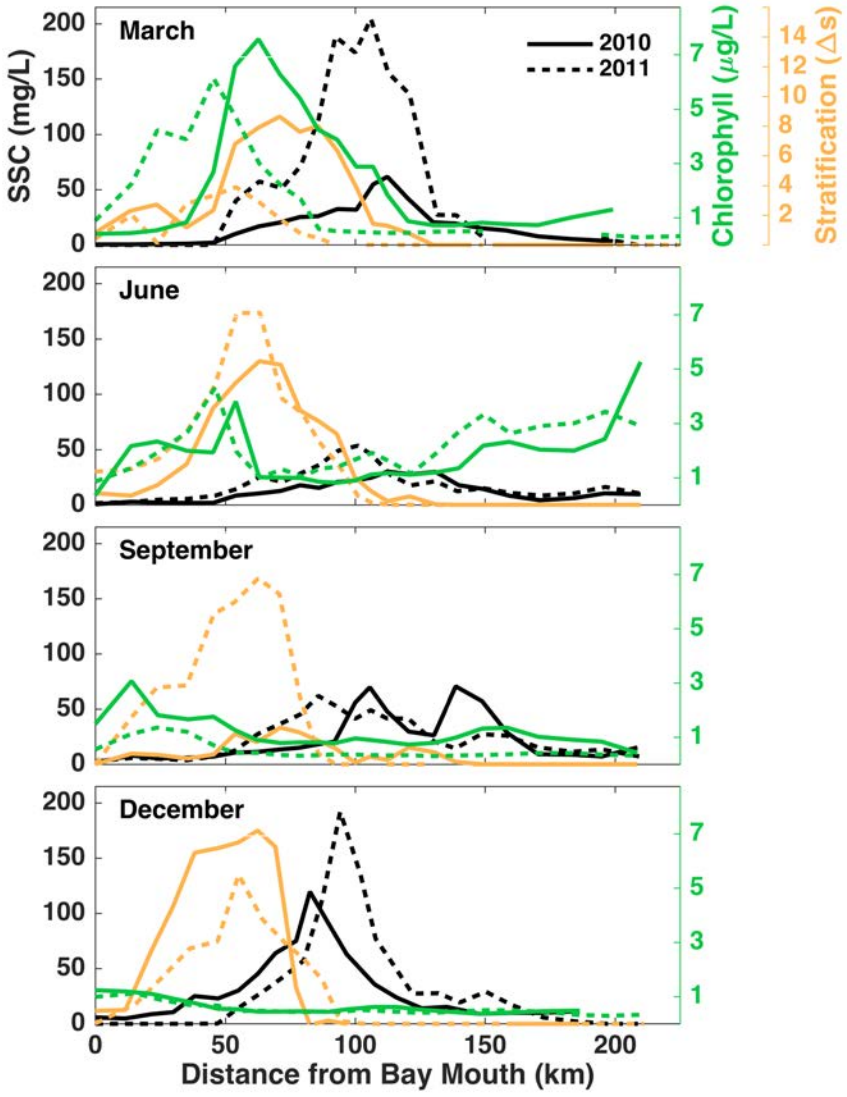

Figure 4.7 Suspended sediment concentration and chlorophyll 1.5 m below the surface and stratification calculated as bottom salinity- surface salinity (black, green and yellow lines, respectively) for 2010 (solid lines) and 2011 (dashed lines).

Our observations shed light on the seasonality of the physics that modulate the light environment, but the seasonality of the blooms themselves are a function of light availability and a number of factors not discussed here, such as temperature and grazing pressure. Our goal is to describe the role of stratification in influencing the bloom, which will likely modulate the perhaps larger seasonal scale variability associated with sunlight, temperature and grazing. Thus, our results provide context on the physics that control estuarine productivity in turbid estuaries and suggest that variability in seasonal production would be modulated primarily by river discharge and secondarily by spring-neap stratification.

4.5.3 The Role of River Discharge

To better understand how river discharge contributes to movement and structure of the ETM, we run a series of idealized ROMS models with different constant discharge values. The initial simulations are forced with M2 tidal currents on the order of 1.0 m s^{-1}, so spring-neap variability is not an influence. The simulations reach steady state after about 30 model days, and Figure 4.8 shows the steady state average solution (model day 30-60) for a run with 75 m^3 s^{-1} constant river discharge. Details of the ETM structure differ from the observations (Figure 4.6) which is unsurprising given the many differences between the idealized model geometry and reality, but the ETM still has the key features of resuspension through the entire water column near the well-mixed salt front and resuspension limited to a lower layer by stratification. Notably, the stratification is much shallower than observed in the estuary, so the tail of the ETM,

roughly between 70-80 km up-estuary from the bay mouth, occupies more of the water column.

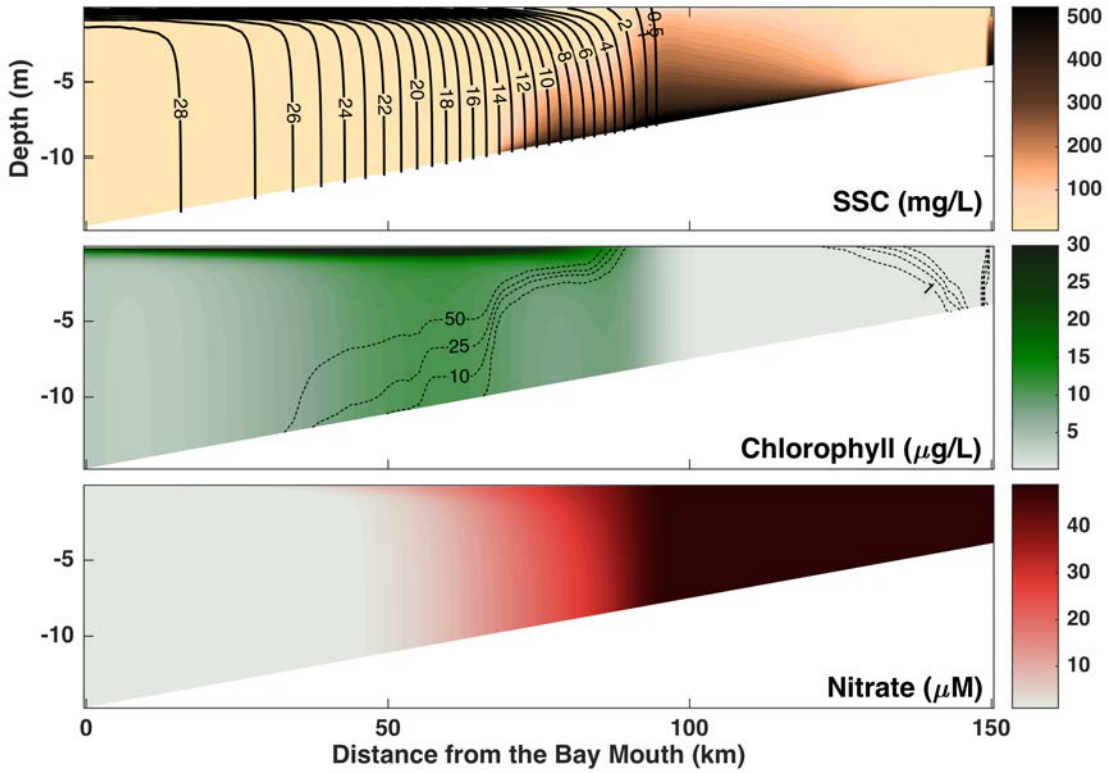

Figure 4.8 Model steady state average solution (model day 30-60) from a run with a river discharge of 75 $m^3 s^{-1}$. Same layout as Figure 4.3.

The chlorophyll concentrations are highest down-estuary of the turbidity maximum where stratification prevents sediment from reaching the surface. Chlorophyll is most concentrated in the surface layer, but some biomass is mixed down along the isopycnals. Production is notably low up-estuary of the ETM due to a combination of light-limitation from the riverine sediment input and fast flushing times.

Nitrate is depleted down-estuary of the turbidity maximum (Figure 4.8), and the modeled nitrate-salinity curve (Figure 4.9), colored by nitrate uptake and denitrification, confirms that nitrate in the system is depleted from the system due to primary production. The nitrate curve indicates that the along-estuary nitrate distribution is controlled by

uptake in addition to conservative mixing, verifying that the model is capturing nitrate dynamics similar to those observed (Figure 4.4). As the model assumes that detritus instantaneously remineralizes when it hits the bed, the nitrogen removed by denitrification was previously removed from the nitrate pool by uptake. The removal of nitrogen by nitrate uptake is an order of magnitude larger than that by denitrification and is greatest slightly up-estuary of the denitrification peak.

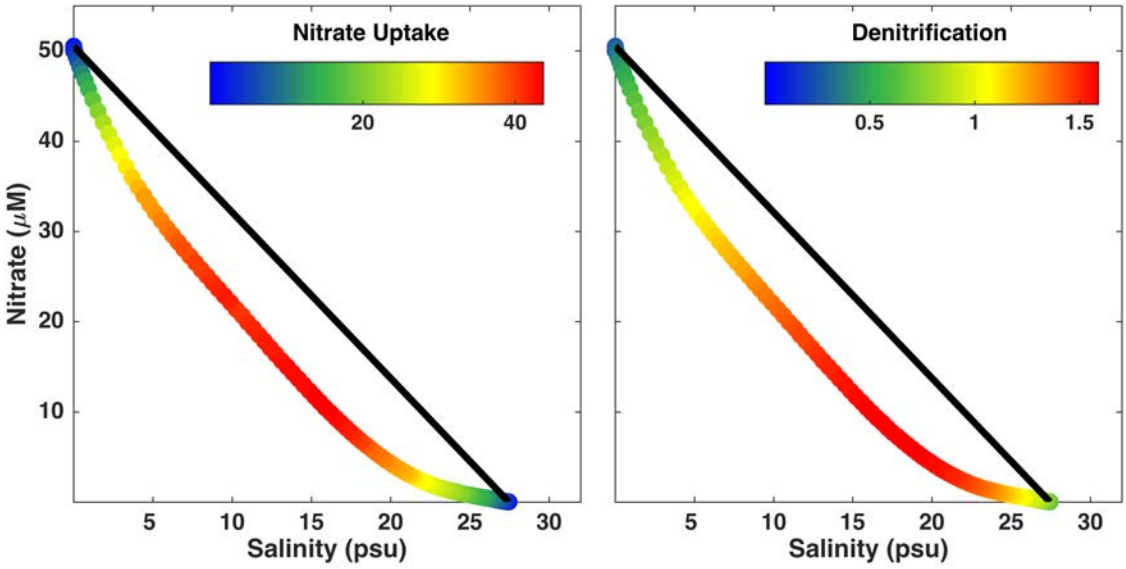

Figure 4.9 Modeled nitrate-salinity curve from the steady state average solution (model day 30-60) of the 75 m^3 s^{-1} simulation. Nitrate and salinity values are depth-averaged. On the left, the dots are colored by the depth integrated nitrate uptake (mmol N m^{-2} day^{-1}). On the right, dots are colored by denitrification (mmol N m^{-2} day^{-1}).

To evaluate how these spatial patterns are influenced by river discharge, we look at the along-channel distributions for 6 runs with constant river flows of 50, 75, 100, 125, 150, and 175 m^3 s^{-1}. These discharge values were chosen because the coinciding locations of the salt front and ETM are consistent within space with the observed range. However, the discharge values cannot be directly compared with observed discharge

ranges due to the difference in the model's cross sectional area and that of the bay. In order to draw a more direct comparison between the model and observations, we can calculate the river velocities, U_R, in the vicinity of the ETM by dividing the river discharge by the cross sectional area. The observed river velocities (Figure 4.2) are slightly weaker than those modeled (Figure 4.10), but the values are comparable.

Figure 4.10 shows the surface salinity, stratification, SSC, chlorophyll, and primary production as a function of along-estuary distance. As expected, the salt front moves down-estuary as the river discharge increases (Figure 4.8a). The modeled salt intrusion length scales with $Q^{-1/3}$ (black dots), which is consistent with classic estuarine theory (Hansen and Rattray, 1965; Monismith et al., 2002). The Delaware's salt intrusion length has been found to be less sensitive to discharge ($L \sim Q^{\approx -0.15}$) due to the tidal oscillatory salt flux, variability in the vertical eddy viscosity, and bathymetry (Aristizábal and Chant, 2013), so the model is not capturing dynamics explicitly specific to the Delaware.

The stratification increases with increasing discharge (Figure 4.10b) which is consistent with theory (MacCready and Geyer, 2010)and findings that the Delaware is most strongly stratified during the spring freshet. Stratification is minimal at the leading edge of the salt intrusion in every case and peaks about 5 km downstream of the salt intrusion. Notably, the reach of the strongest stratification also increases with increasing river flow, spanning roughly 25 km in the 50 m^3 s^{-1} case and 50 km in the 175 m^3 s^{-1} case.

Suspended sediment concentrations at the surface (Figure 4.10d) is always greatest just up-estuary of the salt front. In every river flow case, there is a sharp transition to no sediment in the surface mixed layer that coincides with stratification. As

river flow increases, the concentrations of resuspended sediment increase due to stronger flows. Consistent with observations, the sediment concentrations at the surface are roughly a third of those at the bed.

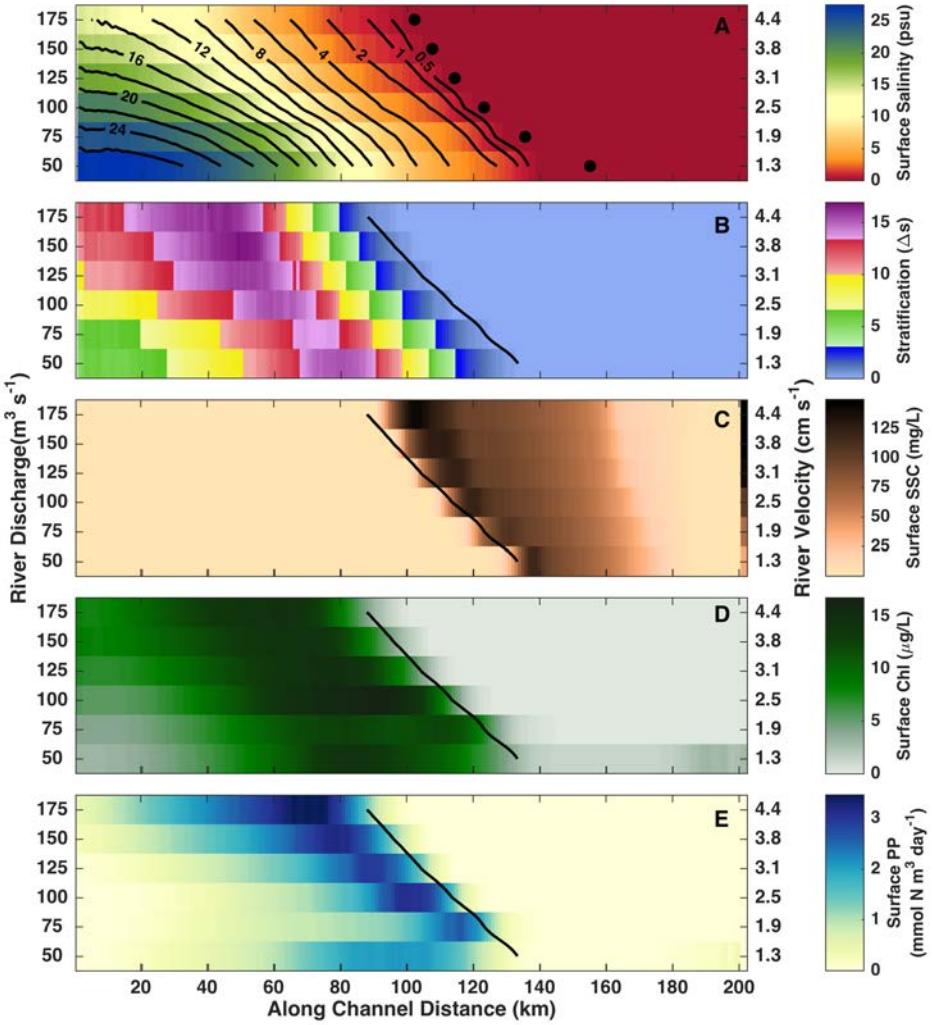

Figure 4.10 Steady state averaged model results (model day 30-60) for simulations with 6 different river discharges – 50, 75, 100, 125, 150, 175 $m^3 s^{-1}$. For panels a-b, the y-axis shows the river discharge values and for panels c-e, the y-axis is expressed in terms of the river velocities, which range from 1.3 to 4.4 cm s^{-1}. The 1psu surface isohaline is drawn in each panel for reference. a) the along-channel surface salinity (psu) with specific isohalines contoured and the theoretical salt intrusion length based on $L \sim Q^{-1/3}$ (black dots). b) the stratification $\left(\partial s / \partial z\right)$ at the surface c) the sediment concentration (mg L^{-1}) at the surface d) the chlorophyll concentration (μg L^{-1}) at the surface e) the surface new primary production (mmol N $m^3 day^{-1}$)

Unsurprisingly, the chlorophyll peaks move down estuary with increasing river discharge (Figure 4.10e). Chlorophyll concentrations are nearly zero near the salt intrusion front where sediment reaches the surface. Just down-estuary, where light becomes available due to sediment being trapped by stratification below the surface mixed layer, a bloom is initiated. Chlorophyll concentrations then accumulate with distance down-estuary, as production continues and chlorophyll biomass is moved ocean-ward. Chlorophyll concentrations are slightly elevated up-estuary of the turbidity maximum in the low-flow case, which is consistent with the chlorophyll distribution observed in the June months.

Primary production is greatest in the stratified reaches of the estuary, just oceanward of the turbidity maximum for all river discharge cases. Primary production rates tend to decrease further down-estuary (Figure 4.10d), where nutrients are less abundant. In the lower discharge case, there is weak production up-estuary that coincides with chlorophyll peak similar to that observed in June cruises.

Estuarine circulation inherently controls the steady state solutions shown in Figure 4.10. For example, the estuarine circulation plays a key role in modulating the location of the salt front (Hansen and Rattray, 1965) and consequently the ETM. The axial sediment distribution is modulated by estuarine processes, as convergent fluxes trap sediment within the ETM region. The depth-integrated sediment flux in the ETM is relatively weak, and vertical mixing on a tidal timescale controls the surface SSC signal in the ETM and therefore the light limitation. The location of primary production is controlled by the estuarine physics that modulate light availability, but the resulting chlorophyll biomass will be advected down-estuary at the surface due to the vertical

structure of the riverine and estuarine exchange velocities. The spatial scale of this advection is visible in the comparison of Figure 14.0d and Figure 4.10e.

The coincidence of the spatial patterns of sediment , chlorophyll and production within the ETM is direct evidence that the structure of the suspended-sediment concentration field directly affects primary productivity.

4.5.4 Spring-Neap Variability

Our findings that river discharge plays a critical role in modulating the spatial pattern of stratification, sediment, light-limitation, and productivity on a subtidal timescale is consistent with both observations and other modeling efforts (De Swart et al., 2009). Because the salinity front, stratification, and ETM position also vary on spring-neap timescales (Aristizábal and Chant, 2014; McSweeney et al., 2016a), it is possible that spring-neap variability sometimes enhances or masks variability driven by changes in the river discharge. Thus, we conduct a further simulation that includes M2 and S2 tides to tease apart the relative contributions of river discharge and spring-neap variability.

Stratification is modified significantly on a spring-neap timescale, with the water column more strongly stratified during neap tides compared to spring tides (Figure 4.11b). Correlated with stratification, sediment concentrations in the surface waters during spring tides are roughly double those during than neap tides due to the prevalence of mixed conditions (Figure 4.11b, c). With stratification and bottom stress related through the Simpson number (Simpson et al., 1990), bottom stress is predictably reduced during neap tides (Figure 4.11e). Consequently, the SSC a meter above the bed also

shows spring-neap variability, with spring tides resuspending almost double the amount of sediment resuspended during neap tide (Figure 4.11d). Notably, bottom stresses during the neap tide at the end of January were below the critical erosion stress and yet there was still a significant amount of sediment suspended a meter above the bed. This sediment is material that had not yet settled to the bed, demonstrating that the sediment inventory in the water column is not entirely composed of newly suspended sediment. Thus, while spring-neap variability of bottom stress definitely contributes to sediment resuspension, it is the spring-neap variability of stratification that is the main control on SSC that reaches the surface. Since surface SSC directly impacts light attenuation, there is a nearly two-fold increase in production that coincides with the increased stratification and lower surface SSC during neap tides (Figure 4.11f).

Stratification, bottom stress, and surface and bottom SSC also vary on a tidal timescale, with stratification decreased and bottom stress and SSC increased on flood tides. However, the primary production signal has a diurnal signal that coincides with incoming radiation rather than a tidal signal. Since the timescales of biomass accumulation are longer than a tidal timescale, we conclude that the tidal modulation of stratification and surface SSC is less important to light-limited productivity than spring-neap.

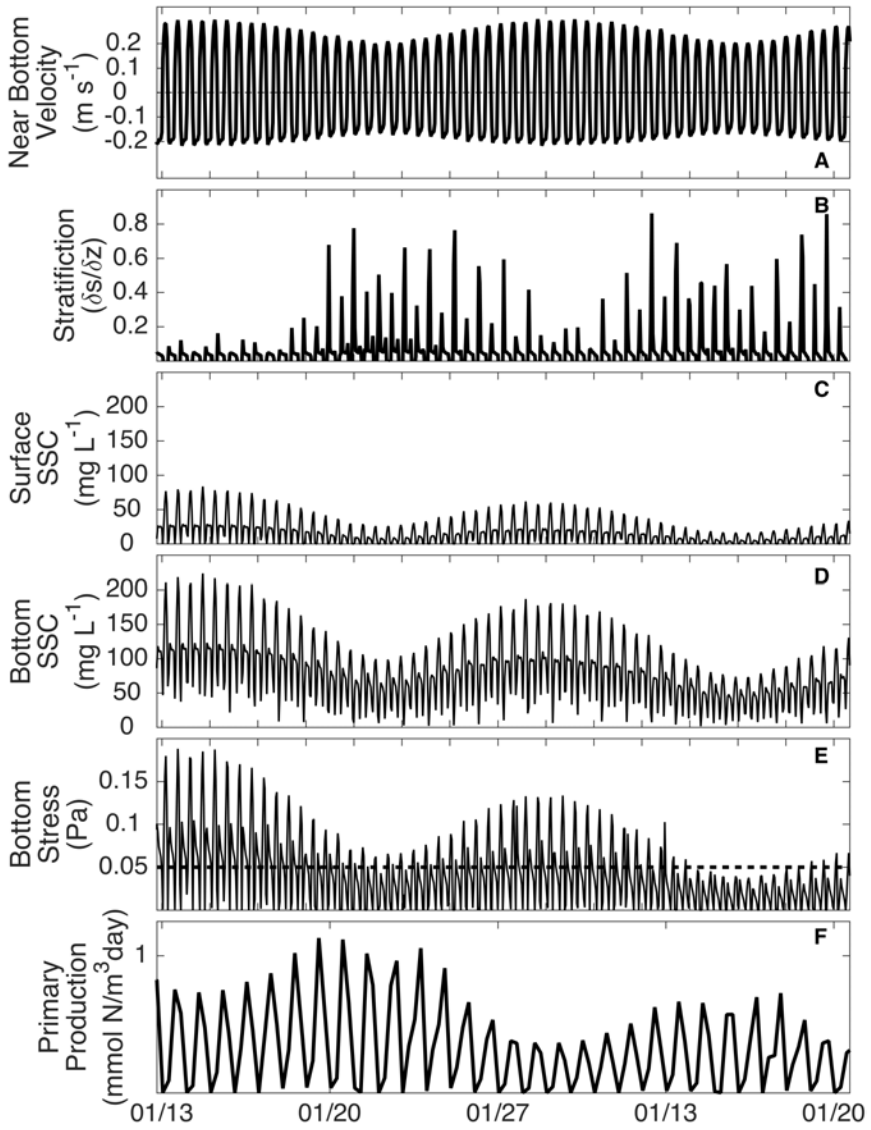

Figure 4.11 Model output over a spring-neap cycle from a simulation with a constant river discharge a) The near-bottom velocities at a location near the salt intrusion. b) The average stratification, calculated by the difference in top and bottom salinity at each vertical level c) the surface SSC (mg L^{-1}) d) the SSC a meter above the bed (mg L^{-1}), e) the bottom stress (Pa) at the bed compared to the critical erosion stress (dashed line) f) the primary production rate (mmol N m^{-3} day^{-1})

Similar to the spring-neap variability of stratification seen in the model (Figure 4.11), the Delaware Estuary becomes significantly stratified during neap tides. Figure 4.12b shows the stratification conditions at a mooring site in the vicinity of the ETM

over a spring-neap cycle in July 2011. During the spring tides (shaded in grey), the site is fairly well-mixed with slight stratification developing on a tidal timescale. During neap tide however, there is a salinity difference of roughly 10 psu between the surface and bottom. Looking at 3 cross-sections during neap tide 26 July 2011 (Figure 4.12c-h), it is evident that estuary is strongly stratified. The optical backscatter signal, a proxy for sediment concentration, indicates that sediment can be mixed to the surface where stratification is weak but that sediment is prevented from reaching the surface in more strongly stratified areas. We note that the optical backscatter signal at km 7 in Figure 4.12e may be capturing chlorophyll biomass that is similar in size to sediment particles. Generally, the chlorophyll maxima spatially coincide with areas of strong stratification and low surface sediment, and the blooms are constrained to the surface layer by stratification. These observations, coupled with the spring-neap model, emphasize that tidal variability can modulate stratification even under conditions of constant river discharge which significantly impacts suspended-sediment concentration (Sommerfield and Wong, 2011) and by extension productivity.

While the distribution of chlorophyll and sediment is predominantly controlled by along-channel processes, the cross-sectional observations (Figure 4.12) hint that the chlorophyll blooms may have lateral structure related to lateral stratification and sediment features (McSweeney et al., 2016a). These observations provide motivation to study the 3-dimensional nature of sediment impacts on light-limited productivity in future work.

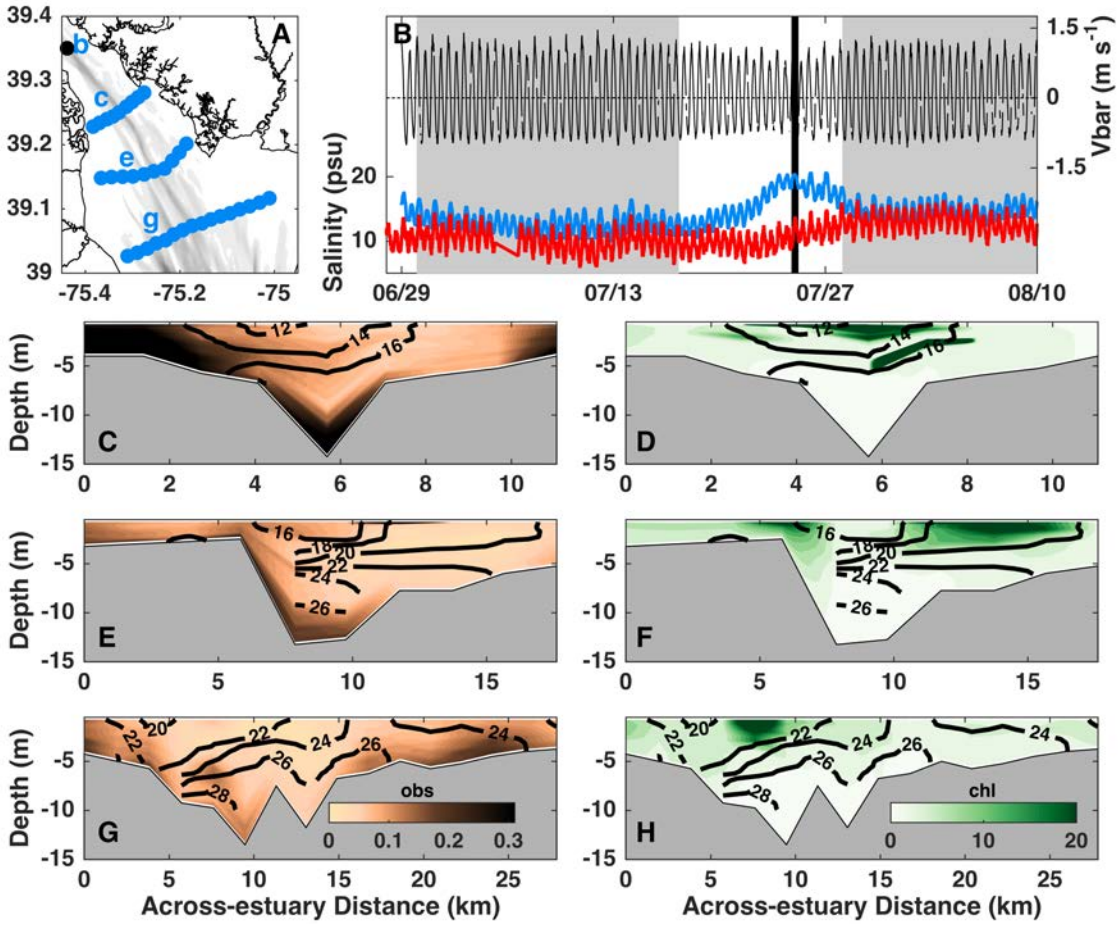

Figure 4.12 Cross-sectional data during a neap tide. A) Map of the mooring location (black dot) and three cross-channel sections (blue dots). Bathymetry.is contoured in grey. B) Depth averaged velocity (black line, m s^{-1}) and surface (red line) and bottom (blue line) salinity from the mooring shown by black dot in (A). The spring tide is shaded grey, the neap tide is white. c-h) Observations from the 3 cross-channel sections (C and D, E and F, and G and H corresponding with labels c, e, and g respectively panel A) 26 July 2011. The brown shading is optical backscatter, a proxy for sediment (C, E, G, volts), the green shading is chlorophyll concentrations (D, F, H, µg L^{-1}) and the black contours are salinity (psu).

4.5.5 Implications for Modeling Primary Productivity

In order to contextualize the importance of sediment absorption of light, we run the model with and without the sediment absorption included in the total light attenuation. Figure 4.13 shows the average primary production (mmol N m^{-3} day^{-1}) for the river discharge 75 m^3 s^{-1} case (M2 only) where only Equation 4 is altered. When light

attenuation by sediment is accounted for, we see production at the surface down-estuary of the ETM and no production where sediment is resuspended to the surface. When sediment is in the model but not attenuating light, production is spread along the estuary (Figure 4.13b). Comparing the two spatial patterns in Figure 4.13 with observations of chlorophyll and nitrate (Figure 4.3), it is evident that sediment attenuation can play a key role in controlling the spatial distribution of productivity.

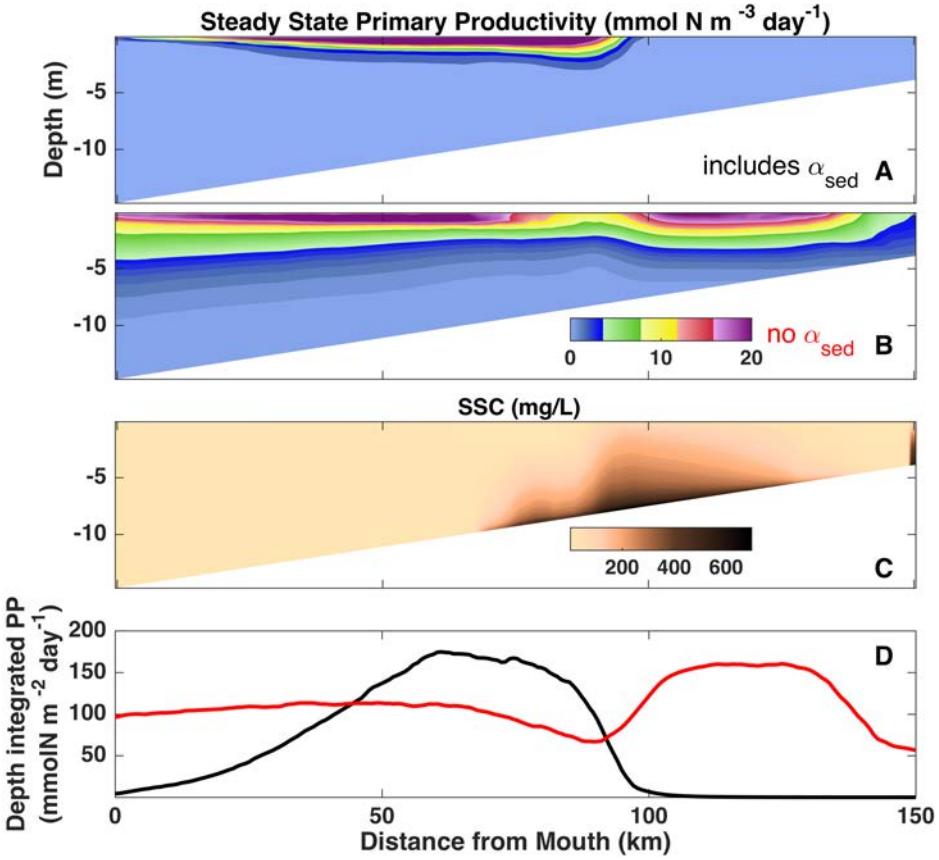

Figure 4.13 Steady state model results of primary productivity (mmol N m^{-3} day^{-1}) for 2 runs that are identical except for the absorption coefficient. River discharge is 75 m^3 s^{-1}. a) the absorption coefficient includes absorption by water, chlorophyll and sediment b) the absorption coefficient includes absorption by water and chlorophyll. c) the steady state sediment distribution (mg/L). d)The depth integrated primary production for the case A (black) and B (red).

This result highlights the importance of including sediment and light attenuation by suspended sediment in biogeochemical models of turbid estuaries. Models that do not account for sediment attenuation will miss key light-limitations and thus overestimate the levels of primary productivity that can be supported. Figure 4.11c suggests that the overestimations may be especially important up- and down- estuary of the true bloom location. There is an increasing amount of evidence that modeling light absorption in coastal and estuarine systems should be of high importance (Desmit et al., 2005; Arndt et al., 2007), and yet these linkages are poorly represented in many biogeochemical models. Our study provides further evidence that the linkages between hydrodynamics, suspended sediment, light, and productivity are important, emphasizing that stratification is key to understanding how these processes are interconnected. Since stratification can vary on tidal and seasonal timescales, it is important to consider the affects of both river discharge and spring-neap variability of light-limitation.

As noted in Section 4.4.2 we also ran the model with two different α_{sed} values to evaluate how our estimations compare to that by Pennock (1985). The model output for the two sediment attenuation values did not vary significantly. The spatial patterns described were very similar, with a slight impact on the magnitudes of production and chlorophyll concentration. Because the attenuation coefficient is estimated from the relationship between sediment and light, it is possible that the difference between our estimation and that of Pennock (1985) is indicative of a temporal shift in the properties of the sediment. A study of the Rhode River, a tributary of the Chesapeake Estuary, concluded that a shift towards smaller, organic particles impacted water clarity despite similar SSC concentrations (Gallegos et al., 2005). Further work would be needed to

determine if a shift in sediment size such as that observed in the Rhode River is happening in the Delaware or if the variability is merely a result of the observational time periods capturing different ETM ratios of biogenic and mineral material. For example, biomarker and stable isotope carbon analysis of samples from these cruises indicate that discharge in the winter and spring delivers higher levels of terrestrial matter (Hermes, 2013), which would impact the sediment-specific absorption. Regardless, based on our model sensitivity runs, we conclude that the impacts of sediment on light-limitation patterns are relatively insensitive to the observed variations in α_{sed} compared to the sensitivity to sediment concentration.

4.6 Conclusions

Sediment resuspension and concentration plays an important role in limiting light-availability and primary production in turbid estuaries. The Delaware Estuary is a high-nutrient, low-growth environment whose water quality is thought to be largely controlled by sediment attenuation of light. This study uses observations from eight along-estuary surveys and an idealized ROMS model to focus on the interactions between the ETM, light-limitation, and productivity, emphasizing the role of stratification and sediment dynamics. While the location of the ETM is largely controlled by river discharge, the ETM structure is controlled by stratification due to both river inflow and spring-neap variability. The leading edge of the ETM tends to follow the salt intrusion front and is characterized by resuspension that spans the entire water column, compared to the tail of the ETM which is confined below the surface mixed layer by stratification. We observe that the depth of the 1% light level is primarily controlled by this structure and thus

shallows in the vicinity of the ETM where resuspension reaches the surface. Consequently, production is minimal in the ETM region due to light-limitations, and chlorophyll concentrations are maximal down-estuary of the turbidity maximum.

The location and structure of the turbidity maximum varies with river discharge, causing notable seasonal variability of the sediment and chlorophyll spatial patterns. Surface sediment concentrations in the ETM region are maximal in March and December months due to the delivery of sediment by high river flows. However, despite the similar ETM features, the along-channel distribution of chlorophyll is significantly different in the winter and spring. In March, the stratification induced by higher river discharge plays a key role in limiting resuspension to lower in the water column in the tail region of the ETM, initiating phytoplankton blooms in the surface mixed layer. In the winter months, the surface mixed layer is significantly deepened such that the stratification, coupled with little sunlight, is less conducive to productivity.

Our results highlight that both high river flows and neap tides can drive stratification that is sufficient to prevent suspended sediment from reaching the surface, thus creating light conditions favorable for primary production. Previous studies have classified Delaware to be well-mixed, such that light-limitation is a persistent control on production except for in cases on increased river run-off (Pennock and Sharp, 1986). Here, we suggest that even in low river discharge conditions, neap tides can drive stratification that limits sediment from being resuspended into the surface layer.

We ran an idealized ROMS model with the diffuse attenuation coefficients including and excluding the attenuation by sediment to isolate the contribution of sediment attenuation to the spatial patterns of productivity. From this model comparison,

we conclude that the absorption of light by surface sediment is an extremely important factor that controls the spatial distributions of productivity, chlorophyll, nitrate, and oxygen that are observed in high-nutrient, low-growth turbid estuaries Therefore, we posit that biogeochemical models of urbanized turbid estuaries may grossly overestimate productivity and miss important spatial and temporal patterns if they do not account for the suspended sediment attenuation of light.

While our analysis focuses on observations from the Delaware Estuary and a complementary model, the mechanisms discussed in this paper are broadly applicable to turbid estuaries with an excess of nutrients. Since the salinity front modulates the location of the ETM, an estuary's along-channel sediment distribution will respond to river discharge changes, which are predictably seasonal in most systems. Furthermore, because estuarine stratification is known to increase with neap tides and strong river flows, resuspended sediment within an ETM may not reach the surface during these conditions. Since the magnitude and duration of stratification are key factors to whether sediment is resuspended to the surface layer, the relative importance of both river discharge and spring-neap variability may vary from system to system. In some estuaries, high river flow can push the salt field out of the system entirely, in which case the entire estuary would become fresh and likely turbid at the surface due to the lack of stratification. Or, even if the salt field remains in the estuary, the stratified region can be shortened significantly and the flushing time would be too great for chlorophyll biomass to accumulate within the stratified region.

Another factor to consider in this paradigm is the size and sinking velocity of the sediment types. For example, the described mechanisms may be confounded in certain

cases, such as a river discharge event that delivers extremely fine sediment. If the sinking velocities are low enough and the estuary becomes strongly stratified, the increased sediment load could become trapped at the surface by stratification. In that scenario, stratified conditions would coincide with increased light attenuation by sediment and a poor environment for production. Therefore, the conclusion that stratification plays an important role in modulating sediment concentrations at the surface and light-availability is robust, but the implications of this mechanism can impact estuarine systems differently.

4.7 Acknowledgements

We thank Eli Hunter, Maria Aristizábal, Anna Hermes, and the *R/V Hugh Sharp* crew for their dedication to the field campaign. Special thanks to Aboozar Tabatabai and Alex López for helpful feedback regarding the model development. Data collection was funded through National Science Foundation grants OCE-0928567 and OCE-0825833 to R. Chant, and OCE-0928496 to C. Sommerfield. This material is also based upon work supported by the Department of Marine and Coastal Sciences at Rutgers University and the National Science Foundation Graduate Research Fellowship under grant no. DGE-0937373. The data collected in this study and the model output can be accessed at: *http://tds.marine.rutgers.edu/thredds/roms/catalog.html*. or by contacting Jacqueline McSweeney at jmcsween@marine.rutgers.edu.

Chapter 5: Conclusions

The estuarine turbidity maximum (ETM) in Delaware Estuary has a 3-dimensional structure that is influenced by spatiotemporal patterns in axial and lateral sediment transport. Understanding the spatial complexity of the ETM and how it may vary on different timescales is scientifically challenging because of its intrinsic variability and the limited observational resources available. Many studies lack the spatial or temporal resolution necessary to resolve the sediment dynamics that drive such rich variability. Furthermore, the estuary's funnel shape, regions of curvature, and asymmetric cross-channel bathymetry all contribute to the challenge of capturing accurate sediment dynamics in modeling efforts. This thesis utilizes a suite of resources to describe sediment transport dynamics in Delaware Estuary and to explore how their variability impacts the structure of the ETM and trapping efficiency of the system. These resources include: 6 months of data from a cross-channel mooring transect, 2 years of seasonal along-channel surveys, 4 cross-channel tidal surveys, an idealized 2-D Regional Ocean Modeling System (ROMS) coupled hydrodynamic, sediment, and biogeochemical model, and a 3D ROMS coupled hydrodynamic and sediment model with realistic forcings.

In Chapter 2, sediment fluxes at 7 mooring locations in the vicinity of the ETM are decomposed into the tidal pumping and mean advective components. Since the data span 6 months, the influence of spring-neap variability and river discharge on sediment transport patterns can be determined. During high river discharge, sediment is exported at all locations across the channel whereas during low discharge, sediment is exported on the Delaware (DE) flank and imported in the channel. These spatiotemporal patterns are driven by both tidal pumping and mean advection, with tidal pumping comprising about

30% of the total along-estuary transport. The data suggest that export by tidal pumping occurs on the flanks because stratification is strongest on the flood tide and that tidal pumping import in the channel occurs when stratification is enhanced on ebb. In contrast to the along-channel sediment fluxes, the lateral sediment transport is insensitive to river discharge and is driven almost entirely by the mean advective flux. There is a pattern of persistent lateral divergence over the slope of the DE flank-channel transition and the mean sediment transport is directed westward towards the DE coastline. From this observational analysis, it is clear that the structure of the ETM is laterally strained by the cross-channel variability of sediment transport. This lateral straining of the ETM can reinforce sediment reworking within the ETM, ultimately impacting the estuary's trapping efficiency.

In Chapter 2, a realistic ROMS model of Delaware Estuary with coupled hydrodynamics and sediment dynamics is used to elucidate broader sediment transport patterns. The residual circulation is described at 7 cross-sections along the axis of the estuary. The time-averaged sediment transport at each cross-section is compared to maps of the depth-integrated, time-averaged sediment transport. The combination of these perspectives provides insight about the spatial variability beyond a single transect location and the role of the vertical structure of the flow field.

Sediment transport patterns are also evaluated on spring-neap, seasonal, and annual timescales. Whereas the along-estuary sediment transport is significantly modulated by river discharge, the lateral fluxes are relatively insensitive to changes in freshwater inflow. On a spring-neap timescale, there are competing mechanisms that contribute to spatially variable spring-neap variability. That is, spring tides are associated

with stronger bed stresses and more resuspension, but neap tides generate stronger stratification and lateral flows. The net effect is that along-channel sediment fluxes are stronger on neap but do not have much spring-neap spatial variability, whereas the magnitude of the lateral fluxes are comparable but the spatial patterns vary on spring-neap. Pathways of sediment reworking and export are most obvious on an annual timescale, and the findings demonstrate that the annual residual circulation has strong impacts on the trapping efficiency.

The realistic model is additionally used to analyze the cross-channel momentum balances in the upper estuary, ETM, and lower estuary. In the upper estuary, flow curvature is a main force generating lateral flows, whereas in the ETM, both differential advection and geostrophy contribute to secondary circulation. In the lower estuary, Ekman is the dominant balance and the lateral circulation becomes more complex due to the lateral bathymetry. Lateral circulation plays an important role in modulating the variability of sediment transport mechanisms, and the momentum balance demonstrates that that the key lateral processes vary along the axis of the estuary.

In Chapter 3, data from a series of along-channel surveys and an idealized 2D ROMS model are used to evaluate the impact of sediment dynamics on light availability and consequent productivity. The location of the ETM is influenced by river discharge conditions, whereas the vertical structure of the along-channel sediment distribution is controlled by stratification, which varies with spring-neap conditions and river discharge. When sediment is resuspended to the surface waters in areas of weak stratification, such as at the salt intrusion front, light is attenuated quickly and primary production is light-limited. In the stratified region of the ETM, seaward of the salt intrusion, sediment is

limited to lower in the water column by stratification and consequently more light is available. Thus, algal blooms are co-located with the stratified regions of the ETM. This work highlights the broader importance of sediment dynamics and demonstrates the connectivity between physical mechanisms driving transport and biogeochemical patterns that have been observed in the Delaware Estuary.

The ETM is a key location of sediment trapping and storage in the Delaware Estuary, and this thesis sheds light on the mechanisms that control sediment dynamics. Much of the fundamental research motivating this research was based on spatially-limited data and/or idealized models with simple bathymetry. This dissertation expands our understanding of estuarine sediment dynamics by addressing lingering questions related to spatiotemporal variability in a system with asymmetric cross-channel bathymetry, flow curvature, and variable width.

Ultimately, the spatiotemporal variability of sediment fluxes described in this dissertation inform broader issues related to estuarine sediment. For example, the export pathways identified in Chapter 3 that facilitate sediment transport towards the estuarine shoreline may play an important role in regulating sediment supply to the marshes. Furthermore, the observations of axial convergence of sediment on the DE slope of the channel-flank transition provide insight about where future dredging efforts may need to be focused. Since our findings indicate that sediment rarely leaves the estuarine system, even in the event of strong river discharges, it is probable that management strategies related to future cases of particle-bound contamination can be focused within the system. The sediment transport patterns described influence ecosystems through habitat impact, modification of light availability, and water quality. This dissertation not only advances

our understanding of physical sediment transport mechanisms, but also has important societal and economic impact.

Acknowledgement of Previous Publications

Chapter 2 has been published in the scientific journal *Journal of Geophysical Research: Oceans*.

McSweeney, J. M., R. J. Chant, and C. K. Sommerfield (2016), Lateral variability of sediment transport in the Delaware Estuary, *J. Geophys. Res. Oceans*, 121, 725–744, doi:10.1002/ 2015JC010974.

Chapter 4 is in revision for publication in the scientific journal *Estuaries and Coasts*.

McSweeney, J. M., R. J. Chant, J. L. Wilkin, and C. K. Sommerfield. (in revision), Suspended-Sediment Impacts on Light-Limited Productivity in Delaware Estuary, *Estuaries and Coasts*.

References

Allen, G. P., Salomon, J., Bassoullet, P., Du Penhoat, Y., and De Grandpre, C.: Effects of tides on mixing and suspended sediment transport in macrotidal estuaries, Sedimentary Geology, 26, 69-90, 1980.

Aristizábal, M., and Chant, R.: A numerical study of salt fluxes in Delaware Bay Estuary, Journal of Physical Oceanography, 2013.

Aristizábal, M., and Chant, R.: Mechanisms Driving Stratification in Delaware Bay Estuary, Ocean Dynamics, 64, 1615-1629, 2014.

Aristizábal, M. F., and Chant, R. J.: An observational study of salt fluxes in Delaware Bay, Journal of Geophysical Research: Oceans, 2015.

Arndt, S., Vanderborght, J. P., and Regnier, P.: Diatom growth response to physical forcing in a macrotidal estuary: coupling hydrodynamics, sediment transport, and biogeochemistry, Journal of Geophysical Research: Oceans, 112, 2007.

Beardsley, R. C., and Boicourt, W. C.: On estuarine and continental-shelf circulation in the Middle Atlantic Bight, Evolution of physical oceanography, 198-233, 1981.

Becherer, J., Stacey, M. T., Umlauf, L., and Burchard, H.: Lateral Circulation Generates Flood Tide Stratification and Estuarine Exchange Flow in a Curved Tidal Inlet, Journal of Physical Oceanography, 45, 638-656, 2015.

Bianchi, T. S.: Biogeochemistry of estuaries, Oxford University Press, 2007.

Biggs, R. B., Sharp, J. H., Church, T. M., and Tramontano, J. M.: Optical properties, suspended sediments, and chemistry associated with the turbidity maxima of the Delaware Estuary, Canadian Journal of Fisheries and Aquatic Sciences, 40, s172-s179, 1983.

Biggs, R. B., and Beasley, E. L.: Bottom and suspended sediments in the Delaware River and Estuary, Ecology and Restoration of the Delaware River Basin, 116-131, 1988.

Burchard, H., and Baumert, H.: The formation of estuarine turbidity maxima due to density effects in the salt wedge. A hydrodynamic process study, Journal of Physical Oceanography, 28, 309-321, 1998.

Chant, R. J.: Secondary circulation in a region of flow curvature: Relationship with tidal forcing and river discharge, Journal of Geophysical Research: Oceans (1978–2012), 107, 14-11-14-11, 2002.

Chant, R. J., Geyer, W. R., Houghton, R., Hunter, E., and Lerczak, J.: Estuarine boundary layer mixing processes: Insights from dye experiments*, Journal of Physical Oceanography, 37, 1859-1877, 2007.

Chant, R. J., Fugate, D., and Garvey, E.: The shaping of an estuarine superfund site: Roles of Evolving Dynamics and Geomorphology, Estuaries and Coasts, 34, 90-105, 2010.

Chatwin, P.: Some remarks on the maintenance of the salinity distribution in estuaries, Estuarine and Coastal Marine Science, 4, 555-566, 1976.

Cheng, P., Li, M., and Li, Y.: Generation of an estuarine sediment plume by a tropical storm, Journal of Geophysical Research: Oceans, 118, 856-868, 2013.

Cloern, J. E.: Tidal stirring and phytoplankton bloom dynamics in an estuary, Journal of marine research, 49, 203-221, 1991.

Cook, T. L., Sommerfield, C. K., and Wong, K.-C.: Observations of tidal and springtime sediment transport in the upper Delaware Estuary, Estuarine, Coastal and Shelf Science, 72, 235-246, 2007.

De Swart, H., Schuttelaars, H., and Talke, S.: Initial growth of phytoplankton in turbid estuaries: A simple model, Continental Shelf Research, 29, 136-147, 2009.

Desmit, X., Vanderborght, J.-P., Regnier, P., and Wollast, R.: Control of phytoplankton production by physical forcing in a strongly tidal, well-mixed estuary, Biogeosciences, 2, 205-218, 2005.

Devlin, M., Barry, J., Mills, D., Gowen, R., Foden, J., Sivyer, D., and Tett, P.: Relationships between suspended particulate material, light attenuation and

Secchi depth in UK marine waters, Estuarine, Coastal and Shelf Science, 79, 429-439, 2008.

Domingues, R. B., Barbosa, A., and Galvao, H.: Nutrients, light and phytoplankton succession in a temperate estuary (the Guadiana, south-western Iberia), Estuarine, Coastal and Shelf Science, 64, 249-260, 2005.

Duval, D.: Sedimentary response of the Delaware Estuary to tropical cyclones Irene and Lee in 2011, University of Delaware, 2013.

Dyer, K.: Coastal and estuarine sediment dynamics, Chichester: Wiley, 1986.

Fennel, K., Wilkin, J., Levin, J., Moisan, J., O'Reilly, J., and Haidvogel, D.: Nitrogen cycling in the Middle Atlantic Bight: Results from a three‐dimensional model and implications for the North Atlantic nitrogen budget, Global Biogeochemical Cycles, 20, 2006.

Festa, J. F., and Hansen, D. V.: Turbidity maxima in partially mixed estuaries: A two-dimensional numerical model, Estuarine and Coastal Marine Science, 7, 347-359, 1978.

Fischer, H. B.: Mass transport mechanisms in partially stratified estuaries, Journal of fluid mechanics, 53, 671-687, 1972.

Fisher, T. R., Harding, L. W., Stanley, D. W., and Ward, L. G.: Phytoplankton, nutrients, and turbidity in the Chesapeake, Delaware, and Hudson estuaries, Estuarine, Coastal and Shelf Science, 27, 61-93, 1988.

Friedrichs, C., Armbrust, B., and De Swart, H.: Hydrodynamics and equilibrium sediment dynamics of shallow, funnel-shaped tidal estuaries, Physics of estuaries and coastal seas, 315-327, 1998.

Fugate, D. C., and Friedrichs, C. T.: Determining concentration and fall velocity of estuarine particle populations using ADV, OBS and LISST, Continental Shelf Research, 22, 1867-1886, 2002.

Fugate, D. C., and Friedrichs, C. T.: Controls on suspended aggregate size in partially mixed estuaries, Estuarine, Coastal and Shelf Science, 58, 389-404, 2003.

Fugate, D. C., Friedrichs, C. T., and Sanford, L. P.: Lateral dynamics and associated transport of sediment in the upper reaches of a partially mixed estuary, Chesapeake Bay, USA, Continental shelf research, 27, 679-698, 2007.

Gallegos, C. L., Jordan, T. E., Hines, A. H., and Weller, D. E.: Temporal variability of optical properties in a shallow, eutrophic estuary: Seasonal and interannual variability, Estuarine, Coastal and Shelf Science, 64, 156-170, 2005.

Ganju, N., Miselis, J., and Aretxabaleta, A.: Physical and biogeochemical controls on light attenuation in a eutrophic, back-barrier estuary, Biogeosciences, 11, 7193-7205, 2014.

Ganju, N. K., and Schoellhamer, D. H.: Annual sediment flux estimates in a tidal strait using surrogate measurements, Estuarine, Coastal and Shelf Science, 69, 165-178, 2006.

Garvine, R. W., McCarthy, R. K., and Wong, K.-C.: The axial salinity distribution in the Delaware estuary and its weak response to river discharge, Estuarine, Coastal and Shelf Science, 35, 157-165, 1992.

Gerbi, G. P., Trowbridge, J. H., Edson, J. B., Plueddemann, A. J., Terray, E. A., and Fredericks, J. J.: Measurements of Momentum and Heat Transfer across the Air–Sea Interface, Journal of Physical Oceanography, 38, 2008.

Geyer, W. R.: Three‐dimensional tidal flow around headlands, Journal of Geophysical Research: Oceans, 98, 955-966, 1993a.

Geyer, W. R.: The importance of suppression of turbulence by stratification on the estuarine turbidity maximum, Estuaries, 16, 113-125, 1993b.

Geyer, W. R., Trowbridge, J. H., and Bowen, M. M.: The Dynamics of a Partially Mixed Estuary*, Journal of Physical Oceanography, 30, 2035-2048, 2000.

Geyer, W. R., Woodruff, J. D., and Traykovski, P.: Sediment transport and trapping in the Hudson River estuary, Estuaries, 24, 670-679, 2001.

Geyer, W. R., Scully, M. E., and Ralston, D. K.: Quantifying vertical mixing in estuaries, Environmental fluid mechanics, 8, 495-509, 2008.

Gibbs, R. J., Konwar, L., and Terchunian, A.: Size of flocs suspended in Delaware Bay, Canadian Journal of Fisheries and Aquatic Sciences, 40, s102-s104, 1983.

Haidvogel, D. B., Arango, H. G., Hedstrom, K., Beckmann, A., Malanotte-Rizzoli, P., and Shchepetkin, A. F.: Model evaluation experiments in the North Atlantic Basin: simulations in nonlinear terrain-following coordinates, Dynamics of Atmospheres and Oceans, 32, 239-281, 2000.

Haidvogel, D. B., Arango, H., Budgell, W. P., Cornuelle, B. D., Curchitser, E., Di Lorenzo, E., Fennel, K., Geyer, W. R., Hermann, A. J., and Lanerolle, L.: Ocean forecasting in terrain-following coordinates: Formulation and skill assessment of the Regional Ocean Modeling System, Journal of Computational Physics, 227, 3595-3624, 2008.

Hansen, D. V., and Rattray, M.: Gravitational circulation in straits and estuaries, Journal of Marine Research, 23, 1965.

Hermes, A. L.: Spatial and seasonal particulate organic carbon cycling within the Delaware estuary, assessed using biomarker and stable carbon isotopic approaches, Rutgers University-Graduate School-New Brunswick, 2013.

Hermes, A. L., and Sikes, E. L.: Particulate organic matter higher concentrations, terrestrial sources and losses in bottom waters of the turbidity maximum, Delaware Estuary, USA, Estuarine, Coastal and Shelf Science, 180, 179-189, 2016.

Hill, P. S., Milligan, T. G., and Geyer, W. R.: Controls on effective settling velocity of suspended sediment in the Eel River flood plume, Continental Shelf Research, 20, 2095-2111, 2000.

Huguenard, K., Valle‐Levinson, A., Li, M., Chant, R., and Souza, A.: Linkage between lateral circulation and near‐surface vertical mixing in a coastal plain estuary, Journal of Geophysical Research: Oceans, 2015.

Huijts, K., Schuttelaars, H., De Swart, H., and Valle‐Levinson, A.: Lateral entrapment of sediment in tidal estuaries: An idealized model study, Journal of Geophysical Research: Oceans (1978‐2012), 111, 2006.

Huijts, K. M., de Swart, H. E., Schramkowski, G. P., and Schuttelaars, H. M.: Transverse structure of tidal and residual flow and sediment concentration in estuaries, Ocean dynamics, 61, 1067-1091, 2011.

Huzzey, L. M., and Brubaker, J. M.: The formation of longitudinal fronts in a coastal plain estuary, Journal of Geophysical Research: Oceans (1978–2012), 93, 1329-1334, 1988.

Janzen, C. D., and Wong, K. C.: Wind‐forced dynamics at the estuary‐shelf interface of a large coastal plain estuary, Journal of Geophysical Research: Oceans (1978‐2012), 107, 2-1-2-12, 2002.

Jay, D., and Musiak, J.: Internal tidal asymmetry in channel flows: Origins and consequences, Coastal and Estuarine Studies, 50, 211-249, 1996.

Jay, D. A., and Musiak, J. D.: Particle trapping in estuarine tidal flows, Journal of Geophysical Research: Oceans (1978–2012), 99, 20445-20461, 1994.

Johnson, G. A.: The purification of public water supplies, US Government Printing Office, 1913.

Ketchum, B. H.: The distribution of salinity in the estuary of the Delaware River, Woods Hole Oceanographic Institution, 1952.

Kildow, J. T., Colgan, C. S., Johnston, P., Scorse, J. D., and Gardiner Farum, M.: State of the US Ocean and Coastal Economies 2016, 2016.

Kineke, G., and Sternberg, R.: Measurements of high concentration suspended sediments using the optical backscatterance sensor, Marine Geology, 108, 253-258, 1992.

Kirincich, A. R., Lentz, S. J., and Gerbi, G. P.: Calculating Reynolds Stresses from ADCP Measurements in the Presence of Surface Gravity Waves Using the Cospectra-Fit Method, Journal of Atmospheric & Oceanic Technology, 27, 2010.

Kocum, E., Underwood, G. J., and Nedwell, D. B.: Simultaneous measurement of phytoplanktonic primary production, nutrient and light availability along a turbid, eutrophic UK east coast estuary (the Colne Estuary), Marine ecology progress series, 231, 1-12, 2002.

Lawson, S., Wiberg, P., McGlathery, K., and Fugate, D.: Wind-driven sediment suspension controls light availability in a shallow coastal lagoon, Estuaries and Coasts, 30, 102-112, 2007.

Lerczak, J. A., and Geyer, W. R.: Modeling the lateral circulation in straight, stratified estuaries, Journal of Physical Oceanography, 34, 2004.

Lerczak, J. A., Geyer, W. R., and Chant, R. J.: Mechanisms Driving the Time-Dependent Salt Flux in a Partially Stratified Estuary*, Journal of Physical Oceanography, 36, 2296-2311, 2006.

MacCready, P.: Toward a unified theory of tidally-averaged estuarine salinity structure, Estuaries, 27, 561-570, 2004.

MacCready, P.: Estuarine adjustment, Journal of Physical Oceanography, 37, 2133-2145, 2007.

MacCready, P., and Geyer, W. R.: Advances in estuarine physics, Annual Review of Marine Science, 2, 35-58, 2010.

Malone, T., Crocker, L., Pike, S., and Wendler, B.: Influences of river flow on the dynamics of phytoplankton production in a partially stratified estuary, Marine ecology progress series. Oldendorf, 48, 235-249, 1988.

Mansue, L. J., and Commings, A. B.: Sediment transport by streams draining into the Delaware Estuary, US Government Printing Office, 1974.

Marchesiello, P., McWilliams, J. C., and Shchepetkin, A.: Open boundary conditions for long-term integration of regional oceanic models, Ocean modelling, 3, 1-20, 2001.

May, C. L., Koseff, J. R., Lucas, L. V., Cloern, J. E., and Schoellhamer, D. H.: Effects of spatial and temporal variability of turbidity on phytoplankton blooms, Marine Ecology Progress Series, 254, 111-128, 2003.

McSweeney, J. M., Chant, R., and Sommerfield, C. K.: Lateral Variability of Sediment Transport in the Delaware Estuary, Journal of Geophysical Research: Oceans, 121, 725-744, 10.1002/2015JC010974, 2016a.

McSweeney, J. M., Chant, R. J., Wilkin, J. L., and Sommerfield, C. K.: Suspended-sediment impacts on light-limited productivity in the Delaware Estuary, Estuaries and Coasts, submitted, 2016b.

Meade, R. H.: Landward transport of bottom sediments in estuaries of the Atlantic coastal plain, Journal of Sedimentary Research, 39, 222-234, 1969.

Monismith, S. G., Kimmerer, W., Burau, J. R., and Stacey, M. T.: Structure and flow-induced variability of the subtidal salinity field in northern San Francisco Bay, Journal of Physical Oceanography, 32, 3003-3019, 2002.

Nash, D. B.: Effective sediment-transporting discharge from magnitude-frequency analysis, The Journal of Geology, 79-95, 1994.

Neiheisel, J.: Source of detrital heavy minerals in estuaries of the Atlantic Coastal Plain, 1973.

Nunes, R., and Simpson, J.: Axial convergence in a well-mixed estuary, Estuarine, Coastal and Shelf Science, 20, 637-649, 1985.

Orlanski, I.: A simple boundary condition for unbounded hyperbolic flows, Journal of computational physics, 21, 251-269, 1976.

Pape, E. H., and Garvine, R. W.: The subtidal circulation in Delaware Bay and adjacent shelf waters, Journal of Geophysical Research: Oceans (1978–2012), 87, 7955-7970, 1982.

Pennock, J. R.: Chlorophyll distributions in the Delaware estuary: regulation by light-limitation, Estuarine, Coastal and Shelf Science, 21, 711-725, 1985.

Pennock, J. R., and Sharp, J. H.: Phytoplankton production in the Delaware Estuary: temporal and spatial variability, Marine Ecology Progress Series, 34, 143-155, 1986.

Pennock, J. R.: Temporal and spatial variability in phytoplankton ammonium and nitrate uptake in the Delaware Estuary, Estuarine, Coastal and Shelf Science, 24, 841-857, 1987.

Pennock, J. R., and Sharp, J. H.: Temporal alternation between light- and nutrient-limitation of phytoplankton production in a coastal plain estuary, Marine ecology progress series. Oldendorf, 111, 275-288, 1994.

Pijanowski, K.: Patterns and Rates of Historical Shoreline Change in the Delaware Estuary, Master of Science in Marine Studies, University of Delaware, 2016.

Postma, H.: Sediment transport and sedimentation in the estuarine environment, American Association for the Advancement of Science publication, 83, 158-179, 1967.

Pritchard, D.: Estuatine Hydrography, Advances in Geophysics, 1, 243-280, 1952.

Pritchard, D. W.: The dynamic structure of a coastal plain estuary, J. Mar. Res, 15, 33-42, 1956.

PWD: Drinking Water Quality Report, Philadelphia Water Department 2016.

Ralston, D. K., Geyer, W. R., and Lerczak, J. A.: Subtidal salinity and velocity in the Hudson River estuary: Observations and modeling, Journal of Physical Oceanography, 38, 753-770, 2008.

Ralston, D. K., and Geyer, W. R.: Episodic and long-term sediment transport capacity in the Hudson River estuary, Estuaries and coasts, 32, 1130-1151, 2009.

Ralston, D. K., Geyer, W. R., and Warner, J. C.: Bathymetric controls on sediment transport in the Hudson River estuary: Lateral asymmetry and frontal trapping, Journal of Geophysical Research: Oceans (1978–2012), 117, 2012.

Ralston, D. K., Warner, J. C., Geyer, W. R., and Wall, G. R.: Sediment transport due to extreme events: The Hudson River estuary after tropical storms Irene and Lee, Geophysical Research Letters, 40, 5451-5455, 2013.

Rozovskiĭ, I. L.: Flow of water in bends of open channels, Academy of Sciences of the Ukrainian SSR, 1957.

Sanford, L. P., and Maa, J. P.-Y.: A unified erosion formulation for fine sediments, Marine Geology, 179, 9-23, 2001.

Schubel, J. R.: Turbidity maximum of the northern Chesapeake Bay, Science, 161, 1013-1015, 1968.

Scully, M. E., and Friedrichs, C. T.: The influence of asymmetries in overlying stratification on near-bed turbulence and sediment suspension in a partially mixed estuary, Ocean Dynamics, 53, 208-219, 2003.

Scully, M. E., and Friedrichs, C. T.: Sediment pumping by tidal asymmetry in a partially mixed estuary, Journal of Geophysical Research: Oceans (1978–2012), 112, 2007a.

Scully, M. E., and Friedrichs, C. T.: The Importance of Tidal and Lateral Asymmetries in Stratification to Residual Circulation in Partially Mixed Estuaries*, Journal of Physical Oceanography, 37, 1496-1511, 2007b.

Scully, M. E., and Geyer, W. R.: The Role of Advection, Straining, and Mixing on the Tidal Variability of Estuarine Stratification, Journal of Physical Oceanography, 42, 2012.

Sharp, J. H., Culberson, C. H., and Church, T. M.: The chemistry of the Delaware estuary. General considerations, Limnology and Oceanography, 27, 1015-1028, 1982.

Sharp, J. H., Pennock, J. R., Church, T. M., Tramontano, J. M., and Cifuentes, L. A.: The estuarine interaction of nutrients, organics, and metals: A case study in the Delaware Estuary, in: The Estuary as a Filter, Academic Press, New York, 241-258, 1984.

Sharp, J. H., Cifuentes, L. A., Coffin, R. B., Pennock, J. R., and Wong, K.-C.: The influence of river variability on the circulation, chemistry, and microbiology of the Delaware Estuary, Estuaries, 9, 261-269, 1986.

Sharp, J. H., Yoshiyama, K., Parker, A. E., Schwartz, M. C., Curless, S. E., Beauregard, A. Y., Ossolinski, J. E., and Davis, A. R.: A biogeochemical view of estuarine eutrophication: Seasonal and spatial trends and correlations in the Delaware Estuary, Estuaries and coasts, 32, 1023-1043, 2009.

Shchepetkin, A. F., and McWilliams, J. C.: The regional oceanic modeling system (ROMS): a split-explicit, free-surface, topography-following-coordinate oceanic model, Ocean Modelling, 9, 347-404, 2005.

Simpson, J. H., Brown, J., Matthews, J., and Allen, G.: Tidal straining, density currents, and stirring in the control of estuarine stratification, Estuaries, 13, 125-132, 1990.

Smith, R.: Buoyancy effects upon longitudinal dispersion in wide well-mixed estuaries, Philosophical Transactions of the Royal Society of London. Series A, Mathematical and Physical Sciences, 296, 467-496, 1980.

Sommerfield, C. K., and Madsen, J. A.: Sedimentological and Geophysical Survey of the Upper Delaware Estuary: Final Report to the Delaware River Basin Commission, University of Delaware Sea Grant Publication, 126 pp., 2004.

Sommerfield, C. K., and Wong, K. C.: Mechanisms of sediment flux and turbidity maintenance in the Delaware Estuary, Journal of Geophysical Research: Oceans (1978–2012), 116, 2011.

Stross, R. G., and Sokol, R. C.: Runoff and flocculation modify underwater light environment of the Hudson River estuary, Estuarine, Coastal and Shelf Science, 29, 305-316, 1989.

Taylor, K. E.: Summarizing multiple aspects of model performance in a single diagram, Journal of Geophysical Research: Atmospheres, 106, 7183-7192, 2001.

Umlauf, L., and Burchard, H.: A generic length-scale equation for geophysical turbulence models, Journal of Marine Research, 61, 235-265, 2003.

Uncles, R.: Estuarine physical processes research: some recent studies and progress, Estuarine, Coastal and Shelf Science, 55, 829-856, 2002.

Valle-Levinson, A., Reyes, C., and Sanay, R.: Effects of Bathymetry, Friction, and Rotation on Estuary–Ocean Exchange, Journal of Physical Oceanography, 33, 2003.

Valle‐Levinson, A., Li, C., Wong, K. C., and Lwiza, K. M.: Convergence of lateral flow along a coastal plain estuary, Journal of Geophysical Research: Oceans (1978–2012), 105, 17045-17061, 2000.

Wai, O., Wang, C., Li, Y., and Li, X.: The formation mechanisms of turbidity maximum in the Pearl River estuary, China, Marine Pollution Bulletin, 48, 441-448, 2004.

Wang, Z., Haidvogel, D. B., Bushek, D., Ford, S. E., Hofmann, E. E., Powell, E. N., and Wilkin, J.: Circulation and water properties and their relationship to the oyster disease MSX in Delaware Bay, Journal of Marine Research, 70, 279–308, 2012.

Warner, J. C., Sherwood, C. R., Signell, R. P., Harris, C. K., and Arango, H. G.: Development of a three-dimensional, regional, coupled wave, current, and sediment-transport model, Computers & Geosciences, 34, 1284-1306, 2008.

Weil, C. B.: Sediments, structural framework, and evolution of Delaware Bay, a transgressive estuarine delta, Sea Grant Technical Report, 1977.

Wellershaus, S.: Turbidity maximum and mud shoaling in the Weser estuary, Archiv fur Hydrobiologie, 92, 161-198, 1981.

Wofsy, S.: A simple model to predict extinction coefficients and phytoplankton biomass in eutrophic waters, Limnology and Oceanography, 28, 1144-1155, 1983.

Wong, K.-C., and Sommerfield, C. K.: The variability of currents and sea level in the upper Delaware estuary, Journal of Marine Research, 67, 479-501, 2009.

Wong, K. C., and Garvine, R. W.: Observations of wind‐induced, subtidal variability in the Delaware estuary, Journal of Geophysical Research: Oceans (1978–2012), 89, 10589-10597, 1984.

Wong, K. C.: On the nature of transverse variability in a coastal plain estuary, Journal of Geophysical Research: Oceans (1978–2012), 99, 14209-14222, 1994.

Wong, K. C., and Moses‐Hall, J. E.: On the relative importance of the remote and local wind effects to the subtidal variability in a coastal plain estuary, Journal of Geophysical Research: Oceans (1978–2012), 103, 18393-18404, 1998.

Woodruff, J. D., Geyer, W. R., Sommerfield, C. K., and Driscoll, N. W.: Seasonal variation of sediment deposition in the Hudson River estuary, Marine Geology, 179, 105-119, 2001.

Xia, X., Li, Y., Yang, H., Wu, C., Sing, T., and Pong, H.: Observations on the size and settling velocity distributions of suspended sediment in the Pearl River Estuary, China, Continental Shelf Research, 24, 1809-1826, 2004.

Yoshiyama, K., and Sharp, J. H.: Phytoplankton response to nutrient enrichment in an urbanized estuary: Apparent inhibition of primary production by overeutrophication, Limnology and Oceanography, 51, 424-434, 2006.